



LAWRENCE  
LIVERMORE  
NATIONAL  
LABORATORY

# Oxygen Isotopic Variations in the Outer Margins and Wark-Lovering Rims of Refractory Inclusions

J. I. Simon, J. Matzel, S. B. Simon, I. D. Hutcheon, D. K. Ross, P. K. Weber, L. Grossman

June 29, 2016

Geochimica Cosmochimica Acta

## **Disclaimer**

---

This document was prepared as an account of work sponsored by an agency of the United States government. Neither the United States government nor Lawrence Livermore National Security, LLC, nor any of their employees makes any warranty, expressed or implied, or assumes any legal liability or responsibility for the accuracy, completeness, or usefulness of any information, apparatus, product, or process disclosed, or represents that its use would not infringe privately owned rights. Reference herein to any specific commercial product, process, or service by trade name, trademark, manufacturer, or otherwise does not necessarily constitute or imply its endorsement, recommendation, or favoring by the United States government or Lawrence Livermore National Security, LLC. The views and opinions of authors expressed herein do not necessarily state or reflect those of the United States government or Lawrence Livermore National Security, LLC, and shall not be used for advertising or product endorsement purposes.

1  
2  
3  
4  
5  
6  
7  
8  
9  
10  
11  
12  
13  
14  
15  
16  
17  
18  
19  
20  
21  
22  
23  
24  
25  
26  
27  
28  
29  
30  
31  
32  
33  
34  
35  
36  
37  
38  
39  
40  
41  
42  
43  
44  
45

**Oxygen isotopic variations in the outer margins and Wark-Lovering rims of refractory inclusions**

Justin I. Simon<sup>1\*</sup>, Jennifer E. P. Matzel<sup>2</sup>, Steven B. Simon<sup>3</sup>, Ian D. Hutcheon<sup>2</sup>, D. Kent Ross<sup>1,4</sup>, Peter K. Weber<sup>2</sup>, and Lawrence Grossman<sup>3,5</sup>

<sup>1</sup>Center for Isotope Cosmochemistry and Geochronology,  
Astromaterials Research and Exploration Science Division  
Exploration, Integration, and Science Directorate  
NASA Johnson Space Center  
Houston, TX 77058

<sup>2</sup>Lawrence Livermore National Laboratory  
Livermore, CA 94451

<sup>3</sup>Department of the Geophysical Sciences  
5734 S. Ellis Ave,  
The University of Chicago  
Chicago, IL 60637

<sup>4</sup>University of Texas at El Paso / Jacobs Technology  
Houston, TX 77058

<sup>5</sup>Enrico Fermi Institute  
The University of Chicago  
Chicago, IL 60637

Revised for *Geochimica et Cosmochimica Acta*  
February, 2016

\*Correspondence author: justin.i.simon@nasa.gov

## ABSTRACT

Oxygen isotopic variations across the outer margins and Wark-Lovering (WL) rims of a diverse suite of six coarse-grained Types A and B refractory inclusions from both oxidized and reduced CV3 chondrites suggest that CAIs originated from a  $^{16}\text{O}$ -rich protosolar gas reservoir and were later exposed to both relatively  $^{17,18}\text{O}$ -rich and  $^{16}\text{O}$ -rich reservoirs. The O-isotope profiles of CAIs can be explained by changes in the composition of gas near the protoSun or the migration of CAIs through a heterogeneous nebula. Variability within the inclusion interiors appears to have been set prior to WL rim growth. Modeling the isotopic zoning profiles as diffusion gradients between inclusion interiors and edges establishes a range of permissible time-temperature combinations for their exposure in the nebula. At mean temperatures of 1400 K, models that match the isotope gradients in the inclusions yield timescales ranging from  $5 \times 10^3$  to  $3 \times 10^5$  years. Assuming CAIs originated with a relatively  $^{16}\text{O}$ -rich (protosolar) isotopic composition, differences among the melilite interiors and the isotopic gradients in their margins imply the existence of a number of isotopically distinct reservoirs. Evidence at the edges of some CAIs for subsequent isotopic exchange may relate to the beginning of rim formation. In the WL rim layers surrounding the interiors, spinel is relatively  $^{16}\text{O}$ -rich but subtly distinct among different CAIs. Melilite is often relatively  $^{16}\text{O}$ -poor, but rare relatively  $^{16}\text{O}$ -rich grains also exist. Pyroxene generally exhibits intermediate O-isotope compositions and isotopic zoning. Olivine in both WL and accretionary rims, when present, is isotopically heterogeneous. The extreme isotopic heterogeneity among and within individual WL rim layers and in particular, the observed trends of outward  $^{16}\text{O}$ -enrichments, suggest that rims surrounding CAIs contained in CV3 chondrites, like the inclusions themselves, formed from a number of isotopically distinct gas reservoirs. Collectively, these results support numerical protoplanetary disk models in which CAIs were transported between several distinct nebular reservoirs multiple times prior to accretion onto a parent body.

## INTRODUCTION

Calcium-aluminum-rich inclusions (CAIs) have refractory mineral assemblages consisting of phases predicted to condense from a hot nebula of solar composition (e.g., Grossman, 1972). We now understand that the mineralogy of coarse-grained CAIs is the result of crystallization from melts and that their reset Al-Mg chronologies (MacPherson, *et al.*, 2012) and decoupled stable isotope compositions of refractory and more volatile elements (J. Simon and

80 DePaolo, 2010) likely reflect substantial processing of primordial condensates. Despite evidence  
81 for a complicated history, their old ages (Amelin *et al.*, 2002; Bouvier and Wadhwa, 2010;  
82 Connelly *et al.*, 2012) attest to the fact that they represent some of the most primitive solar  
83 system materials and likely provide our best window into the earliest conditions of the solar  
84 protoplanetary disk. After crystallization of their interiors, most inclusions were rimmed by a  
85 common mineral layering sequence, implying a fundamental change in their environment.  
86 Previous investigations have interpreted these so-called Wark-Lovering (WL) rims (Wark and  
87 Lovering, 1977) as products of formation from nebular reservoirs with pressures (J. Simon *et al.*,  
88 2005), temperatures (Young *et al.*, 2005), and isotopic compositions (Aleon *et al.*, 2007; Krot *et*  
89 *al.*, 2002; J. Simon *et al.*, 2011; Yoshitake *et al.*, 2005; Yurimoto *et al.*, 1998) distinct from those  
90 indicated by the interiors. These environmental changes likely not only produced the  
91 mineralogical variability of WL rims (Dyl *et al.*, 2011; J. Simon *et al.*, 2005), but could also have  
92 led to mineralogical (Keller and Buseck, 1991; Metzler *et al.*, 1992) and isotopic (Fagan *et al.*,  
93 2004a; J. Simon *et al.*, 2011; J. Simon and Young, 2011) changes within the refractory inclusions  
94 themselves.

95         Compared to the terrestrial planets, many CAIs exhibit an  $^{16}\text{O}$ -rich composition ( $\delta^{18}\text{O}$   
96  $\approx \delta^{17}\text{O} \leq -40\text{‰}$ ) that likely reflects the O-isotopic composition of protosolar gas in the nebula  
97 (McKeegan *et al.*, 2011). Yet, it has been known for decades that individual CAIs have  
98 heterogeneous O-isotopic compositions, in some cases spanning the range between protosolar to  
99 planetary reservoirs (Clayton *et al.*, 1977). One can postulate that CAIs condensed, melted,  
100 crystallized, and were rimmed in the relatively  $^{16}\text{O}$ -rich protosolar reservoir, and that any internal  
101 O-isotopic heterogeneity resulted from mineralogically controlled isotope exchange with a  
102 planetary reservoir ( $\delta^{18}\text{O} \sim 0\text{‰}$ ) on the chondrite parent body, e.g., Wasson *et al.* (2001).  
103 Alternatively, the O-isotopic heterogeneity in CAIs can be explained by formation from both  
104 relatively  $^{16}\text{O}$ -rich and  $^{16}\text{O}$ -poor reservoirs of nebular gas (Clayton *et al.*, 1977; Yurimoto *et al.*,  
105 1998; Krot *et al.*, 2002; Yoshitake *et al.*, 2005; Aleon *et al.*, 2007; J. Simon *et al.*, 2011). This  
106 might occur if igneous CAIs formed through admixing melanges of isotopically heterogeneous  
107 material and/or through transport, exposure, and exchange with distinct nebular reservoirs. As of  
108 yet the locations and identities of the reservoirs, the formation processes involved in recording  
109 the isotopic shifts, and the timing of isotopic exchange are not well-constrained.

110         In a prior study (J. Simon *et al.*, 2011), secondary ion mass spectrometry (SIMS)  
111 measurements of the WL rim and outer margin of the Allende compact Type A CAI A37  
112 revealed large O-isotope heterogeneity across the outermost  $\sim 70\ \mu\text{m}$  of the inclusion and showed  
113  $>25\text{‰}$  variations in  $\Delta^{17}\text{O}$  (departure from the terrestrial mass fractionation line;  $\Delta^{17}\text{O} = \delta^{17}\text{O} -$

114  $0.52 \times \delta^{18}\text{O}$ ) within the  $\sim 100$   $\mu\text{m}$ -thick WL rim. Those workers proposed that the variations  
115 reflected either transport of the inclusion between distinct nebular reservoirs inherited from the  
116 parental molecular cloud, or a time-varying oxygen isotopic composition of a region of the  
117 nebula, such as the relatively  $^{16}\text{O}$ -poor gas predicted for the outer margins of the disk by  
118 photochemical self-shielding models (Lyons and Young, 2005). Although some rims  
119 surrounding CAIs exhibit extreme O-isotopic heterogeneity, others are isotopically homogeneous  
120 (Matzel *et al.*, 2013; Bodénan *et al.*, 2014). More studies that report O-isotopic records with high  
121 spatial resolution are needed to constrain solar protoplanetary disk evolution models, such as  
122 those of Cuzzi *et al.* (2003), Boss (2004), and Ciesla (2007). It is noteworthy that some rims  
123 consist of only a single pyroxene layer (e.g., Bodénan *et al.* 2014), while others are far more  
124 complex, such as the WL rim surrounding Leoville CAI L6 (this study) that consists of at least 9  
125 distinct mineral layers. Comparison of O-isotopic compositions of petrographically distinct rim  
126 sequences will improve our understanding of their astrophysical significance.

127         The nature of chondritic host rocks and the potentially disparate formation histories of  
128 their constituent components create challenges to interpretation of the O-isotopic records of  
129 individual CAIs. In particular, parent body alteration may produce O-isotope heterogeneity. To  
130 document O-isotopic heterogeneity to test models for the evolution of the protoplanetary disk,  
131 this work presents the results of coordinated high-spatial resolution oxygen and petrologic  
132 investigations of CAIs with a range of mineralogical compositions and alteration histories from  
133 the Allende, Efremovka, and Leoville CV3 chondrites.

134

135

## METHODS

136

### Oxygen Isotopic Zoning Profiles by NanoSIMS

138         Oxygen isotope measurements were performed using the NanoSIMS 50 at Lawrence  
139 Livermore National Laboratory (LLNL), following the method developed by J. Simon *et al.*  
140 (2011), during  $\sim 5$  weeks of analysis over an  $\sim 3$ -year period (Table 1, Appendix D).  
141 Measurements were performed by sputtering the polished surfaces of CAIs in carbon-coated thin  
142 sections and epoxy embedded thick sections with a 16 keV,  $\sim 12$  pA  $\text{Cs}^+$  beam focused to a  $\sim 100$   
143 nm spot size and rastered over  $2 \times 2$   $\mu\text{m}$  regions. Negative secondary ions of  $^{16}\text{O}$ ,  $^{17}\text{O}$ ,  $^{18}\text{O}$ , and  
144  $^{28}\text{Si}$  (or  $^{30}\text{Si}$ ) were collected in a Faraday cup and three separate electron multipliers,  
145 respectively. Each measurement comprises  $(3-6) \times 10^5$  counts of  $^{17}\text{O}$  and  $(1.5-3.0) \times 10^6$  counts of  
146  $^{18}\text{O}$  collected during a 368-second analysis time. The data were corrected for detector dead time.  
147 Measured uncertainties reflect the standard deviation of isotope ratio data acquired over 300  
148 rastered measurement cycles and follow a Poisson distribution. Uncertainties reported in Table 1

149 reflect a combination of counting statistics and either 2 standard errors ( $\pm e_m$ ) or 2 standard  
150 deviations (sd) of the average value of the measured mineral standards used for sample-standard  
151 bracketing (Appendices I and II). A mass resolving power of  $\sim 7000$  was used to resolve  $^{17}\text{O}$   
152 from  $^{16}\text{OH}^-$ . Monitoring the  $\text{Si}^-/^{16}\text{O}^-$  ratio (in addition to pre- and post-analysis using  
153 backscattered electron and X-ray images) allowed identification of the phases analyzed, which is  
154 critical for interpretation of analyses within the fine mineral layers of WL rims and near crystal  
155 boundaries in interiors of CAIs. A normal-incidence electron gun was utilized for charge  
156 compensation.

157 Oxygen isotopic zoning profiles were obtained by conducting NanoSIMS traverses across  
158 the rims and outer margins of CAIs. In most cases more than one traverse across a comparable  
159 region of a given CAI was measured. Within select traverses, analyses were made out of spatial  
160 sequence in order to separate potential analytical shifts from gradients in the samples themselves.  
161 Measurements were made on six CAIs and include analyses of primary melilite, spinel, fassaite  
162 and anorthite; secondary grossular, plagioclase, and sodalite in the CAI interiors; and olivine, Ti-  
163 pyroxene, aluminous pyroxene, spinel, anorthite, hibonite, perovskite and secondary nepheline  
164 and andradite in the WL rims. Each individual datum reflects a  $\sim 2 \times 2 \mu\text{m}$  spot analysis from a  
165 single mineral phase, as evaluated by the observed  $^{28 \text{ (or } 30)}\text{Si}^-/^{16}\text{O}^-$  ion ratios and by SEM analyses  
166 after the NanoSIMS measurements, unless stated otherwise. Oxygen isotopic compositions are  
167 reported in terms of  $\delta^{17}\text{O}$  and  $\delta^{18}\text{O}$ , the permil differences from the reference ratios of standard  
168 mean ocean water (SMOW);  $\delta^i\text{O} = 10^3 \times ((^i\text{O}/^{16}\text{O})/(^i\text{O}/^{16}\text{O})_{\text{SMOW}} - 1)$ , where  $i$  is either 17 or 18.  
169  $\Delta^{17}\text{O}$ , defined as  $\Delta^{17}\text{O} = \delta^{17}\text{O} - 0.521 \times \delta^{18}\text{O}$ , represents the departure of the sample composition  
170 from the terrestrial mass fractionation (TMF) line that defines the terrestrial oxygen reservoir.

171 Instrumental mass fractionation (IMF) and experimental reproducibility were determined  
172 through replicate analyses of terrestrial spinel, anorthite, grossular, pyroxene, and forsterite  
173 standards. The standard analyses were interspersed with unknowns. Periodically an automated  
174 series of standard analyses ( $n \approx 10\text{-}15$ ) were run overnight. The individual measurements that  
175 made up these standard series scattered about their average value, but did not exhibit significant  
176 systematic shifts attesting to the fact that on a day-to-day timeframe instrument IMF conditions  
177 were stable. Over the  $\sim 3$ -year period of the study, however, IMF conditions did vary and data  
178 were corrected accordingly. The IMF corrections were handled in two different ways. In the first,  
179 mineral-specific corrections were applied to the unknown measurements based on the standards  
180 used for each session. In the second an average of the mineral-specific corrections was applied,  
181 based on the standards used for each session. The overall difference between the two approaches  
182 was negligible and only varied up to  $\sim 1.5\text{‰}$  (see columns #8 and #10, respectively in Table 1

183 and details in Appendix II). Systematic mass independent effects varied among the different  
184 mineral standards in each analytical session, but by no more than ~2‰. The reproducibility in  
185  $\Delta^{17}\text{O}$  among 521 terrestrial mineral standard analyses was  $\leq 6\text{‰}$  (2 sd), after IMF corrections  
186 were applied, and within a given session ~4‰ (2 sd) as summarized in Appendix II. For internal  
187 consistency only the spinel, anorthite, and olivine standards were used in the reported error of the  
188 unknowns as these were measured in every session. The uncertainty of individual measurements  
189 was  $\leq 4\text{‰}$  (2 sd) for  $\delta^{17}\text{O}$  and  $\leq 2\text{‰}$  (2 sd) for  $\delta^{18}\text{O}$ . In ideal cases (e.g., comparing the averages  
190 of multiple analyses of distinct regions along a single traverse within a given session), a  
191 difference in  $\Delta^{17}\text{O}$  as small as ~1-2‰ (2 se<sub>m</sub>) appears resolvable, whereas a more conservative  
192 evaluation of uncertainty consistent with the inter-session reproducibility of standards is closer to  
193  $\pm 4\text{‰}$  (2 sd).

194

#### 195 *Avoiding oxygen isotopic measurements of mineral mixtures*

196 Analysis of more than one, isotopically-distinct, mineral phase in a single rastered spot  
197 may lead to spurious O-isotope values. This problem is particularly acute for the analysis of  
198 mineral layers within WL-rims, where the thin individual mineral layers can be difficult to  
199 resolve. We evaluated each O-isotope analysis for the possibility that it might reflect a mixture of  
200 two or more minerals by both comparing pre-analysis and post-analysis SEM images and  
201 evaluating the corresponding  $^{28}$  or  $^{30}\text{Si}^{-16}\text{O}^{-}$  ion ratios. This combined approach effectively  
202 identifies analytical volumes that sampled more than one mineral, as SEM images alone do not  
203 always reveal accessory phases or minor contributions. In general, the  $^{28}$  or  $^{30}\text{Si}^{-16}\text{O}^{-}$  ion ratios of  
204 individual minerals are diagnostic, especially between oxides and silicates in the present samples  
205 (Fig. 1). The  $^{28}$  or  $^{30}\text{Si}^{-16}\text{O}^{-}$  ratio of diopside is clearly distinguishable from that of melilite. It is  
206 not always possible, however, to use the ion ratio approach to distinguish Ti-pyroxene from a  
207 mixture of Ti-pyroxene and melilite, so the post-analysis SEM images were heavily relied upon.  
208 Among the samples analyzed here, only the WL rim on the Leoville sample (L6) has pyroxene in  
209 contact with melilite. Measurements of  $^{28}$  or  $^{30}\text{Si}^{-16}\text{O}^{-}$  ratios were not calibrated, and only intra-  
210 amount and intra-analytical session comparisons were made.

211

#### 212 **X-ray Mapping and Mineral Compositions by Scanning Electron Microscope and** 213 **Microprobe**

214 Mineral compositions, X-ray maps and backscattered electron images (BEI) were  
215 obtained at NASA Johnson Space Center (JSC), The University of Chicago, and LLNL to study  
216 the petrography of the inclusions, guide NanoSIMS traverses, and verify the mineralogy of  
217 analysis spots. High-resolution BEI and digital X-ray maps were obtained with a JEOL JSM-

218 7600F SEM at JSC and with an FEI Inspect F field emission SEM at LLNL. At JSC, X-ray maps  
219 were obtained with a ThermoElectron SDD X-ray detector and ThermoElectron software using a  
220 15 kV beam and 30 nA beam current. At LLNL, element maps were made with an EDAX  
221 Apollo 40 energy-dispersive X-ray microanalysis system. At The University of Chicago, selected  
222 areas of the samples were documented with a JEOL JSM-5800LV SEM operated at 15 kV and 1  
223 nA beam current.

224 Electron microprobe traverses were conducted across the margins of select inclusions to  
225 document chemical zoning profiles in melilite. Wavelength-dispersive (WDS) analyses were  
226 obtained with a Cameca SX-50 electron microprobe operated at 15 kV at The University of  
227 Chicago. The WDS data were reduced using the modified ZAF correction procedure PAP  
228 (Pouchou and Pichoir, 1984). For Efremovka sample Ef-1, melilite compositions were obtained  
229 using the SX-100 electron microprobe at JSC. The JSC electron probe was operated at 15 kV  
230 with a 20 nA beam current, and also used PAP data reduction.

231

## 232 **Modeling Oxygen Isotopic Exchange in CAIs**

233 Assuming that the gradients defined by O-isotopic profiles in the interiors of CAIs were  
234 established by incomplete exchange between a primordial, or other initial, isotopic composition  
235 characteristic of the CAI interior and an external isotopic reservoir, oxygen diffusion models  
236 were used to assess the timescale for establishing the observed profiles. For non-steady state  
237 diffusion in spherical coordinates, equation 6.18 of Crank (1975),

$$238 \quad \frac{C-C_{i,cond}}{C_0-C_{i,cond}} = 1 + \frac{2a}{\pi r} \sum_{n=1}^{\infty} \frac{(-1)^n}{n} \sin \frac{n\pi r}{a} \exp(-D_i n^2 \pi^2 t/a^2), \quad (1)$$

239 was used to determine  $(C-C_{i,cond})/(C_0-C_{i,cond})$  as a function of  $r$ , the distance from the edge of the  
240 inclusion of radius  $a$ ; and  $t$ , time; where  $C_{i,cond}$  is an initially uniform concentration of a particular  
241 oxygen isotope in the condensed phase, assumed to be melilite, either crystalline or its molten  
242 equivalent;  $C_0$  is the surface concentration of the same isotope, assumed to be constant;  $C$  is the  
243 concentration of that isotope at  $r$  and  $t$ ; and  $D_i$  is the temperature-dependent diffusivity of each  
244 isotope in the solid-state from Ryerson and McKeegan (1994) and in Type A and B melts using  
245 the viscosity-based parameterization of Liang *et al.* (1996), respectively. Computed profiles for  
246 each isotope were combined to obtain profiles for  $\Delta^{17}\text{O}$ .  $C_{i,cond}$  was inferred from  $\Delta^{17}\text{O}$  analyses  
247 of either interior spinel or uniform melilite. Various isotopic compositions were used for  $C_0$ :  
248 either  $\Delta^{17}\text{O}$  of the innermost WL rim layer; the Allende matrix composition for testing parent  
249 body exchange scenarios; or an assumed planetary-like oxygen isotopic composition of an  
250 ambient solar nebular gas. For nebular exchange models, the sum of the partial pressures of all  
251 oxygen-containing gas species,  $\sim 10^{-6}$  bar, obtained from solar gas equilibrium condensation

252 calculations at 1400 K and  $P^{\text{tot}} = 10^{-2}$  or  $10^{-3}$  bar (Fedkin and Grossman, 2006), was used to  
253 obtain  $C_0$ . For parent body scenarios, the abundance of oxygen at the inclusion surface reflects  
254 that of an Allende matrix composition (Clark *et al.* 1970). Diffusion times were calculated at  
255 1400 K and 900 K for nebular and parent body exchange, respectively.

256

257

## RESULTS

258

### Petrography of Refractory Inclusions

260

261

262

263

264

265

266

267

268

269

270

271

272

273

274

275

The petrography of the CAIs included in this study has been described in detail elsewhere (Meeker *et al.*, 1983; S. Simon *et al.*, 1999, 2001; S. Simon and Grossman, 2013). The CAIs are igneous with a range of mineral assemblages: The compact Type A CAIs are dominated by blocky, coarse-grained melilite and fassaite enclosing euhedral spinel grains and anhedral perovskite grains; the Type B CAIs have more abundant fassaite than the Type A CAIs, with coarse-grained anorthite and melilite enclosing smaller spinel grains. Like most CAIs, those studied here likely experienced one or more reheating events that led to such processes as melting, solid-state recrystallization, and possibly reactions between primary phases and an external reservoir (e.g., MacPherson and Davis, 1993; Hsu *et al.*, 2000; J. Simon and Young, 2011). Varying abundances of secondary minerals are found in the inclusions, consistent with differences seen previously in CAIs from oxidized and reduced chondrites (Brearley and Jones, 1998, and references therein). The suite of inclusions studied here represents a range in the degree of secondary alteration, from least to most: Ef-1/L6, A37, Egg-6, TS4, and ALH3. Images of the samples are shown in Figures 2-7.

275 *Compact Type A CAIs: Ef-1 (Efremovka), L6 (Leoville), ALH3 (Allende), and A37 (Allende)*

276

277

278

279

280

281

Ef-1 (Efremovka), Fig. 2, is a convoluted compact Type A CAI, ~3x3.5 mm, composed mainly of visually unaltered melilite and 20-70  $\mu\text{m}$ -sized spinel grains, with interstitial, anhedral fassaite. The inclusion is surrounded by a simple ~15 to 40  $\mu\text{m}$  thick WL rim made up, from the interior outwards, of spinel and pyroxene (Fig. 2A, B). Melilite in Ef-1 is largely gehlenitic ( $\text{\AA}k_{10\pm 2}$ ), except at the outermost edge where it is slightly more magnesian ( $\sim\text{\AA}k_{17}$ ), as shown in Fig. 8A. Representative melilite analyses are given in Table 2.

282

283

284

285

L6 (Leoville), Fig. 3, is a visually unaltered compact Type A inclusion, originally ~6-7 mm, with clusters of spinel grains (typically euhedral, ~50  $\mu\text{m}$  across) and fassaite (anhedral) enclosed in melilite. At the edge of L6, a nearly continuous, thick (up to 100  $\mu\text{m}$ ) WL rim layer consists of spinel intergrown with melilite. Outside the main spinel layer, there are additional

286 occurrences of pyroxene ±melilite layers. Based on petrography and mineral chemistry, five  
287 generations of pyroxene (Fig. 3B-D) were identified (S. Simon and Grossman, 2013) outside of  
288 the innermost spinel layer. Representative electron probe analyses of each of these five  
289 generations are given in Table 3. The innermost pyroxene layer (Ti-pyx-1) is Ti-rich and  
290 intergrown with the “main” spinel layer. This pyroxene layer ( $\leq 10 \mu\text{m}$  thick) has a sharp contact  
291 with a zoned pyroxene layer (Ti-pyx-2) that becomes less Ti-rich outward and is in contact with  
292 a layer of varying thickness consisting of melilite and spinel. Two other Ti-rich pyroxene units  
293 (Ti-pyx-3; Ti-pyx-4) with distinct compositions occur (S. Simon and Grossman, 2013). Finally,  
294 the entire inclusion and inner rims are surrounded by a uniform layer of diopside ( $\sim 15 \mu\text{m}$ , Al-  
295 pyx-5, Fig. 3C), that in some places is in direct contact with the Ti-bearing pyroxene of an inner  
296 layer but more commonly overlies the irregular, granular mixed melilite-spinel layer.

297 In L6 melilite is found in several rim layers that range in grain size and, in places, are  
298 locally bifurcated by discontinuous spinel layers (Fig. 3B). The åkermanite content in the  
299 innermost layer (Mel-1) decreases radially outward from  $\sim \text{Åk}_{15}$  to  $\sim \text{Åk}_5$ . The åkermanite content  
300 in the next layer (Mel-2) increases radially outward from  $\sim \text{Åk}_5$  to  $\sim \text{Åk}_{13}$  (see Fig. 8B). In places,  
301 the innermost melilite can be found in contact with the “main” spinel layer rather than the inner  
302 Ti-rich zoned pyroxene layer (Ti-pyx-2). The third occurrence of rim melilite (Mel-3) is found in  
303 “peninsulas” sitting on top of pyroxene layer Ti-pyx-3. It has a range of grain sizes that appear to  
304 correlate with spinel content, with the coarser melilite enclosing fewer spinel grains. Across the  
305 outer  $\sim 200 \mu\text{m}$  of the inclusion, the åkermanite content of the melilite decreases radially  
306 outward, from  $\text{Åk}_{30}$  to  $\text{Åk}_3$ .

307 Based on electron microprobe analyses summarized in Table 3, all of the WL rim  
308 pyroxene layers surrounding L6 exhibit lower  $\text{Ti}^{3+}/\text{Ti}^{\text{tot}}$  than those measured in the interior  
309 fassaite (0.71) similar to that reported elsewhere for other WL rims, e.g., Dyl *et al.* (2011). In  
310 detail,  $\text{Ti}^{3+}/\text{Ti}^{\text{tot}}$  decreases from the innermost layer, Ti-pyx-1 (0.57), to Ti-pyx-2 (0.42, inner  
311 sublayer), to Ti-pyx-2 ( $\sim 0$ , outer sublayer). Then there is a reversal towards slightly higher  
312  $\text{Ti}^{3+}/\text{Ti}^{\text{tot}}$  in Ti-pyx-3 (0.29) and Ti-pyx-4 (0.46). Scarce titanium is measured in the outermost  
313 diopside layer (Table 3). There is a range of  $\text{Ti}^{3+}/\text{Ti}^{\text{tot}}$  in each layer when individual analyses are  
314 considered, showing greater overlap between the layers. These pyroxene layers provide an  
315 opportunity for the first coordinated report of O-isotopes and oxidation state.

316 A37 (Allende), Fig. 4, is a subspherical, compact Type A inclusion,  $\sim 4 \times 7 \text{ mm}$ , composed  
317 primarily of melilite ( $\text{Åk}_{5-36}$ ), 20-70  $\mu\text{m}$ -sized spinel grains and rare fassaite mainly occurring  
318 between the melilite grains (J. Simon *et al.*, 2011 and references therein). The melilite near the  
319 outer margin of the inclusion is zoned in composition from Mg-rich towards the interior to Al-

320 rich towards the edge (Fig. 8C). The surrounding WL rim is ~50 to 100  $\mu\text{m}$  thick and made up of  
321 a typical layered mineral sequence, from the interior outward, of hibonite  $\pm$ melilite, spinel  
322 (enclosing perovskite), melilite/nepheline, Ti-bearing pyroxene, Al-rich pyroxene and an  
323 outermost layer of olivine (Fig. 4B). A small (~50  $\mu\text{m}$  diameter), spinel-rich, perovskite-bearing  
324 “micro-CAI” is located within the WL rim layers (J. Simon *et al.*, 2011). Melilite contained in  
325 the hibonite  $\pm$ melilite rim layer is locally in contact with melilite of the host inclusion (Fig. 4C).

326 ALH3 (Allende), Fig. 5, is a large, subspherical Type A inclusion, ~6 mm, consisting of  
327 melilite, hibonite, and spinel (S. Simon *et al.*, 2001). The range of melilite compositions is  
328 similar to that of other Type A inclusions ( $\text{\AA}k_{1-29}$ ), but there is neither an inclusion-wide trend  
329 nor a dominant core-rim trend within individual crystals (S. Simon *et al.*, 2001). Surrounding the  
330 CAI is an ~30 to 75  $\mu\text{m}$  thick rim containing: (1) secondary anorthitic plagioclase; (2) spinel; (3)  
331 Ti-pyroxene; (4) nepheline (discontinuous layer); (5) Al-diopside; and (6) Fe-rich olivine, ~Fa<sub>50</sub>,  
332 which may be accretionary (Fig. 5B). The inclusion encloses a pocket of matrix, with a second,  
333 ‘interior’ WL rim sequence lining the pocket, varying from ~50 to 100  $\mu\text{m}$  in thickness and  
334 consisting of: (1) secondary anorthitic plagioclase (a discontinuous layer of varying thickness);  
335 (2) spinel (enclosing perovskite); (3) Ti-bearing pyroxene; (4) Al-diopside; and (5) andradite  
336 (Fig. 5C). The primary difference between the sequences is the outermost layer, i.e., Fe-rich  
337 olivine versus andradite.

338

339 *Type B CAIs: Egg-6 (Allende) and TS4 (Allende)*

340 Egg-6 (Allende), Fig. 6, is a subspherical Type B1 inclusion, ~2 cm, with a core of  
341 fassaite, anorthite, spinel, and melilite surrounded by a well-developed melilite ( $\text{\AA}k_{20-60}$ ) mantle  
342 zoned from Mg-rich towards the interior to Al-rich towards the edge. One quarter of the  
343 inclusion is composed of secondary minerals that are typical of those found in alteration veins in  
344 Allende CAIs (MacPherson *et al.*, 1981; Meeker *et al.*, 1983), but this high degree of alteration  
345 was not seen in the section, ~3x6 mm, used for this study. The outer ~20-40  $\mu\text{m}$  of the sample  
346 consists of a simple WL rim of Fe-poor spinel that has a slight increase in FeO grading outward,  
347 which is surrounded by a layer of diopside (Fig. 6B, D-F). The spinel layer encloses a semi-  
348 continuous chain of isolated perovskite and Ti-bearing pyroxene grains (Fig. 6B,C, F).

349 TS4 (Allende), Fig. 7, is an irregularly-shaped Type B2 CAI, ~5x8 mm, composed  
350 mainly of melilite ( $\text{\AA}k_{35-50}$ ), fassaite, anorthite, and 5-70  $\mu\text{m}$ -sized spinel grains found throughout  
351 and in palisades. The interior is rich in fassaite and anorthite that typically poikilitically encloses  
352 high concentrations of spinel grains (Fig. 7A,B). TS4 is surrounded by an ~15 to 60  $\mu\text{m}$  thick  
353 WL rim composed, from the interior outward, of spinel, Ti-bearing pyroxene, Al-rich pyroxene,

354 and an outermost band of olivine (Fig. 7B,C). Outward from the WL rim is a fine-grained olivine  
355 accretionary rim. The margin of the inclusion is locally melilite-rich, with grains that zone from  
356 Mg-rich toward the interior to Al-rich toward the edge of the inclusion (Fig. 8D). Secondary  
357 minerals include patchy nepheline and sodalite at the edge of the CAI and  
358 andradite+wollastonite+hedenbergite in what appears to be a discrete pod or xenolith in the  
359 interior (Ross *et al.*, 2012).

360

## 361 **NanoSIMS Oxygen Isotope Measurements**

362

### 363 *Isotopic zoning profiles across the margins of inclusions*

364 Oxygen isotopic results that have been corrected for mineral-specific IMF effects are  
365 presented in Figures 9 and 10. Both mineral-specific and average IMF corrected data are listed in  
366 Table 1. Also shown in these figures are modeled diffusion profiles, discussed in later sections  
367 and summarized in Table 4. In the following paragraphs, we describe the profiles as either  
368 “normal”, i.e. profiles that exhibit  $^{16}\text{O}$ -enrichments that decrease with distance from the center of  
369 the inclusion, or “reverse”. The A37 and L6 profiles are the most distinctive examples of normal  
370 and reverse profiles, respectively. The two Type B CAIs, Egg-6 and TS4, are most consistent  
371 with normal zoning profiles, whereas Ef-1 and ALH3 are more consistent with reverse zoning  
372 profiles. The contact between melilite at the outer edge of an inclusion (i.e., the margin) and its  
373 WL rim is a feature common to all of the studied inclusions. Therefore, analysis points within the  
374 WL rim and the inclusion interior are plotted as a function of negative and positive distance from  
375 this contact, respectively, in Figures 9 and 10. Unless stated otherwise, the uncertainties for all of  
376 the individual  $\Delta^{17}\text{O}$  values are  $\sim 4\%$  ( $2\text{ se}_m$ ). In order to assess whether specific regions or rim  
377 layers have different oxygen isotopic compositions, the averages of multiple measurements  
378 within these materials are compared. In some instances only a few measurements define the  
379 average value. To account for the statistics of small numbers, 95% confidence intervals are  
380 determined by multiplying the standard errors ( $\text{se}_m$ ) by a Student’s *t*-adjustment (Mahon, 1996).

381 A37: The  $\Delta^{17}\text{O}$  of melilite within the outer 100  $\mu\text{m}$  of A37 increases monotonically  
382 outward from  $-17.5\pm 0.8\%$  ( $n=20$ ), characteristic of the interior, to  $-2.2\pm 3.0\%$  ( $n=6$ ) at the edge  
383 (Fig. 9A). Additional melilite analyses reported here match the composition of the interior  
384 melilite ( $\Delta^{17}\text{O} \sim -18\%$ ) reported by J. Simon *et al.* (2011), and replicate analyses of interior  
385 spinel grains had reproducible, relatively  $^{16}\text{O}$  enriched  $\Delta^{17}\text{O}$  values ranging from  $-28$  to  $-31\%$   
386 ( $n=3$ ).

387 Egg-6: Two traverses across the melilite mantle (Fig. 9B) were complemented by  
388 analyses of fassaite, spinel, and anorthite in the margin and/or within the core of this Type B1  
389 inclusion. Melilite measurements yield an average  $\Delta^{17}\text{O}$  value of  $-2.3\pm 0.9\text{‰}$  ( $n=32$ , squares).  
390 Melilite within  $\sim 300\ \mu\text{m}$  of the edge averages  $-0.9\pm 1.0\text{‰}$  ( $n=13$ , Traverse 1, unrimmed squares)  
391 and  $-2.6\pm 0.8\text{‰}$  ( $n=7$ , Traverse 2, squares with black borders). These values near the edge are  
392 within error of each other but differ slightly from some melilite towards the core. Melilite  
393 beyond  $\sim 300\ \mu\text{m}$  from the inclusion edge exhibits a relatively constant  $\Delta^{17}\text{O}$  of  $-0.1\pm 2.3\text{‰}$  ( $n=4$ )  
394 along Traverse 1, but it is slightly more  $^{16}\text{O}$ -rich as measured by the longer Traverse 2,  
395 exhibiting an average  $\Delta^{17}\text{O}$  value of  $-5.6\pm 0.6\text{‰}$  ( $n=8$ ). Although the individual measurements are  
396 again mostly within error of each other, the apparent difference may reflect small differences in  
397 secondary mineralization along the two traverses, as a result of the fact that Traverse 1 crosscuts  
398 several more veins of secondary minerals than Traverse 2. The average  $\Delta^{17}\text{O}$  value of fassaite  
399 within the melilite mantle is  $-18.2\pm 2.6\text{‰}$  ( $n=4$ , three are  $> 700\ \mu\text{m}$  from the edge, off scale in  
400 Fig. 9B) and that of spinel from the mantle and core is  $-24.7\pm 1.8\text{‰}$  ( $n=9$ ). Primary anorthite  
401 exhibits  $\Delta^{17}\text{O}$  values of  $-5$  and  $-12\text{‰}$  (locations are off scale in Fig. 9B), bracketing the slightly  
402  $^{16}\text{O}$ -enriched melilite compositions measured further towards the interior along Traverse 2. Veins  
403 and patches of secondary plagioclase replacing material between the WL rim and melilite at the  
404 edge of the interior along Traverse 1 have  $\Delta^{17}\text{O}$  values ranging from  $-1.3$  to  $2.4\text{‰}$  ( $n=3$ ), similar  
405 to that of adjacent melilite.

406 TS4: Two traverses across the margin of the Type B2 inclusion TS4 (Fig. 9C) were  
407 accompanied by analyses of fassaite, spinel, and anorthite from further within the interior.  
408 Melilite within  $\sim 500\ \mu\text{m}$  of the edge has an average  $\Delta^{17}\text{O}$  value of  $-0.5\pm 0.7\text{‰}$  ( $n=16$ ), whereas  
409 melilite further inward has  $\Delta^{17}\text{O}$  values that range from  $-4$  to  $-5\text{‰}$  ( $n=3$ ). Fassaite within the  
410 outermost  $\sim 300\ \mu\text{m}$  has an average  $\Delta^{17}\text{O}$  value of  $-22.1\pm 2.1\text{‰}$  ( $n=6$ ), indistinguishable from that  
411 of fassaite further within the interior, with an average  $\Delta^{17}\text{O}$  value of  $-22.3\pm 1.3\text{‰}$  ( $n=6$ ). Spinel  
412 within the interior has an average  $\Delta^{17}\text{O}$  value of  $-22.3\pm 1.5\text{‰}$  ( $n=9$ ), indistinguishable from that  
413 of fassaite (Fig. 9C). Interior anorthite analyses yield  $\Delta^{17}\text{O}$  values that range from  $-11$  to  $-3\text{‰}$   
414 ( $n=4$ ), similar to, or possibly, slightly more  $^{16}\text{O}$ -enriched than melilite compositions also  
415 measured  $>500\ \mu\text{m}$  from the edge.

416 L6: Three NanoSIMS traverses were measured across the melilite margin of this compact  
417 Type A inclusion (Fig. 9D). The most negative  $\Delta^{17}\text{O}$  values ( $-20\text{‰}$ ,  $n=2$ ) occur at the outermost  
418 edge of Traverse 3, and intermediate values (between  $-15$  to  $-10\text{‰}$ ,  $n=5$ ) occur inward along  
419 Traverse 3 and within Traverse 1. The remaining measurements, starting  $\sim 100\ \mu\text{m}$  from the edge

420 to  $\geq 500$   $\mu\text{m}$  inward, including data from Traverses 1 and 2 that represent the bulk of the interior  
421 melilite, show no obvious zoning and exhibit an average  $\Delta^{17}\text{O}$  value of  $-6.9 \pm 1.5\text{‰}$  ( $n=28$ ). The  
422 O-isotopic zoning profile in this CAI and those observed in the remaining inclusions are different  
423 from those discussed above. Such trends of increasing  $^{16}\text{O}$  enrichment outward are referred to as  
424 “reverse” oxygen isotopic zoning in this work.

425 ALH3: A traverse across the outer margin of compact Type A inclusion ALH3 and  
426 interior melilite spots positioned at the ends of three additional traverses focused on its WL rim  
427 were measured (Fig. 9E). Melilite at the inclusion edge and within the outermost  $100 \mu\text{m}$  of this  
428 traverse (diamonds) has an average  $\Delta^{17}\text{O}$  of  $-7.7 \pm 1.4\text{‰}$  ( $n=6$ ), whereas melilite located  $>100 \mu\text{m}$   
429 inward exhibits an average  $\Delta^{17}\text{O}$  value of  $-5.2 \pm 1.5\text{‰}$  ( $n=7$ ). When analyses of melilite near the  
430 WL rim/interior boundary from the other traverses are included, the average  $\Delta^{17}\text{O}$  within the first  
431  $<100 \mu\text{m}$  drops slightly to a value of  $-8.3 \pm 1.1\text{‰}$  ( $n=11$ ), which appears distinct from the  
432 interior. The  $\Delta^{17}\text{O}$  values of secondary minerals in ALH3 are not shown in Figure 9E, but are  
433 near zero, distinct from those of adjacent, primary melilite.

434 Ef-1: The traverse across the margin of Ef-1 also shows a reverse sense of O-isotopic  
435 zoning (Fig. 9F). Melilite within  $100 \mu\text{m}$  of the edge of Ef-1 exhibits an average  $\Delta^{17}\text{O}$  value of -  
436  $5.0 \pm 1.6\text{‰}$  ( $n=8$ ), whereas the interior is slightly less  $^{16}\text{O}$ -rich ( $\Delta^{17}\text{O} = -1.9 \pm 1.3\text{‰}$ ,  $n=6$ ). A single  
437 interior spinel grain is much more  $^{16}\text{O}$ -rich,  $\Delta^{17}\text{O} = -21\text{‰}$ , than any of the interior melilite.

438  
439 *Isotopic heterogeneity among Wark-Lovering rim layers*

440 In all of the CAIs studied, the WL rims exhibit extreme O-isotopic heterogeneity (up to  
441  $\sim 25\text{‰}$ ), whether the interiors are normal or reversely zoned. In most cases, the WL rims exhibit  
442 changes in  $\Delta^{17}\text{O}$  over small spatial scales, e.g.,  $\leq 10 \mu\text{m}$ . Results are illustrated in Figure 10. Data  
443 for multiple traverses are plotted together. In order to account for local differences in layer  
444 thickness between traverses, offsets to the absolute positions of some analyses have been made  
445 to eliminate the appearance of mineral mixing. To accurately show intra-layer zoning, however,  
446 no adjustments were made within individual traverses on a given mineral layer.

447 A37: No new measurements were performed on the rim of this compact Type A  
448 inclusion; data shown in Figure 10A are from J. Simon *et al.* (2011). The WL rim is  $\sim 50$  to  $100$   
449  $\mu\text{m}$  thick and consists of a layered mineral sequence, from the interior outward, of  
450 hibonite $\pm$ melilite, spinel (enclosing perovskite), melilite/nepheline, pyroxene grading outward  
451 from Ti-bearing to Al-rich diopside, and an outermost layer of olivine (Fig. 4C). The melilite at  
452 the edge of the inclusion has an average  $\Delta^{17}\text{O}$  value of  $-2.2 \pm 3.0\text{‰}$  ( $n=6$ ). Considerations of its  
453 distinct sodium abundance and texture (Fig. 4D) led J. Simon *et al.* (2011) to suggest that this

454 melilite may represent the initial stage of rim formation. Hibonite yields a  $\Delta^{17}\text{O}$  value of -17‰  
455 that is indistinguishable from that measured in neighboring perovskite enclosed within spinel.  
456 Spinel yields an average  $\Delta^{17}\text{O}$  value of  $-23.1 \pm 1.4\text{‰}$  (n=15). The pyroxene layer exhibits reverse  
457 O-isotopic zoning, where the inner pyroxene has  $\Delta^{17}\text{O}$  up to -6‰ and the outer pyroxene has an  
458 average  $\Delta^{17}\text{O}$  value of  $-20.9 \pm 1.8\text{‰}$  (n=7) (Fig. 10A). The innermost portion of the pyroxene  
459 layer lies in direct contact with a ~10-20  $\mu\text{m}$  layer of melilite+nepheline (incorrectly identified as  
460 sodalite by J. Simon *et al.*, 2011) that has a planetary-like O-isotopic composition. The olivine  
461 layer exhibits a wide range of  $\Delta^{17}\text{O}$  values, from -24 to -6‰. Backscattered electron images  
462 reveal localized, less forsteritic regions of olivine, and on average, the relatively FeO-rich olivine  
463 tends to have slightly higher and less variable  $\Delta^{17}\text{O}$  (values range from -16 to -9‰).

464 Egg-6: This Type B1 inclusion, with relatively  $^{16}\text{O}$ -poor, nearly isotopically  
465 homogeneous melilite, is surrounded by a simple, two-layer, spinel-pyroxene WL rim sequence  
466 (Fig. 6). The FeO content of the spinel increases outward; innermost, magnesian spinel contains  
467 discontinuous lenses of Ti-rich pyroxene and isolated perovskite (Fig. 6B, C). A NanoSIMS  
468 traverse across the rim starts near the outer point of Traverse 2, within the interior, and continues  
469 across the rim (Fig. 10B). Analyses were also made of aluminous diopside, spinel, and  
470 perovskite enclosed in the spinel layer. Ti-rich pyroxene has  $\Delta^{17}\text{O}$  values that range from -4 to -  
471 2‰ (n=2), indistinguishable from most perovskite. Three of the four perovskite grains analyzed  
472 have  $\Delta^{17}\text{O}$  values of -4 to -1‰; the outermost perovskite grain has a  $\Delta^{17}\text{O}$  value of -10‰. The  
473 outer, diopside layer exhibits reverse O-isotopic zoning, with the innermost spot having  $\Delta^{17}\text{O}$  of -  
474 4‰ and the outer spot a  $\Delta^{17}\text{O}$  value of -13‰. Ti-rich pyroxene grains enclosed in the spinel layer  
475 are notably  $^{16}\text{O}$ -poor compared to both the outer part of the diopside layer and the Ti-rich  
476 pyroxene in the interior of the CAI.

477 TS4: This Type B2 inclusion has relatively  $^{16}\text{O}$ -poor, isotopically homogeneous melilite  
478 in its interior and is surrounded by a ~15 to 60  $\mu\text{m}$  thick WL rim composed, from interior  
479 outward, of spinel, Ti-bearing pyroxene grading into aluminous pyroxene, and a thick, semi-  
480 continuous layer of olivine that underlays the accretionary olivine rim (Fig. 7B). The  
481 discontinuous outer region of sodalite and patches of secondary plagioclase that occur just inside  
482 of, and are partially intermingled with, the spinel layer exhibit near-zero  $\Delta^{17}\text{O}$ . The interface  
483 between the ~10-25  $\mu\text{m}$  thick spinel layer and interior spinel can be difficult to define in this  
484 sample, but spinel at the interior's edge has a  $\Delta^{17}\text{O}$  value of -20‰, similar to spinel in the interior  
485 and less  $^{16}\text{O}$ -rich than observed in some other CAI rims (e.g., Egg-6). Analysis of the ~5  $\mu\text{m}$ -  
486 thick, zoned pyroxene layer yields a  $\Delta^{17}\text{O}$  of -6‰ (Fig. 10C). The  $\geq 30$   $\mu\text{m}$  thick, outer olivine

487 layer is heterogeneous in O-isotopic composition, exhibiting  $\Delta^{17}\text{O}$  values ranging from -20 to  
488 0‰. Normal isotopic zoning is observed within the coherent olivine layer, as analyses within  
489  $\sim 25\ \mu\text{m}$  of the pyroxene layer exhibit  $\Delta^{17}\text{O}$  values that range from -21 to -6‰ (n=4), whereas the  
490 remaining measurements closer to the matrix range from -5 to 0‰ (n=3), indistinguishable from  
491 a measurement in the accretionary rim that has a  $\Delta^{17}\text{O}$  value of 0‰.

492 L6: This minimally altered compact Type A inclusion is surrounded by a continuous and  
493 locally thick (up to  $100\ \mu\text{m}$ ) layer of spinel intergrown with melilite, with reverse O-isotopic  
494 zoning at the edge of the melilite interior. As shown in Figure 10D, spinel grains have an average  
495  $\Delta^{17}\text{O}$  value of  $-24.9 \pm 1.2\text{‰}$  (n=8). In the innermost chemically zoned melilite layer(s) that  
496 includes Mel-1 and Mel-2 (Fig. 8B),  $\Delta^{17}\text{O}$  is -4‰ (n=3), but  $\Delta^{17}\text{O}$  in melilite in the outer spinel-  
497 melilite layer (Mel-3), varies from -5‰, like a majority of interior melilite, to -26‰. Diopside in  
498 Al-pyx-5, the outermost layer, has  $\Delta^{17}\text{O}$  values ranging from -14‰ to -22‰ (n=4), and averages  
499 -18‰. Among the pyroxene layers,  $\Delta^{17}\text{O}$  increases inward from Al-pyx-5, to Ti-pyx-4, with an  
500 average of -17‰, to Ti-Pyx-3, with an average of -13‰, to Ti-pyx-1, at -10‰.

501 ALH3: This compact Type A inclusion has subtle, reverse O-isotopic zoning in the  
502 interior. The primary WL rim traverse reflects a continuation of Traverse 4, originating from the  
503 interior. Additional WL rim analyses come from a sub-parallel traverse (#3)  $\sim 20\ \mu\text{m}$  away and a  
504 pair of traverses (#1 and #2) across a WL rim sequence lining the bottom of an embayment,  
505 located at the edge of a matrix pocket within ALH3. Spinel yields an average  $\Delta^{17}\text{O}$  value of  $-22.0$   
506  $\pm 1.9\text{‰}$  (n=7) (Fig. 10E), while pyroxene measurements are more variable, averaging  $-11.0 \pm 5\text{‰}$   
507 (n=7). There is evidence for reverse zoning across the pyroxene (Fig. 10E), where  $\Delta^{17}\text{O}$  values  
508 increase inward across two separate traverses, from -22 to -4‰ and from  $\Delta^{17}\text{O} = -11$  to -7‰. The  
509 pyroxene analyses with the highest  $^{16}\text{O}$  abundances along each traverse are those furthest away  
510 from the spinel layer. All measured olivine lies within an  $\sim 20\ \mu\text{m}$ -thick layer at the interface  
511 between the WL rim and the matrix. Olivine yields  $\Delta^{17}\text{O}$  values of -26, -25, -11, and 0‰; the two  
512  $^{16}\text{O}$ -rich analyses come from the same grain.

513 Ef-1: This minimally altered compact Type A inclusion is surrounded by a simple, two-  
514 layer, spinel-pyroxene WL rim sequence, with a melilite interior exhibiting reverse O-isotopic  
515 zoning. Two analytical traverses transect the rim (Fig. 10F). The spinel layer,  $\sim 5$ - $10\ \mu\text{m}$  thick  
516 and interfingered with the margin of interior melilite, has an average  $\Delta^{17}\text{O}$  value of  $-21.4 \pm 3.2\text{‰}$   
517 (n=4), similar to that of interior spinel. The pyroxene layer is  $\sim 10$ - $15\ \mu\text{m}$  thick and chemically  
518 zoned from Ti-rich to aluminous diopside. A single traverse across the pyroxene layer reveals  
519 reverse O-isotope zoning, from a  $\Delta^{17}\text{O}$  value of -11‰ near the  $^{16}\text{O}$ -rich spinel layer and -20‰

520 near the contact with the fine-grained, olivine-dominated matrix, which has a  $\Delta^{17}\text{O}$  of  $-1.6 \pm 5\%$   
521 (n=4). No secondary mineralization was observed in the WL rim of this inclusion (Fig. 2).

522

523

## DISCUSSION

524

### Characteristics of Oxygen Isotopic Exchange in the Interiors and Rims of CAIs

526 A number of processes can be envisioned that can potentially explain the heterogeneous  
527 distribution of O-isotopic compositions in the interiors and WL rims of CAIs (e.g., Clayton et al.,  
528 1977; Ryerson and McKeegan, 1994; Yurimoto *et al.*, 1998; Yoshitake *et al.*, 2005; Aleon *et al.*,  
529 2007; J. Simon *et al.*, 2011; Park *et al.*, 2012). Exchange between a molten CAI with an  $^{16}\text{O}$ -rich  
530 protosolar composition and a gaseous reservoir with a planetary, relatively  $^{16}\text{O}$ -poor isotopic  
531 composition could occur rapidly, before any crystals form, or more slowly, while the CAI  
532 crystallizes. The first case would produce a CAI in which all minerals have a uniform, relatively  
533  $^{16}\text{O}$ -poor, planetary-like O-isotopic composition. This is never observed. The second case would  
534 yield a CAI in which  $\Delta^{17}\text{O}$  is lowest in spinel, the phase with the highest crystallization  
535 temperature, highest in pyroxene and anorthite, the solidus phases, and intermediate in melilite.  
536 This is also never observed. An alternative scenario could involve O-isotopic exchange between  
537 a solid CAI of protosolar O-isotopic composition and a near-zero  $\Delta^{17}\text{O}$  planetary oxygen  
538 reservoir on the chondrite parent body. This parent body scenario would yield progressively less  
539 negative  $\Delta^{17}\text{O}$  values in melilite from the center of the CAI to the edge, which is seen only in  
540 some CAIs (e.g., Egg-6). A parent body scenario would also likely lead to less negative  $\Delta^{17}\text{O}$   
541 values from the inside out within a given mineral layer and between similar phases from the  
542 inner to the outer rim, which was not observed in this study. For CAI interiors, the remaining  
543 possibility is exchange between solid CAIs of protosolar O-isotopic composition and several  
544 nebular gas reservoirs with distinct O-isotopic compositions. It should be noted that some  
545 interactions could have occurred between nebular gas and inclusions in which both had similar  
546 isotopic compositions. In this case the solid-gas interaction would leave little to no isotopic  
547 record. It is also possible that some WL rim growth involved a non-solar gas with a protosolar O-  
548 isotopic composition. For rim layers, the remaining possibility is growth of different layers from  
549 distinct nebular reservoirs, most dramatically indicated by reversals in the gradients of isotopic  
550 compositions observed in the present work.

551 Despite the wealth of O-isotopic measurements of CAIs, only a few studies have  
552 systematically addressed, at high spatial resolution, the radial distribution of O-isotopes in CAIs  
553 and their rims. In examples that do exist, including those reported herein, there are some general

554 features that provide important diffusion model input parameters and allow us to make specific  
555 predictions for environment(s) from which CAIs formed and evolved. Illustrative model results  
556 shown in Table 4 include examples of complete oxygen exchange between protosolar and near  
557 planetary compositions for a variety of end-member cases (“Idealized CAIs”) involving molten  
558 objects at 1773 K or 1973 K and 1 bar; solid objects with no defects at 1400 K and  $P^{\text{tot}}=10^{-3}$  bar  
559 and 1500 K and  $P^{\text{tot}}=10^{-2}$  bar; and solid objects with significant lattice dislocations, both large (2  
560 cm) and smaller (0.5 cm) CAI sizes, at 1400 K and 1500 K, respectively. Table 4 also  
561 summarizes results that reflect the timescales for diffusive exchange to reproduce the isotopic  
562 compositions characteristic of the interiors and the external isotopic reservoirs implied by the  
563 “Studied CAIs” for nebular and planetary scenarios. These models assume mean temperatures  
564 (pressures) of 1400 K ( $P^{\text{tot}}=10^{-3}$  bar) and 900 K (1 bar), respectively. Representative diffusion  
565 models are compared to the isotopic zoning profiles in the interiors of the inclusions and shown  
566 in Figure 9. Although such models are non-unique, a comparison between the model curves and  
567 the measured profiles can be used to determine plausible temperature-dependent timescales of O-  
568 isotopic exchange in the CAIs, and ultimately used to constrain the possible environments where  
569 exchange occurred, i.e., nebular (Shu *et al.*, 2001; Cuzzi *et al.*, 2003; Boss *et al.*, 2012) or on a  
570 planetary body (Wasson *et al.*, 2001).

571 Model curves were computed to reflect the exchange of O-isotopes in each CAI to  
572 investigate the possibility that the  $\Delta^{17}\text{O}$  profiles developed following crystallization, assuming  
573 each CAI subsequently exchanged oxygen with a reservoir of distinct O-isotope composition. It  
574 is possible that the progress of isotopic exchange due to reheating occurred in numerous short  
575 (hours to days) events within the solar nebula (e.g., Young *et al.*, 2005). None of these  
576 isothermal models reproduce actual heating events, but allow assessment of the plausibility of  
577 exchange by solid-state diffusion. Based on the broad trends and relative lack of localized O-  
578 isotopic heterogeneity observed across the melilite interiors of the studied inclusions, the models  
579 summarized in Table 4 are those that consider diffusion length scales at the inclusion scale rather  
580 than the individual mineral grain scale. To model the profiles observed in L6, Ef-1, and ALH3,  
581 the CAIs exhibiting relatively  $^{16}\text{O}$ -poor interiors with melilite margins that are comparatively  
582  $^{16}\text{O}$ -rich (i.e., exhibit reverse zoning), starting conditions for a second step of isotopic exchange  
583 assumed an interior that was previously enriched in “heavy” oxygen and uniformly  $^{16}\text{O}$ -poor, -5,  
584 0, and -3‰, respectively. More complicated models, where the distribution of O-isotopes within  
585 the interior is non-uniform, e.g., like in A37, would be necessary to fully understand the  
586 timescales and temperatures required to explain the reversely zoned profiles. Models that match  
587 the relatively  $^{16}\text{O}$ -poor and nearly uniform melilite profiles of the Type B inclusions (Egg-6 and

588 TS4) are shown in Figure 9 although it is debatable whether a nebular process provides the best  
589 explanation for the O-isotopic compositions of their melilite.

590 The individual models for the inclusions do not take into account enhanced-diffusivity  
591 due to crystal lattice dislocations (Ryerson and McKeegan, 1994), fast diffusion pathways along  
592 grain boundaries, or the presence of a fluid phase. Dislocations in minerals contained in CAIs are  
593 generated by exposure to ionizing radiation emitted from the protoSun, and their density  
594 increases with exposure time (Kwok *et al.*, 1978). For example, in an Allende CAI Barber *et al.*  
595 (1984) found dislocation densities  $<10^8/\text{cm}^2$  in spinel and pyroxene and  $\sim 10^9/\text{cm}^2$  in melilite.  
596 Ryerson and McKeegan (1994) calculated that equilibration of oxygen isotopes in melilite at  
597 temperatures approaching the solidus ( $\sim 1500$  K) would happen within years, an order of  
598 magnitude faster than in dislocation-free grains (see “Idealized CAIs” with “defects” included in  
599 Table 4). On the other hand, Ryerson and McKeegan (1994) find that equilibration times exceed  
600  $10^6$  years regardless of the dislocation density within melilite at temperatures relevant to  
601 chondrite parent bodies (e.g.,  $<1000$  K). It follows that significant isotopic zoning like that seen  
602 within the melilite interiors of A37 and L6 should be rare. Therefore these rare inclusions  
603 possibly indicate rapid accretion onto a parent body, as an inclusion with significant dislocations  
604 would likely be efficiently homogenized in the nebula, leading to the relatively homogeneous  
605 melilite interiors documented in other CAIs.

606

### 607 **Effect of Parent Body Alteration on Oxygen Isotopes of Refractory Inclusions**

608 Inclusions in Allende, Efremovka, and Leoville contain evidence of secondary alteration.  
609 This alteration is largely due to hydrous fluids or gas, assisted by heating in asteroidal and  
610 nebular environments (Brearley, 1997; Huss *et al.*, 2006; Hutcheon *et al.*, 1998, and references  
611 therein). The effect of water on intra-mineral (volume) diffusion is a subject of debate, but it  
612 likely enhances exchange rates at parent body temperatures, but apparently not significantly at  
613 nebular ones ( $>1000$  K), e.g., Ingrin *et al.* (2001) and Ryerson and McKeegan (1994). Noble gas  
614 data indicative of the abundance and survival of presolar grains (Huss *et al.*, 2003) and Raman  
615 spectroscopic studies of organic material (Bonal *et al.*, 2006) suggest that CV3 meteorites  
616 experienced moderate peak temperatures,  $\sim 500$ - $900$  K, during parent body processing (Huss *et al.*  
617 *et al.*, 2006). The timescale for producing these peak temperatures, e.g.,  $\leq 800$  K on the Allende  
618 parent body, primarily reflects parent body size and the initial abundance and subsequent decay  
619 of  $^{26}\text{Al}$  (i.e.,  $^{26}\text{Al}/^{27}\text{Al}_0 = 3\text{-}5 \times 10^{-6}$ ). Young (2001) and Kunihiro *et al.* (2004) estimate that it  
620 would take more than  $2 \times 10^6$  years to reach these peak temperatures and that they would not  
621 persist for more than  $5 \times 10^5$  years. Other potential sources of heat include magnetic induction and  
622 impacts (Rubin, 1995), although neither induction nor collisional heating are likely to result in

623 the relatively high temperatures required by the global thermal metamorphism of chondrite  
624 parent bodies (Keil *et al.*, 1997). The timescale of radiogenic heating is incompatible with the  
625 magnitude of O-isotope exchange inferred for the studied CAIs, as unrealistically long periods of  
626 time,  $\sim 10^6$ - $10^8$  years, would be required (Table 4; Yurimoto *et al.*, 1989; Ryerson and  
627 McKeegan, 1994; Ingrin *et al.*, 2001).

628 If the O-isotopic profiles in the interiors of CAIs were established by incomplete  
629 exchange with a planetary isotopic reservoir, it is noteworthy that there are larger shifts within  
630 the melilite in Ef-1 and L6, both from reduced CV3 chondrites, than in A37, from an oxidized  
631 CV3 chondrite. Moreover, much of the melilite in the Type A CAI interiors appears to be  
632 “lighter” than typical bulk O-isotopic compositions of inclusions from CV3 chondrites.  
633 Additionally, L6, ALH3 and EF-1 record O-isotopic gradients within their interiors that exhibit  
634 relative  $^{16}\text{O}$ -enrichment trends towards their edges. Although sometimes subtle, this “reverse”  
635 zoning is not consistent with late parent body exchange because the latter would produce  
636 “normal” zoning. Collectively, these observations argue that the primary process(es) responsible  
637 for incorporating relatively  $^{16}\text{O}$ -poor oxygen into the CAI interiors occurred in the nebula rather  
638 than the parent body. Finally, the O-isotopic heterogeneity within the rim layers surrounding the  
639 CAIs, and especially the presence of the relatively  $^{16}\text{O}$ -rich, fine-grained (i.e., high surface area)  
640 melilite in the Wark-Lovering rim of L6 provides strong evidence that some coarse-grained  
641 melilite in the CAI interiors became relatively  $^{16}\text{O}$ -poor prior to rim formation.

642 Among the CAIs studied here, it is also noteworthy that the evidence for isotopic  
643 exchange is largely uncorrelated with the degree of secondary alteration discernible from  
644 petrographic study. This can be clearly seen by the fact that both A37, whose interior records  
645 only “normal” isotopic exchange, and L6, with an interior that records “reverse” zoning and  
646 which likely had a much more complex and evolved isotopic exchange history than A37, contain  
647 minimal amounts of secondary alteration products. It is therefore concluded that the primary  
648 mineral assemblages within CAIs experienced minimal O-isotopic exchange on their parent  
649 bodies.

650

### 651 **Nebular Isotopic Exchange with CAI Interiors**

652 A37: The interior of this inclusion is “normally” zoned, with  $\Delta^{17}\text{O}$  values in melilite  
653 increasing monotonically from  $-17.5 \pm 0.8\text{‰}$  ( $n=20$ ) in the interior to  $-2.2 \pm 3.0\text{‰}$  ( $n=6$ ) at the  
654 inclusion edge (Fig. 9A). New spinel analyses in the present study from the interior of A37 are  
655 significantly more  $^{16}\text{O}$ -rich ( $\Delta^{17}\text{O} \sim -29\text{‰}$ ) than both the new and previously reported interior  
656 melilite data (J. Simon *et al.*, 2011). A similar oxygen diffusion model was employed in that

657 work as in the present study but, since previously no interior spinel had been measured, J. Simon  
658 *et al.* (2011) concluded that a single-step, solid-state diffusion model could explain the O-  
659 isotopic profile of A37. The new spinel data (Fig. 9A), however, have the usual protosolar  $\Delta^{17}\text{O}$   
660 of  $\sim -29\text{‰}$ , indicating the likelihood that the entirety of the A37 interior formed initially with this  
661  $\Delta^{17}\text{O}$  value. The red curve in Figure 9A is representative of the mismatch of single-step models  
662 for A37. All such temperature-time models that reproduce the relatively elevated  $\sim -18\text{‰}$  value  
663 of the interior yield too shallow a curvature to be considered a good match to the data. More  
664 likely, A37 experienced an early oxygen exchange event that reset melilite to an intermediate  
665  $\Delta^{17}\text{O}$  value (step 1), the relatively uniform value measured in the interior, before melilite at its  
666 margin exchanged further with a near-zero  $\Delta^{17}\text{O}$  planetary reservoir (step 2). The black curves in  
667 Figure 9A represent a family of two-step diffusion models with temperature-time parameters of  
668 1400 K and  $\sim 2 \times 10^4$  years in step 1 and 1400 K and  $\sim 1.6 \times 10^4$  years for step 2, which yield a  
669 good match to the measurements. Although elevation of the  $\Delta^{17}\text{O}$  value in interior melilite by  
670  $\sim 10\text{‰}$  relative to the spinel could be due to exchange while the CAI was partially molten,  
671 exchange that led to the measured zoning profile can only be fit at subsolidus temperatures.

672 Egg-6 and TS4: Interior melilite in Type B CAIs Egg-6 and TS4 differs from that in the  
673 Type A CAIs of this study in having near-zero  $\Delta^{17}\text{O}$  values at their margins and nearly uniform  
674 and relatively high values, mostly between 0 and  $-5\text{‰}$ , throughout the rest of their interiors (Figs.  
675 9B, C). Assuming that all CAIs started with protosolar,  $^{16}\text{O}$ -rich compositions, these values  
676 indicate nearly complete exchange with a relatively  $^{16}\text{O}$ -poor reservoir in the solid-state. The  
677 melilite interiors of both Type B CAIs can be matched with single-step models (e.g., black  
678 curves in Fig. 9B), but TS4 appears to require at least two-steps (Fig. 9C) as discussed below. A  
679 diffusion model for Egg-6 with temperature-time parameters of 1400 K and  $\sim 2.8 \times 10^5$  years  
680 yields a good match to the subtle gradient exhibited by melilite and anorthite measurements that  
681 comprise Traverse 2 (bold curve in Fig. 9B). A similar model shown by the upper thin black  
682 curve run for  $3.0 \times 10^5$  model years passes through all of the Egg-6 melilite, including those in  
683 Traverse 1 that are suspected to reflect some contamination by secondary mineralization.

684 In Egg-6, fassaite has higher  $\Delta^{17}\text{O}$ ,  $\sim -18\text{‰}$ , than spinel,  $\sim -25\text{‰}$ , while, in TS4, these  
685 phases have nearly equal  $\Delta^{17}\text{O}$  values of  $\sim -22\text{‰}$ , rather elevated compared to the protosolar  
686 value. Explaining the difference between fassaite and spinel in Egg-6, or the lack thereof in TS4,  
687 by a single subsolidus diffusion process or heating event is difficult. The difference in O-isotopic  
688 composition between spinel, fassaite and melilite in Egg-6 likely reflects differential subsolidus  
689 exchange with a relatively  $^{16}\text{O}$ -poor reservoir, whereby fassaite exchanged more thoroughly than  
690 spinel, and melilite more extensively than fassaite, as suggested originally by Clayton *et al.*

691 (1977). This could have happened on the parent body or in the nebula. Despite abundant  
692 evidence for remelting in Type B CAIs it is unlikely that the preferential incorporation of  
693 “heavy” oxygen in melilite occurred while the inclusion was partially molten because we know  
694 from experimental phase equilibria that the pyroxene would have crystallized after most of the  
695 melilite (Stolper, 1982).

696 Because fassaite and spinel have distinct oxygen diffusivities, their similar but elevated  
697  $\Delta^{17}\text{O}$  values suggest that TS4 exchanged thoroughly with a nebular gas reservoir with  $\Delta^{17}\text{O} \approx -$   
698 20‰, intermediate between the protosolar and planetary values. This exchange could have  
699 happened while the inclusion was a melt (in hours to days) or in the solid-state (Table 4). Model  
700 curves (Fig. 9C) reflect two-steps of exchange, with the intermediate  $\Delta^{17}\text{O}$  value recorded by  
701 spinel and fassaite interpreted to have preserved the shift from the protosolar  $\Delta^{17}\text{O}$  (step  
702 1), before melilite exchanged further with a planetary  $\Delta^{17}\text{O}$  value (step 2). It is notable that the  
703 intermediate composition modeled by step 1 is similar to that of spinel in the rims of Type A  
704 CAIs Ef-1, A37, and E49 of Alton *et al.* (2007), and most of the melilite in the interior of A37.  
705 Both steps of exchange may have occurred prior to formation of the WL rim, whose innermost  
706 spinel is much more  $^{16}\text{O}$ -rich (Fig. 10C). Representative diffusion models with temperature-time  
707 parameters of 1400 K and  $\sim 2 \times 10^4$  years in step 1 and 1400 K and  $\sim 3 \times 10^4$  years for step 2 yields  
708 an acceptable match to the measurements (black curves in Fig. 9C).

709 L6: The outer margin of this inclusion is “reversely” zoned, with  $\Delta^{17}\text{O}$  values in melilite  
710 decreasing monotonically from a relatively uniform value of  $\sim -7$ ‰ in the interior to  $\sim -20$ ‰ at  
711 the margin (Fig. 9D). For reversely zoned CAIs, the model curves were calculated in two steps  
712 as above, except that in the second step the interior melilite values were used for the initial CAI  
713 value and the nebular gas reservoir was assumed to have the same  $\Delta^{17}\text{O}$  as the spinel in the WL  
714 rims (see Table 4). Assuming that the L6 precursor grew originally from a relatively  $^{16}\text{O}$ -rich  
715 protosolar gas, a majority of its melilite interior later exchanged with a reservoir having a  
716 relatively  $^{16}\text{O}$ -poor composition (step 1). A diffusion model with temperature-time parameters of  
717 1400 K and  $\sim 3 \times 10^4$  years approximates the  $\Delta^{17}\text{O}$  of its melilite interior (Table 4). In detail, the  
718 representative model listed in Table 4 is run long enough to produce an interior value that  
719 exceeds the uniform value of  $\sim -7$ ‰ in the interior because the extent of subsequent exchange  
720 needed (in step 2 below) to produce the rather extreme  $^{16}\text{O}$ -enrichment ( $-20$ ‰) at the edge would  
721 drop the modeled  $-5$ ‰ interior value back down to the measured value of the interior ( $\sim -7$ ‰).  
722 Based on the match of the model diffusion profile to the O-isotopic composition of the melilite  
723 observed at the edge of the inclusion, L6 likely experienced a second exchange event (step 2)  
724 that exposed the relatively  $^{16}\text{O}$ -poor interior to a relatively  $^{16}\text{O}$ -rich nebular gas, a process that

725 would have taken  $\sim 2.6 \times 10^4$  years at 1400 K (Table 4). The L6 profile, and the isotopic  
726 composition of its interior and rim spinel ( $\Delta^{17}\text{O} \sim -20$  to  $-25\%$ ) are very similar to those of E49  
727 (Aleon *et al.*, 2007), and both inclusions may have had similar formation histories.

728 Ef-1 and ALH3: In contrast to the near-zero  $\Delta^{17}\text{O}$  values measured at the margins of A37  
729 and the Type B CAIs, Ef-1 and ALH3 exhibit relative  $^{16}\text{O}$ -enrichments at their melilite margins  
730 with average  $\Delta^{17}\text{O}$  values of  $-8 \pm 1\%$  (n=11), and  $-5 \pm 2\%$  (n=8), respectively (Fig. 9E and F).  
731 Although less extreme than the  $\Delta^{17}\text{O} \sim -20\%$  measured at the margin of L6, these reversals in O-  
732 isotopic zoning profiles also imply two exchange events. The interiors of both CAIs record an  
733 event that transformed their assumed protosolar starting compositions into relatively  $^{16}\text{O}$ -poor  
734 compositions (step 1), followed by exposure to a more  $^{16}\text{O}$ -rich nebular gas, producing the higher  
735  $^{16}\text{O}$  abundances at the CAI margins (step 2). Diffusion models with temperature-time parameters  
736 of 1400 K and  $10^3$  years and 1400 K and  $1.9 \times 10^4$  years, approximates the  $\Delta^{17}\text{O}$  of their  
737 respective melilite interiors (step 1's). Because the CAIs are rather large (originally  $\geq 0.5$  cm)  
738 even the slight  $^{16}\text{O}$ -enrichments detected at the margins of Ef-1 and ALH3, require relatively  
739 long exposure times,  $5 \times 10^3$  and  $1.9 \times 10^4$  years, respectively (step 2's). The higher melting  
740 temperature of the gehlenitic melilite composition characteristic of ALH3 permits subsolidus  
741 model temperatures higher than 1400 K. In these relatively high temperature calculations  
742 modeled exchange in ALH3 could be up to  $\sim 5$  times faster.

743 In general, the modeled timescales for O-isotope exchange are comparable to those  
744 reported by J. Simon and Young (2011), based on the Mg-isotope profiles in coarse-grained  
745 CAIs. Unlike spinel, in which oxygen diffuses much more slowly than magnesium, oxygen  
746 diffusivities in melilite are only slightly lower than magnesium diffusivities (LaTourrette and  
747 Hutcheon, 1999; J. Simon and Young, 2011, and references therein). Based on this  
748 complementarity, it follows that a majority of the oxygen data reported herein and the  
749 magnesium data reported for similar inclusions (e.g., Fahey *et al.*, 1987a; J. Simon *et al.*, 2005; J.  
750 Simon and Young, 2011; Bullock *et al.*, 2013) from CV3 chondrites imply early, open-system  
751 exchange, and resetting in the solid-state (Fahey *et al.*, 1987b; J. Simon and Young, 2011; J.  
752 Simon *et al.*, 2005; Young *et al.*, 2005), which could reflect a common early solar system  
753 reprocessing event and/or environment.

754

### 755 **Nebular Scenarios Implied by the Oxygen Isotopic Records of Wark-Lovering Rim Layers**

756 As first suggested by Wasserburg *et al.* (1977) and confirmed by Cosarinsky *et al.* (2005)  
757 and J. Simon *et al.* (2005), at least some WL rims formed within  $10^5$  years of CAI crystallization.  
758 Three mechanisms are frequently invoked to explain part or all of their formation: (1) “flash

759 heating”, whereby inner layers formed by melting and/ or evaporation during intense heating  
760 (Boynton and Wark, 1985; Wark and Boynton, 2001); (2) “subsolidus deposition”, whereby  
761 outer layers formed sequentially by condensation during cooling and/or vapor deposition due to  
762 an increased gas pressure or changing composition (Wark and Lovering, 1977; Fahey *et al.*,  
763 1987b; J. Simon *et al.*, 2005); and (3) growth due to “chemical potential gradients”, where the  
764 common mineral layer sequence of spinel±hibonite→melilite→pyroxene→olivine was produced  
765 simultaneously by metasomatic reaction with nebular gas (Wark and Lovering, 1977;  
766 MacPherson *et al.*, 1981; Ruzicka, 1997) or from elements in the gas phase alone (J. Simon *et*  
767 *al.*, 2005). The O-isotope variability in WL rims, discussed next, demonstrates that growth  
768 occurred from distinct gas reservoirs, that gas chemistry contributing to mineral growth and  
769 potentially leading to higher more planetary  $f_{O_2}$ , can be decoupled from gas isotopic  
770 compositions, and that, similar to the interiors, the initial O-isotope composition of some rim  
771 layers may have been later modified by exposure to distinct gas reservoirs.

772         Several important observations can be made from the present work: (1) Pyroxene found  
773 in WL rims tends to exhibit reverse O-isotopic zoning. That is, when multiple analyses were  
774 made, either within a single layer or among the multiple pyroxene layers surrounding L6 and  
775 Egg-6 (Fig. 10) the outermost spots (i.e., those located closer to the matrix) tend to be relatively  
776  $^{16}\text{O}$ -rich. This observation is difficult to explain by simple mixing between oxygen originally  
777 contained in the inclusion and any near-zero  $\Delta^{17}\text{O}$  oxygen reservoir; (2) For two CAIs (A37, L6),  
778 O-isotopic compositions at the edges of their melilite interiors and the innermost layer of the WL  
779 rims are similar—possibly implying a genetic relationship. In an analogous way, the melilite  
780 interiors of the other two Type A CAIs (ALH3, Ef-1), which exhibit more subtle O-isotopic  
781 gradients, may record a signature of edgeward  $^{16}\text{O}$ -enrichment related to WL rim formation. In  
782 contrast, the O-isotopic compositions of melilite observed in the two Type B CAIs (Egg-6, TS4)  
783 contain little to no evidence of a relationship with their WL rims, the exception being that in  
784 Egg-6, the perovskite and pyroxene enclosed in spinel in the rim have compositions similar to  
785 melilite at the edge of the interior; (3) spinel found in WL rims typically has compositions that  
786 are slightly less  $^{16}\text{O}$ -rich compared to the protosolar gas composition (Fig. 10), but with  
787 measurable differences among the various CAIs not readily attributable to secondary alteration.  
788 Differences among WL rim spinel compositions could have been derived from initially  
789 protosolar spinel that was cogenetic with CAI interiors (Wark and Lovering, 1982) and  
790 incrementally exchanged when the next layer, e.g., relatively  $^{16}\text{O}$ -poor melilite and/or pyroxene,  
791 was deposited; or they may reflect early rim deposition from gas reservoirs with distinct O-  
792 isotopic compositions; and (4) O-isotopic differences between adjacent zones require that some  
793 mineral layers formed sequentially, rather than contemporaneously as hypothesized by some

794 models in which large chemical potential gradients drove their formation (e.g., Ruzicka, 1997).  
795 The measured isotopic heterogeneity over short length scales is inconsistent with the standard  
796 metasomatic mechanism, which would have likely resulted in a continuous isotopic gradient  
797 because such a model implies that the more refractory elements were scavenged from the interior  
798 and diffusively exchanged with material that was added at the surface. It is still possible that the  
799 WL rim layers grew under a chemical potential gradient (as, for example, suggested by J. Simon  
800 *et al.* 2005), but in such a scenario they condensed directly from the gas and formed from several  
801 gas reservoirs with isotopically distinct compositions.

802 *The interface between WL rims and CAI interiors:* In most CAIs, spinel defines the  
803 boundary between the outer edge of the interior and the innermost rim layer. It is unclear  
804 whether all of the spinel at the edge of an inclusion is part of the rim or not; some probably  
805 formed in the interior, as, for example, suggested by Wark and Lovering (1982). An exception to  
806 the rule is the existence of the innermost melilite and hibonite layer, “below” the spinel layer, in  
807 the WL rim surrounding A37 (see Fig. 4C, D and supplemental material of J. Simon *et al.*,  
808 2011). In this case, new melt at the inclusion edge might have lost Mg, and new, more gehlenitic  
809 melilite, precipitated on the underlying melilite interior, producing the observed sequence of  
810 melilite-on-melilite. This melt could be cogenetic with the spinel-perovskite layer, but its  
811 distinct, relatively high Na content, and relatively  $^{16}\text{O}$ -poor isotopic composition, makes this  
812 scenario unlikely. J. Simon *et al.* (2011) analyzed hibonite in the rim and found that it is  
813 relatively  $^{16}\text{O}$ -rich ( $\Delta^{17}\text{O} \sim -17\text{‰}$ ). The intermediate O-isotopic compositions observed in  
814 hibonite may reflect a reaction between the relatively  $^{16}\text{O}$ -poor, Na-rich melilite at the edge of  
815 the interior (i.e., recording the inclusion’s original exposure to relatively  $^{17,18}\text{O}$ -rich nebular gas)  
816 and the relatively  $^{16}\text{O}$ -rich nebular gas related to formation of the spinel-perovskite layer.  
817 Alternatively, if hibonite is relatively resistant to oxygen exchange compared to melilite, it may  
818 have been relatively  $^{16}\text{O}$ -rich and only partially exchanged with the relatively  $^{17,18}\text{O}$ -rich  
819 reservoir that exchanged with the interior.

820 *Spinel layers:* These layers in WL rims are relatively  $^{16}\text{O}$ -rich, with  $\Delta^{17}\text{O}$  values ranging  
821 from  $-30\text{‰}$  to  $-18\text{‰}$ , with most values  $\leq -20\text{‰}$  (Figs. 9 and 10) and uniform in composition  
822 within a given rim. The possible exception is the spinel layer surrounding Egg-6. A comparison  
823 of X-ray image data and the O-isotope measurements show that its outermost spinel is more  
824 FeO-rich and slightly  $^{16}\text{O}$ -poor compared to some more magnesian spinel closer to the CAI edge.  
825 Substitution of Fe for Mg in spinel often indicates parent body alteration and implies that the  
826 slight shift towards relatively  $^{16}\text{O}$ -poor compositions in the outermost spinel zone could have  
827 happened on the parent body. The spinel layers surrounding A37, Egg-6, and L6 have average

828  $\Delta^{17}\text{O}$  values of  $\sim -25\%$  or less, whereas Ef-1, TS4, and E49 (Aleon *et al.*, 2007) have  $\Delta^{17}\text{O}$   
829 values of  $-20\%$ . The possibility that O-isotopes in some Egg-6 spinel have been partially  
830 exchanged, and yet they are still more  $^{16}\text{O}$ -rich than magnesian spinel in Ef-1, implies that Ef-1  
831 spinel may have originated from a slightly  $^{17,18}\text{O}$ -enriched reservoir. If the measured differences  
832 in  $\Delta^{17}\text{O}$  of 5-10% among the studied inclusions reflect different degrees of O-isotope exchange  
833 upon pyroxene deposition, gradational variations within spinel layers might be expected, as in  
834 Egg-6. But evidence for differential exchange in spinel surrounding the other CAIs is lacking.

835         Based on comparison of trends in the O-isotopic zoning profiles and the compositions of  
836 the WL spinel layers (or melilite layer in the case of A37), rim formation may have affected the  
837 O-isotopic composition of the edges of the interiors of the studied Type A CAIs. In contrast, in  
838 both Type B inclusions studied here, there is no obvious connection between relatively  $^{16}\text{O}$ -rich  
839 spinel in the rims and  $^{16}\text{O}$ -poor melilite in their interiors. Nonetheless, with the possible  
840 exception of spinel in the WL rim surrounding Egg-6, the variability of the spinel data in both  
841 the most pristine (Ef-1 and L6) and most altered (TS4 and ALH3) inclusions provides evidence  
842 that the O-isotopic compositions of most WL rim spinel has little to nothing to do with secondary  
843 mineralization, rather, it likely grew and incorporated oxygen from different, possibly evolving  
844 nebular gas reservoirs.

845         *Pyroxene layers:* All WL rims contain a pyroxene layer. Most pyroxene appears to have  
846 formed in chemical disequilibrium with respect to the interior phases, implying later growth  
847 through metasomatic solid-gas reaction and/or condensation from a non-solar gas (Wark and  
848 Lovering, 1977; Ruzicka, 1997; J. Simon *et al.*, 2005; Han and Brearley, 2012). The reverse O-  
849 isotopic zoning seen in the WL rim pyroxene layers surrounding Ef-1, A37, Egg-6, and ALH3  
850 appears to be more common than normal zoning. The replicate sequences of pyroxene (and  
851 melilite) layers in L6, as well as the distinct O-isotopic compositions of the pyroxene, imply that,  
852 at least in this case, they likely formed sequentially rather than simultaneously.

853         At face value, the presence or lack of  $\text{Ti}^{3+}$  in the pyroxene layers can signify the state of  
854 oxidation during their growth. Redox conditions can be estimated by the equilibrium reactions of  
855 J. Simon *et al.* (2005), which relate the measured activities of pyroxene components, and  
856 estimated temperature and  $P_{\text{SiO}}/P_{\text{Mg}}$  in a coexisting nebular gas. Higher  $\text{Ti}^{3+}/\text{Ti}^{\text{tot}}$  due to the more  
857 reducing conditions expected during formation in a primitive nebular environment might be  
858 expected to correlate with greater  $^{16}\text{O}$  abundance. In the case of the pyroxene layers surrounding  
859 L6, however, the innermost layer (Ti-pyx-1), with the highest  $\text{Ti}^{3+}/\text{Ti}^{\text{tot}}$  exhibits the lowest  $^{16}\text{O}$   
860 abundance, whereas the layer with the lowest measurable  $\text{Ti}^{3+}/\text{Ti}^{\text{tot}}$  has an intermediate  $\Delta^{17}\text{O}$   
861 value of  $-15\%$ . These results imply that the valence state of Ti and the O-isotopic composition of

862 rim pyroxene are not always correlated, indicating a decoupling of the isotopic composition of  
863 the gas from other physicochemical parameters.

864 *Melilite layers:* This phase is absent from some WL rims. Where present, it is typically  
865 between the spinel and pyroxene rim layers and is often intergrown with plagioclase  $\pm$ nepheline,  
866 which are likely products of alteration of the melilite. Exceptions include melilite at the interface  
867 with the interior of Allende A37, and the complicated WL rim surrounding L6 that contains three  
868 distinct occurrences of melilite. Often melilite in rims is relatively  $^{16}\text{O}$ -poor, e.g., Ito *et al.* (2010)  
869 and J. Simon *et al.* (2011). This is the case for the inner sublayers “Mel-1, Mel-2” in the rim of  
870 L6 ( $\Delta^{17}\text{O} = -4\%$ ). The fact that this melilite exhibits zoning in chemical composition (see Fig.  
871 8B) but is homogeneous in O-isotopic composition indicates that there were more cycles of  
872 deposition than are recorded by isotopic differences.

873 In L6, the inner rim O-isotopic homogeneity contrasts sharply with the outermost  
874 occurrence of melilite (Mel-3), which exhibits O-isotopic heterogeneity, with  $\Delta^{17}\text{O}$  values  
875 ranging from -26 to -5‰ (Fig. 10D). A single spinel analysis within the outermost melilite yields  
876  $\Delta^{17}\text{O} = -25\%$ . The granular, relatively fine-grained texture of the outer melilite could indicate a  
877 period of accretion of individual melilite and spinel grains whose isotopic heterogeneity could  
878 have predated deposition, rather than formation *in situ*. Although the significance of this extreme  
879 variability is unclear, it is difficult to envision a scenario in which the fine-grained (i.e., high  
880 surface area) melilite in the outer layer retained its O-isotopic heterogeneity if the uniform,  
881 relatively  $^{16}\text{O}$ -poor isotopic composition of the inner melilite layer(s) resulted from exchange of  
882 initially  $^{16}\text{O}$ -rich melilite with a relatively  $^{16}\text{O}$ -poor reservoir after formation of the outer melilite  
883 layer.

884 *Olivine layers:* At the outermost edges of WL rims, there are generally two types of  
885 olivine layers that can be distinguished texturally. Porous layers consisting of many individual  
886 crystals that tend to fill topographic depressions (clearly seen on TS4, Fig. 7A), are thought to be  
887 accretionary (MacPherson *et al.*, 1985), and are not considered part of the WL rim in the present  
888 work. The outer melilite layer in L6 also has a porous, polycrystalline nature but is considered  
889 part of the WL rim because it is found inside massive, WL rim layers of pyroxene. The other  
890 type of olivine occurs as thin but coherent, wall-like layers containing little pore space, and are  
891 interpreted here as WL rims that may have been vapor deposited (J. Simon *et al.*, 2005; Keller *et al.*  
892 *et al.*, 2013). The heterogeneous O-isotopic compositions in the olivine rim layers of TS4 and  
893 ALH3 and in the accretionary rims of A37 suggest that both types of olivine had complex  
894 histories involving formation from relatively  $^{16}\text{O}$ -rich and  $^{16}\text{O}$ -poor gases (Krot *et al.*, 2002). It is  
895 possible that the olivine in the WL rim, and its isotopic heterogeneity, reflects *in situ*

896 condensation of olivine from a relatively  $^{16}\text{O}$ -poor gas that is “peppered” with a previous  
897 generation of relatively  $^{16}\text{O}$ -rich grains just prior to and/or as the earliest stage of accretionary  
898 rim formation. Elevated levels of FeO in both olivine types may be due to subsequent diffusive  
899 Fe-Mg exchange, and could have occurred without significant modification of the original O-  
900 isotopic composition of the olivine (Fagan *et al.*, 2004b; Cosarinsky *et al.*, 2008).

901

## 902 **Mass-independent Oxygen Reservoirs in the Early Solar System**

903  $\Delta^{17}\text{O}$  variability in the early solar system has been generally attributed to  
904 photodissociation of CO by self-shielding in the optically thin surface of the protosolar disk  
905 (Clayton, 2002; Lyons and Young, 2005; Sakamoto *et al.*, 2007). This may have resulted in  
906 formation of relatively  $^{17,18}\text{O}$ -rich water that spread heterogeneously throughout the disk where  
907 its oxygen was incorporated into silicates. Young (2007) suggested that this process occurs on a  
908 timescale of  $\sim 10^5$  years. Alternatively, heterogeneous enrichment of  $^{17,18}\text{O}$  may have existed very  
909 early in the history of the solar nebula originating from the parental molecular cloud (Yurimoto  
910 and Kuramoto, 2004; Dominguez, 2010).

911 In addition to the protosolar oxygen isotopic composition,  $\Delta^{17}\text{O} \sim -25$  to  $-30\%$ , and the  
912 planetary values,  $\Delta^{17}\text{O} \sim 0$  to  $-5\%$ , that are frequently encountered in CAI materials, another  
913 common composition in this study is  $\Delta^{17}\text{O} \sim -17$  to  $23\%$ . This intermediate composition is found  
914 in the fassaite and spinel in TS4, a majority of the melilite in the A37 interior, and spinel in the  
915 WL rim of Ef-1 in the present work, as well as in the CAI rim studied by Aleon *et al.* (2007).  
916 While the common occurrence of this value may be the fortuitous result of exchange between  
917 inclusions with a protosolar composition and an  $^{16}\text{O}$ -depleted reservoir, it is also possible that  
918 there was a distinct reservoir of intermediate oxygen isotopic composition sufficiently  
919 widespread and long-lived to have left its imprint on all of these materials, analogous to that  
920 proposed for chondrules by Chaussidon *et al.* (2008).

921

## 922 **Implications for Protoplanetary Disk Environments and Evolution**

923 The extreme O-isotopic heterogeneity recorded by CAIs and their WL rims is consistent  
924 with exposure to nebular gases with different O-isotopic compositions. CAIs that formed in the  
925 inner solar system may have initially had relatively  $^{16}\text{O}$ -rich “protosolar” compositions.  
926 Thermodynamic calculations show that, as the protoplanetary disk cooled, the refractory phases  
927 characteristic of CAIs would not have survived had they continued to equilibrate with the gas  
928 down to low temperatures (Grossman *et al.*, 2002; 2008). Analyses of refractory cometary  
929 samples show that the solar nebula experienced a phase of large-scale outward transport of

930 refractory grains (Brownlee *et al.*, 2006) and that these grains are relatively  $^{16}\text{O}$ -rich, similar to  
931 the  $\Delta^{17}\text{O} \sim -20 \pm 3\%$  compositions of “normal” bulk CAIs (McKeegan *et al.*, 2006; Krot *et al.*,  
932 2010; Bullock *et al.*, 2012) and a possible “intermediate” oxygen isotopic reservoir envisioned  
933 herein. Likewise, there are a number of ways refractory inclusions could have been removed  
934 from the inner solar nebula. One way is by large-scale transport and mixing processes associated  
935 with a marginally gravitationally unstable disk, a likely cause of FU Orionis events in young  
936 low-mass stars, e.g., Boss *et al.* (2012). Protostellar jets and disk winds, commonly associated  
937 with star formation, have also been suggested (Shu *et al.*, 1996). These hot winds may have  
938 played a role in heating and redistributing material out to distances of several AU (Salmeron and  
939 Ireland, 2012). Alternatively, CAIs may have formed near ( $<1$  AU) the protoSun and been  
940 subsequently transported outward ( $>10$  AU) due to the viscous evolution of the disk and  
941 turbulence effects within it (Cuzzi *et al.*, 2003; Ciesla, 2007). After transport processes such as  
942 these brought CAIs into the outer solar system, they could have encountered relatively  $^{17,18}\text{O}$ -rich  
943 environments such as may have been created, for example, by concentration of relatively  $^{17,18}\text{O}$ -  
944 rich water near the snow line (Young, 2007).

945         The various CAI transport mechanisms discussed here are associated with astrophysical  
946 processes having characteristic timescales and heating times that are quite different from one  
947 another. Accordingly, O-isotopic profiles established by exchange during these different events  
948 should record different diffusion times. For example, the rapid FU outbursts occur very early,  
949 within  $<10$  years of the beginning of the solar system (Boss *et al.*, 2012) and heating times in  
950 disk winds are relatively short,  $\leq 30$  years (Shu *et al.*, 2001). Outward transport of CAIs from the  
951 inner to the outer nebular disk by diffusive processes takes much longer,  $10^3$ - $10^4$  years (Cuzzi *et*  
952 *al.*, 2003), and appears better matched to the timescales required to reproduce the O-isotopic  
953 profiles observed in Type A CAI interiors. The absolute time period may have been longer than  
954 the time required for diffusive exchange since diffusion calculations in this study only represent  
955 the integrated time at elevated temperatures and not necessarily the total time over which CAIs  
956 migrated within the protoplanetary disk (Fig. 9, Table 4). Likewise, the diffusive exchange could  
957 reflect hundreds or thousands of short heating events and/or maybe related to WL rim formation  
958 (e.g., Young *et al.*, 2005), expected for particle transport by disk winds or within the shock fronts  
959 of density waves within the disk. It is also possible that radial excursions of CAIs across the  
960 inner edge of the disk gas produced both the mineralogical layering and O-isotopic variation of  
961 WL rims, due to the confluence of relatively  $^{16}\text{O}$ -poor disk and  $^{16}\text{O}$ -rich gas reservoirs (Park *et*  
962 *al.* 2012) and non-solar gas reservoirs that developed because of infall of outer disk material onto  
963 the protoSun through radial evaporation fronts (e.g., the snow line). Further work coordinating  
964 O-isotope profiles with high precision Al-Mg chronology and measurements of more refractory

965 stable isotopes (e.g., Mg and perhaps Ca) could help distinguish the roles of condensation,  
966 diffusive growth, and accumulation of preexisting dust grains as they relate to the astrophysical  
967 environments of WL rim formation and the alteration of CAI interiors in the nebula.

968

### 969 **A General History of and Summary of Features of Coarse-grained CAIs Based on Their** 970 **Oxygen Isotope Compositions**

971

972 The studied inclusions imply the following formation history:

973 (1) Spinel data from A37 attest to the fact that some, and possibly all, CAIs initially formed from  
974 the protosolar oxygen isotopic composition ( $\Delta^{17}\text{O} \sim -28\%$ , McKeegan *et al.*, 2010).

975 (2) The uniform intermediate composition ( $\Delta^{17}\text{O} \sim -17\text{-}23\%$ ) of the interior melilite of A37 and  
976 spinel and fassaite in the interior of Type B CAI TS4 implies that some CAIs were exposed  
977 to a nebular gas of intermediate oxygen isotopic composition for up to  $2 \times 10^4$  years, assuming  
978 oxygen exchange occurred at temperatures of 1400 K. This might reflect the reservoir that is  
979 typically considered “normal” for CAIs.

980 (3) The relatively  $^{16}\text{O}$ -poor melilite interiors of all studied Type A CAIs indicate many CAIs  
981 were exposed to an  $^{16}\text{O}$ -poor reservoir for as long as  $5 \times 10^3$  to  $3 \times 10^4$  years, assuming  
982 temperatures of 1400 K. In total, a period of nearly  $3.6 \times 10^4$  years is needed for the two  
983 exchange steps indicated by the oxygen record of A37, assuming temperatures of 1400 K.  
984 Two steps of exchange are also indicated by the Type B CAI TS4 data and could require a  
985 similar timescale, but it would be significantly shorter if equilibration with the intermediate  
986 reservoir in the first step occurred while the inclusion was still partially molten.

987 (4) The  $^{16}\text{O}$ -poor interior of Type B CAI Egg-6 either reflects protracted exchange on the  
988 chondrite parent body or exchange with a planetary-like nebular gas in the solid-state, similar  
989 to that inferred for the Type A CAIs. If exchange occurred in the nebula, it would have  
990 required  $\sim 3 \times 10^5$  years at 1400 K. Alternatively, if the isotopic compositions of the melilite in  
991 the interiors of the studied Type B CAIs reflect parent body processes, then much longer  
992 timescales ( $> 10^6$  years) are required even considering hydrothermal oxygen diffusion rates.  
993 The source of the required protracted heating remains elusive in either case, cf. Rubin (1995).

994 (5) The strong gradients in A37 and L6 towards planetary-like and relatively  $^{16}\text{O}$ -rich  
995 compositions, respectively, likely occurred in a second step of nebular solid-state exchange  
996 (in #3). The protosolar environments documented by observations #1-5 may all predate rim  
997 formation, similar to the inclusions described in Yoshitake *et al.* (2005) and Aleon *et al.*  
998 (2007). A37 appears to record modification of the outermost melilite edge by a heating event

- 999 (e.g., Wark and Boynton, 2001) that involved a relatively  $^{16}\text{O}$ -poor, planetary-like reservoir,  
1000 described as the earliest rim-forming event by J. Simon *et al.* (2011).
- 1001 (6) Preservation of the strong gradients in A37 and L6 suggest circumstances where diffusive  
1002 isotopic equilibration was limited and may indicate that these inclusions were rimmed  
1003 relatively early and/or that they were rapidly accreted onto a parent body reducing the  
1004 formation of dislocations from subsequent ionizing radiation.
- 1005 (7) The relatively  $^{16}\text{O}$ -enriched melilite margins of all studied Type A CAIs (except A37) indicate  
1006 exposure to a relatively  $^{16}\text{O}$ -rich nebular gas. It is possible that the strong gradients in A37  
1007 and L6, and the more subtle ones in Ef-1 and ALH3, actually reflect the effect of rim-  
1008 forming processes.
- 1009 (8) The spinel±hibonite layer surrounding all studied CAIs reflects formation from a relatively  
1010  $^{16}\text{O}$ -rich gas. Some spinel at the base of WL-rims may predate rim formation (Wark and  
1011 Lovering, 1982). It remains unclear whether the spinel±hibonite layer involves partial  
1012 melting of the interior (Wark and Boynton, 2001) or whether it originates from the gas phase  
1013 alone.
- 1014 (9) Pyroxene layers outside the spinel±hibonite layer can be heterogeneous in  $\Delta^{17}\text{O}$ , from  
1015 relatively  $^{16}\text{O}$ -rich to planetary-like, and they often record outward (“reverse”) zoning  
1016 towards more  $^{16}\text{O}$ -rich compositions. This heterogeneity and sense of zoning is inconsistent  
1017 with metasomatic growth in the nebula or on a parent body. It is likely that typical portions of  
1018 WL rims condensed from several gas reservoirs with isotopically distinct compositions.
- 1019 (10) The heterogeneous O-isotopic compositions in the olivine rim layers and in accretionary  
1020 rims suggest that both types of olivine grew from relatively  $^{16}\text{O}$ -rich and  $^{16}\text{O}$ -poor gases  
1021 (Krot *et al.*, 2002).
- 1022 (11) Finally, replacement of primary minerals by secondary minerals may have occurred in the  
1023 nebula, e.g., Hutcheon and Newton (1981), and certainly occurred on the parent body.  
1024 Distinguishing between these two end-member environments for given occurrences requires  
1025 coordinated petrologic and isotopic studies.

## 1026 1027 CONCLUSIONS 1028

1029 The evolution of coarse-grained CAIs included open-system diffusive exchange with  
1030 multiple, relatively  $^{16}\text{O}$ -poor and  $^{16}\text{O}$ -rich nebular gases, followed by Wark-Lovering rim  
1031 formation, also from relatively  $^{16}\text{O}$ -poor and  $^{16}\text{O}$ -rich nebular gases, through condensation and  
1032 possibly by the accumulation of preexisting nebular solids. The “normal” and “reverse” isotopic  
1033 zoning profiles observed across the margins of refractory inclusions require that most CAIs

1034 contained in CV3 chondrites experienced at least a two-step nebular exchange history. Larger  
1035 shifts towards planetary-like O-isotope compositions in the melilite contained in Ef-1 and L6,  
1036 both from reduced and more pristine chondrites, than in A37, an oxidized CV3 chondrite,  
1037 indicate that oxygen exchange is decoupled from the formation of secondary alteration products.  
1038 The  $\Delta^{17}\text{O}$  record observed in WL rims is complicated, often exhibiting evidence of “reverse” O-  
1039 isotopic zoning, and shifting from rather homogenous to extremely heterogeneous over short  
1040 distances within and among mineral layering. Considered together with their changing mineral  
1041 chemistry and textures, their  $\Delta^{17}\text{O}$  values suggest that the rims grew under disequilibrium  
1042 conditions in a dynamic, rather hot nebular environment. The complex WL rim on L6, composed  
1043 of five distinct pyroxene layers and probably three distinct melilite zones with varying O-  
1044 isotopic composition, demonstrates that some of the mineral layers formed sequentially, in  
1045 discrete growth events. All of these observations support numerical disk models in which CAIs  
1046 were transported between distinct nebular reservoirs multiple times over  $\sim 10^3$ - $10^5$  years prior to  
1047 accretion onto a parent body. The relatively common occurrence of CAI phases with  $\Delta^{17}\text{O} \approx -$   
1048 20‰ may indicate the existence of an early, intermediate reservoir in which some inclusions re-  
1049 equilibrated before, and in some cases after, initial WL rim growth.

1050

## 1051 **Acknowledgments**

1052 Dr. Ian Douglass Hutcheon (1947-2015) was an exceptional scientist, mentor, and friend.  
1053 He made significant contributions to this work masterfully integrating intuition, open-  
1054 mindedness, and skepticism. His co-authors and many others in our community will sorely miss  
1055 him. We are grateful to Journal Editor D. Papanastassiou and three anonymous reviewers for  
1056 their careful and constructive reviews of this paper. The work was supported by NASA  
1057 Cosmochemistry and Origins Programs: grants 11-COS11-0066 to JIS, NNH10AO48I and  
1058 NNH10AO05I to IDH, and NNX13AE73G to LG. Repolishing of several ‘well-used’ samples  
1059 by Roger Harrington is gratefully appreciated. This work was performed under the auspices of  
1060 the U.S. Department of Energy at Lawrence Livermore National Laboratory under Contract DE-  
1061 AC52-07NA27344.

1062

## 1063 **References**

1064

- 1065 Aleon, J., El Goresy, A., Zinner, E., 2007. Oxygen isotope heterogeneities in the earliest  
1066 protosolar gas recorded in a meteoritic calcium-aluminum-rich inclusion. *Earth and Planetary*  
1067 *Science Letters* 263, 114-127.
- 1068 Amelin, Y., Krot, A.N., Hutcheon, I.D. and Ulyanov, A.A., 2002. Lead isotopic ages of  
1069 chondrules and calcium-aluminum-rich inclusions. *Science* 297, 1678-1683.

1070 Barber, D.J., Martin, P.M., Hutcheon, I.D., 1984. The microstructure of minerals in coarse-  
1071 grained Ca-Al-rich inclusions from the Allende meteorite. *Geochimica et Cosmochimica*  
1072 *Acta* 48, 769-783.

1073 Bodéan, J.-D., Starkey, N.A., Russell, S.S., Wright, I.P., Franchi, I.A., 2014. An oxygen isotope  
1074 study of Wark-Lovering rims on type A CAIs in primitive carbonaceous chondrites. *Earth*  
1075 *and Planetary Science Letters* 401, 327-336.

1076 Bonal, L., Quirico, E., Bourot-Denise, M., Montagnac, G., 2006. Determination of the petrologic  
1077 type of CV3 chondrites by Raman spectroscopy of included organic matter. *Geochimica et*  
1078 *Cosmochimica Acta* 70, 1849-1863.

1079 Boss, A.P., 2004. Evolution of the solar nebula. VI. Mixing and transport of isotopic  
1080 heterogeneity. *Astrophysical Journal* 616, 1265-1277.

1081 Boss, A.P., Alexander, C.M.O.D., Podolak, M., 2012. Cosmochemical consequences of particle  
1082 trajectories during FU Orionis outburst by the early Sun. *Earth and Planetary Science Letters*  
1083 345-348, 18-26.

1084 Bouvier, A. and Wadhwa, M., 2010. The age of the Solar System redefined by the oldest Pb-Pb  
1085 age of a meteoritic inclusion. *Nature GeoScience* 3, 637-641.

1086 Boynton, W.V., Wark, D.A., 1985. Refractory rims: Evidence for high temperature events in the  
1087 post-formation history of Ca,Al-rich inclusions. *Meteoritics* 20, 613-614.

1088 Brearley, A., 1997. Disordered Biopyriboles, Amphibole, and Talc in the Allende Meteorite:  
1089 Products of Nebular or Parent Body Aqueous Alteration. *Science* 276, 1103-1105.

1090 Brearley, A.J., Jones, R.H., 1998. Chondritic Meteorites, in: Papike, J.J. (Ed.), *Planetary*  
1091 *Materials*. Mineralogical Society of America, Washington, D.C., pp. 1-398.

1092 Brownlee, D., Tsou, P., Aleon, J., Alexander, C.M.O., Araki, T., Bajt, S., Baratta, G.A., Bastien,  
1093 R., Bland, P., Bleuet, P., Borg, J., Bradley, J.P., Brearley, A., Brenker, F., Brennan, S.,  
1094 Bridges, J.C., Browning, N.D., Brucato, J.R., Bullock, E., Burchell, M.J., Busemann, H.,  
1095 Butterworth, A., Chaussidon, M., Chevront, A., Chi, M.F., Cintala, M.J., Clark, B.C.,  
1096 Clemett, S.J., Cody, G., Colangeli, L., Cooper, G., Cordier, P., Daghlian, C., Dai, Z.R.,  
1097 D'Hendecourt, L., Djouadi, Z., Dominguez, G., Duxbury, T., Dworkin, J.P., Ebel, D.S.,  
1098 Economou, T.E., Fakra, S., Fairey, S.A.J., Fallon, S., Ferrini, G., Ferroir, T., Fleckenstein,  
1099 H., Floss, C., Flynn, G., Franchi, I.A., Fries, M., Gainsforth, Z., Gallien, J.P., Genge, M.,  
1100 Gilles, M.K., Gillet, P., Gilmour, J., Glavin, D.P., Gounelle, M., Grady, M.M., Graham,  
1101 G.A., Grant, P.G., Green, S.F., Grossemy, F., Grossman, L., Grossman, J.N., Guan, Y.,  
1102 Hagiya, K., Harvey, R., Heck, P., Herzog, G.F., Hoppe, P., Horz, F., Huth, J., Hutcheon, I.D.,  
1103 Ignatyev, K., Ishii, H., Ito, M., Jacob, D., Jacobsen, C., Jacobsen, S., Jones, S., Joswiak, D.,  
1104 Jurewicz, A., Kearsley, A.T., Keller, L.P., Khodja, H., Kilcoyne, A.L.D., Kissel, J., Krot, A.,  
1105 Langenhorst, F., Lanzirotti, A., Le, L., Leshin, L.A., Leitner, J., Lemelle, L., Leroux, H., Liu,  
1106 M.C., Luening, K., Lyon, I., MacPherson, G., Marcus, M.A., Marhas, K., Marty, B., Matrajt,  
1107 G., McKeegan, K., Meibom, A., Mennella, V., Messenger, K., Messenger, S., Mikouchi, T.,  
1108 Mostefaoui, S., Nakamura, T., Nakano, T., Newville, M., Nittler, L.R., Ohnishi, I., Ohsumi,  
1109 K., Okudaira, K., Papanastassiou, D.A., Palma, R., Palumbo, M.E., Pepin, R.O., Perkins, D.,  
1110 Perronnet, M., Pianetta, P., Rao, W., Rietmeijer, F.J.M., Robert, F., Rost, D., Rotundi, A.,  
1111 Ryan, R., Sandford, S.A., Schwandt, C.S., See, T.H., Schlutter, D., Sheffield-Parker, J.,  
1112 Simionovici, A., Simon, S., Sitnitsky, I., Snead, C.J., Spencer, M.K., Stadermann, F.J.,  
1113 Steele, A., Stephan, T., Stroud, R., Susini, J., Sutton, S.R., Suzuki, Y., Taheri, M., Taylor, S.,  
1114 Teslich, N., Tomeoka, K., Tomioka, N., Toppani, A., Trigo-Rodriguez, J.M., Troadec, D.,  
1115 Tsuchiyama, A., Tuzzolino, A.J., Tylliszczak, T., Uesugi, K., Velbel, M., Vellenga, J.,  
1116 Vicenzi, E., Vincze, L., Warren, J., Weber, I., Weisberg, M., Westphal, A.J., Wirick, S.,  
1117 Wooden, D., Wopenka, B., Wozniakiewicz, P., Wright, I., Yabuta, H., Yano, H., Young,  
1118 E.D., Zare, R.N., Zega, T., Ziegler, K., Zimmerman, L., Zinner, E., Zolensky, M., 2006.  
1119 Research article - Comet 81P/Wild 2 under a microscope. *Science* 314, 1711-1716.

1120 Bullock, E.S., Knight, K.B., Richter, F.M., Kita, N.T., Ushikubo, T., MacPherson, G.J., Davis,  
1121 A.M., Mendybaev, R.A., 2013. Mg and Si isotopic fractionation patterns in types B1 and B2

1122 CAIs: Implications for formation under different nebular conditions. *Meteoritics and*  
1123 *Planetary Sciences* 48, 1440-1458.

1124 Bullock, E.S., MacPherson, G.J., Nagashima, K., Krot, A.N., Petaev, M.I., Jacobsen, S.B. and  
1125 Ulyanov, A.A., 2012. Forsterite-bearing type B refractory inclusions from CV3 chondrites:  
1126 aggregates to volatilized melt droplets. *Meteoritics and Planetary Sciences* 47, 2128-2147.

1127 Chaussidon, M., Libourel, G., Krot, A.N., 2008. Oxygen isotopic constraints on the origin of  
1128 magnesian chondrules and on the gaseous reservoirs in the early Solar System. *Geochimica*  
1129 *et Cosmochimica Acta* 72, 1924-1938.

1130 Ciesla, F.J., 2007. Outward transport of high-temperature materials around the midplane of the  
1131 solar nebula. *Science* 318, 613-615.

1132 Clarke Jr., R.S., E. Jarosewich, B. Mason, J. Nelen, M. Gomez, J.R. Hyde, 1970. The Allende,  
1133 Mexico meteorite shower. *Smithsonian Contrib. Earth Sciences*, 5 (1970), pp. 1-53.

1134 Clayton, R.N., 2002. Solar System - Self-shielding in the solar nebula. *Nature* 415, 860-861.

1135 Clayton, R.N., Onuma, N., Grossman, L., Mayeda, T.K., 1977. Distribution of the pre-solar  
1136 component in Allende and other carbonaceous chondrites. *Earth and Planetary Science*  
1137 *Letters* 34, 209-224.

1138 Connelly, J.N., Bizzarro, M., Krot, A.N., Nordlund, A., Wielandt, D. and Ivanova, M.A., 2012.  
1139 The Absolute Chronology and Thermal Processing of Solids in the Solar Protoplanetary  
1140 Disk. *Science* 338, 651-655.

1141 Cosarinsky, M., Leshin, L.A., MacPherson, G.J., Guan, Y., Krot, A.N., 2008. Chemical and  
1142 oxygen isotopic compositions of accretionary rim and matrix olivine in CV chondrites:  
1143 Constraints on the evolution of nebular dust. *Geochimica et Cosmochimica Acta* 72, 1887-  
1144 1913.

1145 Cosarinsky, M., Taylor, D.J., McKeegan, K.D., Hutcheon, I.D., 2005. Mg isotopic study of  
1146 Wark-Lovering rims in Type A inclusions from CV chondrites: formation mechanisms and  
1147 timing, 68th Annual Meteoritical Society Meeting, p. Abst. #5284.

1148 Crank, J., 1975. *The Mathematics of Diffusion*, 2<sup>nd</sup> Edition, Clarendon Press, Oxford, eqn. 6.18,  
1149 p. 91.

1150 Cuzzi, J.N., Davis, S.S., Dobrovolskis, A.R., 2003. Blowing in the wind. II. Creation and  
1151 redistribution of refractory inclusions in a turbulent protoplanetary nebula. *Icarus* 166, 385-  
1152 402.

1153 Desch, S.J., Connolly, H.C.J., 2002. A model of the thermal processing of particles in solar  
1154 nebula shocks: Application to the cooling rates of chondrules. *Meteoritics and Planetary*  
1155 *Sciences* 37, 183-207.

1156 Dominguez, G., 2010. A heterogeneous chemical origin for the <sup>16</sup>O-enriched and <sup>16</sup>O-depleted  
1157 reservoirs of the early solar system. *The Astrophysical Journal Letters* 713, L59-L63.

1158 Dyl, K.A., Simon, J.I., Young, E.D., 2011. Valence state of titanium in the Wark-Lovering rim  
1159 of a Leoville CAI as a record of progressive oxidation in the early Solar Nebula. *Geochimica*  
1160 *et Cosmochimica Acta* 75, 937-949.

1161 Fagan, T.J., Krot, A., Keil, K., Yurimoto, H., 2004a. Oxygen isotope alteration in Ca-Al-rich  
1162 inclusions from Efremovka: Nebular or parent body setting? *Meteoritics and Planetary*  
1163 *Sciences* 39, 1257-1272.

1164 Fagan, T.J., Krot, A.N., Keil, K., Yurimoto, H., 2004b. Oxygen isotopic evolution of amoeboid  
1165 olivine aggregates in the reduced CV3 chondrites Efremovka, Vigarano, and Leoville.  
1166 *Geochimica et Cosmochimica Acta* 68, 2591-2611.

1167 Fahey, A.J., Goswami, J.N., McKeegan, K.D., Zinner, E., 1987a. Al-26, Pu-244, Ti-50, REE,  
1168 and Trace-Element Abundances in Hibonite Grains from CM and CV Meteorites.  
1169 *Geochimica et Cosmochimica Acta* 51, 329-350.

1170 Fahey, A.J., Zinner, E.Z., Crozaz, G., Kornacki, A.S., 1987b. Microdistributions of Mg isotopes  
1171 and REE abundances in a Type A calcium-aluminum-rich inclusion from Efremovka.  
1172 *Geochimica et Cosmochimica Acta* 51, 3215-3229.

1173 Fedkin, A.V., Grossman, L., 2006. The Fayalite Content of Chondritic Olivine: Obstacle to  
1174 Understanding the Condensation of Rocky Material, in: Lauretta, D., McSween, H.Y.J.  
1175 (Eds.), *Meteorites and the Early Solar System II*. University of Arizona Press, Tucson, AZ,  
1176 pp. 279-294.

1177 Grossman, L., 1972. Condensation in the primitive solar nebula. *Geochimica et Cosmochimica*  
1178 *Acta* 36, 597-619.

1179 Grossman, L., Ebel, D.S., Simon, S.B., 2002. Formation of refractory inclusions by evaporation  
1180 of condensate precursors. *Geochimica et Cosmochimica Acta* 66, 145-161.

1181 Grossman, L., Simon, S.B., Rai, V.K., Thiemens, M.H., Hutcheon, I.D., Williams, R.W., Galy,  
1182 A., Ding, T., Fedkin, A.V., Clayton, R.N., Mayeda, T.K., 2008. Primordial compositions of  
1183 refractory inclusions. *Geochimica et Cosmochimica Acta* 72, 3001-3021.

1184 Han, J., Brearley, A.J., 2012. The microstructure and microchemistry of amoeboid olivine  
1185 aggregates from the ALHA 77307 CO3.0 carbonaceous chondrite: Constraints on formation  
1186 and thermal histories, 43rd Lunar and Planetary Science Conference, Abstr. #1323.

1187 Hsu, W.B., Wasserburg, G.J., Huss, G.R., 2000. High time resolution by use of the Al-26  
1188 chronometer in the multistage formation of a CAI. *Earth and Planetary Science Letters* 182,  
1189 15-29.

1190 Huss, G.R., Meshik, A.P., Smith, J.B., Hohenberg, C.M., 2003. Presolar diamond, silicon  
1191 carbide, and graphite in carbonaceous chondrites: Implications for thermal processing in the  
1192 solar nebula. *Geochimica et Cosmochimica Acta* 67, 4823-4848.

1193 Huss, G.R., Rubin, A.E., Grossman, J.N., 2006. Thermal Metamorphsim in Chondrites, in:  
1194 Lauretta, D.S., McSween, H.Y. (Eds.), *Meteorities and the Early Solar System II*. University  
1195 of Arizona Press, pp. 567-586.

1196 Hutcheon, I.D., Krot, A.N., Keil, K., Phinney, D.L., Scott, E.R.D., 1998. <sup>53</sup>Mn-<sup>53</sup>Cr Dating of  
1197 Fayalite Formation in the CV3 Chondrite Mokoia: Evidence for Asteroidal Alteration.  
1198 *Science* 282, 1865-1867.

1199 Hutcheon, I.D. and Newton, R.C., 1981. Mg isotopes, mineralogy, and mode of formation of  
1200 secondary phases in C3 refractory inclusions, 12th Lunar and planetary Science Conference  
1201 pp. 491-493.

1202 Ingrin, J., Picaud, L., Jaoul, O., 2001. Anisotropy of oxygen diffusion in diopside. *Earth and*  
1203 *Planetary Science Letters* 192, 347-361.

1204 Ito, M., Messenger, S., Keller, L.P., Rahman, Z.U., Ross, D.K., Nakamura-Messenger, K., 2010.  
1205 FIB-NanoSIMS-TEM coordinated study of a Wark-Lovering rim in a Vigarano Type A CAI,  
1206 41st Lunar and Planetary Science Conference Abst. 1177.

1207 Keller, L.P., Buseck, P.R., 1991. Calcic micas in the Allende meteorite: Evidence for hydration  
1208 reactions in the early Solar nebula. *Science* 252, 947-949.

1209 Keller, L.P., Needham, A.W., Messenger, S., 2013. A FIB/TEM study of a complex Wark-  
1210 Lovering rim on a Vigarano CAI, Meteoritical Society, Abst #5300, Edmonton.

1211 Keil, K., Stoffer, D., Love, S.G., Scott, E.R.D., 1997. Constrains on the role of impact heating  
1212 and melting in asteroids. *Meteoritics and Planetary Sciences* 32, 349-363.

1213 Krot, A.N., Nagashima, K., Ciesla, F.J., Meyer, B.S., Hutcheon, I.D., Davis, A.M., Huss, G.R.  
1214 and Scott, E.R.D., 2010. Oxygen isotopic composition of the Sun and mean oxygen isotopic  
1215 composition of protosolar silicate dust: evidence from refractory inclusions. *The*  
1216 *Astrophysical Journal* 713, 1159-1166.

1217 Krot, A.N., McKeegan, K.D., Leshin, L.A., MacPherson, G.J., Scott, E.R.D., 2002. Existence of  
1218 an <sup>16</sup>O-Rich Gaseous Reservoir in the Solar Nebula. *Science* 295, 1051-1054.

1219 Kunihiro, T., Rubin, A.E., McKeegan, K.D., Wasson, J.T., 2004. Initial <sup>26</sup>Al/<sup>27</sup>Al in  
1220 carbonaceous-chondrite chondrules: Too little <sup>26</sup>Al to melt asteroids. *Geochimica et*  
1221 *Cosmochimica Acta* 68, 2947-2957.

1222 Kwok, S., Purton, C.R., FitzGerald, P.M., 1978. On the origin of planetary nebulae\*. *The*  
1223 *Astrophysical Journal* 219, L125-L127.

1224 LaTourrette, T., Hutcheon, I.D., 1999. Mg Diffusion in Melilite: Thermal Histories for CAIs and  
1225 their Parent Bodies, Lunar and Planetary Science Conference XXX, Abst #2003.

1226 Liang, Y., Richter, F.M., Davis, A.M., Watson, E.B., 1996. Diffusion in silicate melts 1. Self  
1227 diffusion in CaO-Al<sub>2</sub>O<sub>3</sub>-SiO<sub>2</sub> at 1500 degrees C and 1 GPa. *Geochimica et Cosmochimica*  
1228 *Acta* 60, 4353-4367.

1229 Lyons, J.R., Young, E.D., 2005. CO self-shielding as the origin of oxygen isotope anomalies in  
1230 the early solar nebula. *Nature* 435, 317-320.

1231 MacPherson, G.J., Kita, N.T., Ushikubo, T., Bullock, E.S. and Davis, A.M., 2012. Well-resolved  
1232 variations in the formation ages for Ca-Al-rich inclusions in the early Solar System. *Earth*  
1233 *and Planetary Science Letters* 331-332, 43-45.

1234 MacPherson, G.J., Davis, A.M., 1993. A Petrologic and Ion Microprobe Study of a Vigarano  
1235 Type-B Refractory Inclusion - Evolution by Multiple Stages of Alteration and Melting.  
1236 *Geochimica et Cosmochimica Acta* 57, 231-243.

1237 MacPherson, G.J., Hashimoto, A., Grossman, L., 1985. Accretionary rims on inclusions in the  
1238 Allende meteorite. *Geochimica et Cosmochimica Acta* 49, 2267-2279.

1239 MacPherson, G.J., Grossman, L., 1981. A once-molten, coarse-grained, Ca-rich inclusion in  
1240 Allende. *Earth and Planetary Science Letters* 52, 16-24.

1241 MacPherson, G.J., Grossman, L., Allen, J.M., Beckett, J.R., 1981. Origin of rims on coarse-  
1242 grained inclusions in the Allende meteorite. *Proceedings of Lunar Science Conference* 12th,  
1243 1079-1091.

1244 Mahon, K.I., 1996. The New "York" Regression: Application of an Improved Statistical Method  
1245 to Geochemistry. *International Geology Review* 38, 293-303.

1246 Matzel, J.E.P., Simon, J.I., Hutcheon, I.D., Jacobsen, B., Simon, S.B., Grossman, L., 2013.  
1247 Oxygen isotope measurements of a rare Murchison Type A CAI and its rim, 44th Lunar and  
1248 Planetary Science Conference, p. Abst. #2632.

1249 McKeegan, K.D., Aleon, J., Bradley, J., Brownlee, D. and Stardust Team, 2006. Isotopic  
1250 Compositions of Cometary Matter Returned by Stardust. *Science* 314, 1724-1728.

1251 McKeegan, K.D., Kallio, A.P.A., Heber, V.S., Jarzebinski, G., Mao, P.H., Coath, C.D.,  
1252 Kunihiro, T., Wien, R.C., Nordhort, J.E., Moses Jr., R.W., Reisenfeld, D.B., Jurewicz,  
1253 A.J.G., Burnett, D.S., 2011. The oxygen isotopic composition of the Sun inferred from  
1254 captured solar wind. *Science* 332, 1528-1532.

1255 Meeker, G.P., Wasserburg, G.J., Armstrong, J.T., 1983. Replacement textures in CAI and  
1256 implications regarding planetary metamorphism. *Geochimica et Cosmochimica Acta* 47,  
1257 707-721.

1258 Metzler, K., Bischoff, A., Stöfler, D., 1992. Accretionary dust mantles in CM chondrites:  
1259 Evidence for solar nebula processes. *Geochimica et Cosmochimica Acta* 56, 2873-2897.

1260 Murrell, M.T., Burnett, D.S., 1986. Actinide chemistry in Allende Ca-Al-rich inclusions.  
1261 *Geochimica et Cosmochimica Acta* 51, 985-999.

1262 Park, C., Wakaki, S., Sakamoto, N., Kobayashi, S., Yurimoto, H., 2012. Oxygen isotopic  
1263 composition of the solar nebula gas inferred from high-precision isotope image of melilite  
1264 crystals in an Allende CAI. *Meteoritics & Planetary Science* 47, 2070-2083.

1265 Pouchou, J.L., Pichoir, F., 1984. A new model for quantitative X-ray microanalysis. Part I:  
1266 Application to the analysis of homogeneous samples. *Rech. Aerosp.* 3, 13-38.

1267 Rubin, A.E., 1995. Petrologic Evidence for Collisional Heating of Chondritic Asteroids. *Icarus*  
1268 113, 156-167.

1269 Ruzicka, A., 1997. Mineral layers around coarse-grained, Ca-Al-rich inclusions in CV3  
1270 carbonaceous chondrites: formation by high-temperature metasomatism. *Journal of*  
1271 *Geophysical Research* 102, 13,387-313,402.

1272 Ryerson, F.J., McKeegan, K.D., 1994. Determination of Oxygen Self-Diffusion in Akermanite,  
1273 Anorthite, Diopside, and Spinel - Implications for Oxygen Isotopic Anomalies and the  
1274 Thermal Histories of Ca-Al-Rich Inclusions. *Geochimica et Cosmochimica Acta* 58, 3713-  
1275 3734.

1276 Sakamoto, N., Seto, Y., Itoh, S., Kuramoto, K., Fujino, K., Nagashima, K., Krot, A.N.,  
1277 Yurimoto, H., 2007. Remnants of the Early Solar System Water Enriched in Heavy Oxygen  
1278 Isotopes. *Science* 317, 231-233.

1279 Salmeron, R., Ireland, T., 2012. The role of protostellar jets in star formation and the evolution  
1280 of the early solar system: Astrophysical and meteoritical perspectives. *Meteoritics &*  
1281 *Planetary Science* 47, 1922-1940.

1282 Scott, E.R.D., Love, S.G., Krot, A., 1996. Formation of chondrules and chondrites in the  
1283 protoplanetary nebula, in: Hewin, R.H., Jones, R.H., Scott, E.R.D. (Eds.), *Chondrules and the*  
1284 *Protoplanetary Disk*. Cambridge University Press, pp. 87-96.

1285 Shu, F.H., Shang, H., Gounelle, M., Glassgold, A.E., Lee, T., 2001. The origin of chondrules and  
1286 refractory inclusions in chondritic meteorites. *Astrophysical Journal* 548, 1029-1050.

1287 Shu, F.H., Shang, H., Lee, T., 1996. Toward an astrophysical theory of chondrites. *Science* 271,  
1288 1545-1552.

1289 Simon, J.I., DePaolo, D.J., 2010. Stable calcium isotopic composition of meteorites and rocky  
1290 planets. *Earth and Planetary Science Letters* 289, 457-466.

1291 Simon, J.I., Hutcheon, I.D., Simon, S.B., Matzel, J.E.P., Ramon, E.C., Weber, P.K., Grossman,  
1292 L., DePaolo, D.J., 2011. Oxygen Isotope Variations at the Margin of a CAI Records  
1293 Circulation Within the Solar Nebula. *Science* 331, 1175-1178.

1294 Simon, J.I., Young, E.D., 2011. Resetting, errorchrons and the meaning of canonical CAI initial  
1295  $^{26}\text{Al}/^{27}\text{Al}$  values. *Earth and Planetary Science Letters* 304, 468-482.

1296 Simon, J.I., Young, E.D., Russell, S.S., Tonui, E.K., Dyl, K.A., Manning, C.E., 2005. A short  
1297 timescale for changing oxygen fugacity in the solar nebula revealed by high-resolution Al-  
1298 26-Mg-26 dating of CAI rims. *Earth and Planetary Science Letters* 238, 272-283.

1299 Simon, S.B., Davis, A.M., Grossman, L., 1999. Origin of compact type A refractory inclusions  
1300 from CV3 carbonaceous chondrites. *Geochimica et Cosmochimica Acta* 63, 1233-1248.

1301 Simon, S.B., Davis, A.M., Grossman, L., 2001. Formation of orange hibonite, as inferred from  
1302 some Allende inclusions. *Meteoritics and Planetary Sciences* 36, 331-350.

1303 Simon, S.B., Grossman, L., 2013. A compact type A inclusion with multiple Wark-Lovering  
1304 rims: a complex history recorded in pyroxene, 44th Lunar and Planetary Science Conference.  
1305 Lunar and Planetary Institute, Houston, p. Abs#2793.

1306 Stolper, E., 1982. Crystallization sequences of Ca-Al-rich inclusions from Allende: An  
1307 experimental study. *Geochimica et Cosmochimica Acta* 46, 2159-2180.

1308 Wark, D.A., Boynton, W.V., 2001. The formation of rims on calcium-aluminum-rich inclusions:  
1309 step I--flash heating. *Meteoritics and Planetary Sciences* 36, 1135-1166.

1310 Wark, D.A., Lovering, J.F., 1977. Marker events in the early evolution of the solar system:  
1311 Evidence from rims on Ca-Al-rich inclusions in carbonaceous chondrites. *Proceedings of*  
1312 *Lunar Science Conference* 8th, 95-112.

1313 Wark, D.A., Lovering, J.F., 1982. Evolution of Ca-, Al-rich bodies in the earliest solar system:  
1314 growth by incorporation. *Geochimica et Cosmochimica Acta* 46, 2595-2607.

1315 Wasserburg, G.J., Typhoon, L., Papanastassiou, D.A., 1977. Correlated O and Mg isotopic  
1316 anomalies in Allende inclusions: II. Manganese. *Geophysical Research Letters* 4, 299-302.

1317 Wasson, J.T., Yurimoto, H., Russell, S.S., 2001.  $^{16}\text{O}$ -rich melilite in CO3.0 chondrites: possible  
1318 formation of common,  $^{16}\text{O}$ -poor melilite by aqueous alteration. *Geochimica et*  
1319 *Cosmochimica Acta* 65, 4539-4549.

1320 Yoshitake, M., Koide, Y., Yurimoto, H., 2005. Correlations between oxygen-isotopic  
1321 composition and petrologic setting in a coarse-grained Ca, Al-rich inclusion. *Geochimica et*  
1322 *Cosmochimica Acta* 69, 2663-2674.

1323 Young, E.D., 2001. The hydrology of carbonaceous chondrite parent bodies and the evolution of  
1324 planet progenitors. *The Royal Society* 359, 2095-2110.

1325 Young, E.D., 2007. Time-dependent oxygen isotopic effects of CO self shielding across the solar  
1326 protoplanetary disk. *Earth and Planetary Science Letters* 2007, 468-483.

- 1327 Young, E.D., Simon, J.I., Galy, A., Russell, S.S., Tonui, E., Lovera, O., 2005. Supra-canonical  
1328 Al-26/Al-27 and the residence time of CAls in the solar protoplanetary disk. *Science* 308,  
1329 223-227.
- 1330 Yurimoto, H., Kuramoto, K., 2004. Molecular cloud origin for the oxygen isotope heterogeneity  
1331 in the solar system. *Science* 305, 1763-1766.
- 1332 Yurimoto, H., Ito, M., Nagahara, H., 1998. Oxygen isotope exchange between refractory  
1333 inclusion in Allende and Solar Nebula Gas. *Science* 282, 1874-1876.
- 1334 Yurimoto, H., Morioka, M., Nagasawa, H., 1989. Diffusion in single crystals of melilite: I  
1335 Oxygen. *Geochimica et Cosmochimica Acta* 53, 2387-2394.
- 1336

### 1337 **Figure captions**

1338

1339 Figure 1. Si<sup>2+</sup>/<sup>16</sup>O<sup>2-</sup> ion ratios from Leoville L6, showing that this ratio can be used to distinguish  
1340 mixtures of two or more phases from pure phases. Inset shows systematic shifts in the Si<sup>2+</sup>/<sup>16</sup>O<sup>2-</sup>  
1341 ion ratio at the outer margin of the inclusion related to melilite chemical composition zoning.  
1342 Filled symbols are pure phases: spinel (red), melilite (tan), Ti-pyroxene (light blue), diopside  
1343 (black); mixtures shown by x's. Symbols of the same color, but different shape (i.e., circle,  
1344 square, and diamond) indicate the same mineral phase analyzed in different NanoSIMS transects.

1345

1346 Figure 2. Images of compact Type A inclusion Ef-1. (A) Low-magnification, false-color X-ray  
1347 map (Mg=red, Ca=green, Al=blue), showing occurrence of spinel (purple), pyroxene (dark green  
1348 and olive green), and melilite (blue-green) in the interior of the inclusion and the WL rim.  
1349 Olivine is red and epoxy is black. Region of interest indicated by the white dashed-line rectangle.  
1350 (B) Backscattered electron image overlain upon a secondary electron image, showing the  
1351 locations of NanoSIMS traverses (T-1, T-2; black rectangles) and electron microprobe transect  
1352 (EMP; blue circles) in the WL rim and margin. Some measurements are located further towards  
1353 the center of the inclusion, beyond the field of view. Mel: melilite; Sp: spinel; Ti-pyx: Ti-bearing  
1354 pyroxene; mtx: matrix. Size of analysis spots enhanced by 2x for clarity.

1355

1356 Figure 3. Images of compact Type A inclusion L6. (A) Backscattered electron image of section,  
1357 showing sparse spinel in the melilite-rich interior, spinel-rich WL rim, and meteorite matrix.  
1358 Locations of NanoSIMS traverses (T-1 to T-4) and the area shown in B. (red dashed-line region)  
1359 are indicated. Epoxy is black. (B) False-color X-ray map (Mg=red, Ca=green, Al=blue), showing  
1360 occurrence of spinel (purple) and pyroxene (dark green and olive green) and melilite (blue-  
1361 green) at the rim and olivine (red) in the matrix. Locations of electron microprobe analytical  
1362 traverses (yellow lines) and areas shown in C. and D. (white dashed-line rectangles) are  
1363 indicated. (C) Backscattered electron image of the location of Traverse 4 (T-4), which sampled  
1364 the outer granular melilite and spinel unit Mel-3 and pyroxene units Ti-pyx-4 and Al-pyx-5, the  
1365 latter being the outermost, continuous diopside layer. (D) Backscattered electron image of the  
1366 location of Traverse 3 (T-3), which sampled melilite, spinel, and pyroxene unit Ti-pyx-1 (black  
1367 rectangles). Abbreviations as used previously, plus Per: perovskite. Size of NanoSIMS analysis  
1368 spots enhanced by 50% for clarity.

1369

1370 Figure 4. Images of compact Type A inclusion A37. (A) False colored X-ray map (Mg=red,  
1371 Ca=green, Al=blue) of entire section, showing varying concentrations of spinel in the melilite-  
1372 rich interior. WL rim section and area shown in B. are indicated. (B) Aluminum (Al K $\alpha$ ) X-ray  
1373 map of region with NanoSIMS traverses (T1 to T4) and electron microprobe (EMP) transects of  
1374 J. Simon *et al.* (2011) are indicated. Melilite composition zoning (increasing Al content) at the  
1375 edge of the inclusion and within individual melilite grains can be discerned. Area shown in C. is  
1376 indicated by red-shaded rectangle. (C) Backscattered electron image of WL rim layers from  
1377 inside out include melilite (Mel Åk); hibonite (Hib)  $\pm$ perovskite (Per); melilite (Mel)  $\pm$ nepheline  
1378 (Neph); pyroxene (pyx) zoned from Ti-rich to Al-rich; and olivine (Ol). Area shown in D. is

1379 indicated by dashed-line rectangle at bottom. (D) Backscattered electron image of melilite-on-  
1380 melilite WL rim-interior interface, indicated by red arrows.

1381  
1382 Figure 5. Backscattered electron images of Type A inclusion ALH3. (A) View of entire section  
1383 showing WL rim and locations (white dashed-line rectangles) of areas shown in B. and C. (B)  
1384 Locations of NanoSIMS traverses 1 and 2 (T-1 and T-2). (C) Locations of NanoSIMS traverses 3  
1385 and 4 (T-3 and T-4). Abbreviations as used previously, plus Adr: andradite; Grs: grossular. Size  
1386 of NanoSIMS analysis spots enhanced by 50% for clarity.

1387  
1388 Figure 6. Images of Type B1 inclusion Egg-6. (A) Low-magnification, false-color X-ray map  
1389 (Mg=red, Ca=green, Al=blue) of entire section, showing spinel (purple), fassaite (coarse, dark  
1390 green grains), melilite (light green) and anorthite (blue) in the interior of the inclusion, and  
1391 grossular veins (dark green) across the mantle. Olivine is red and epoxy is black. Interior  
1392 NanoSIMS analysis locations are indicated by black rectangles and traverses, T-1 and T-2 (white  
1393 dashed-lines). Areas shown in B.-F. are indicated by dashed-line rectangles where the main WL  
1394 rim traverse and additional WL rim analyses were made. (B) False-color X-ray map of rim  
1395 region that includes the area shown in C. (colors and phases as in A.). (C) Backscattered electron  
1396 image (BEI) of the location of the main WL rim NanoSIMS traverse that sampled spinel and Ti-  
1397 pyroxene rim layers. (D) BEI of locations of NanoSIMS analyses measured at the end of T-2. (E)  
1398 BEI showing locations of NanoSIMS spots in melilite, spinel and diopside in the WL rim. (F)  
1399 BEI showing locations of NanoSIMS spots in spinel. Abbreviations as used previously. Size of  
1400 NanoSIMS analysis spots enhanced by 50% for clarity.

1401  
1402 Figure 7. Images of Type B2 inclusion TS4. (A) Low-magnification, false-color X-ray map  
1403 (Mg=red, Ca=green, Al=blue) of entire section, showing spinel (purple), fassaite (dark green),  
1404 melilite (light green) and anorthite (blue). Olivine is red, epoxy is black, and secondary pyroxene  
1405 within, but mostly defining the outer edge of the accretionary rim, is forest green. Two  
1406 NanoSIMS traverses, T-1 and T-2, are indicated by the white dashed-lines. (B) BEI showing the  
1407 NanoSIMS Traverse 1, from the interior (left) to the rim (right) of the inclusion. Individual rim  
1408 layers are outlined in red dashed-lines. (C) BEI showing the NanoSIMS Traverse 2, from the  
1409 interior (right) to the rim (left) of the inclusion. Abbreviations as used previously, plus Sod:  
1410 sodalite. Size of NanoSIMS analysis spots enhanced by 50% for clarity.

1411  
1412 Figure 8. Melilite compositions (mole % åkermanite), determined by electron microprobe, as a  
1413 function of distance from the edge of the inclusion interior (i.e., the contact between the  
1414 inclusion and WL rim) in four of the inclusions in the present study. (A) Compact Type A  
1415 inclusion Ef-1. A slight increase in Åk content is seen at the rim. (B) Compact Type A inclusion  
1416 L6. This sample has multiple rim units, as indicated; distances are measured from the innermost  
1417 rim inward (positive values) or outward (negative values). Circles and diamonds represent  
1418 analyses of interior and rim melilite, respectively. The different symbol shades represent  
1419 different EMP traverses. (C) Compact Type A inclusion A37. Data from J. Simon *et al.* (2011).  
1420 (D) Type B2 inclusion TS4. Squares represent analyses of interior melilite, circles are data from  
1421 traverses across the margin. The different symbol shades represent different EMP traverses.

1422  
1423 Figure 9. Oxygen isotopic zoning profiles across the margins of (A) Allende A37, (B) Allende  
1424 Egg-6, (C), Allende TS4, (D) Leoville L6, (E) Allende ALH3, and (F) Efremovka Ef-1. Primary  
1425 minerals are color-coded: melilite-tan, spinel-purple, fassaite-blue, perovskite-light green,  
1426 anorthite-dark green and olivine-red. For the primary phases different symbol shapes or borders  
1427 indicate different traverses. All secondary minerals are gray: plagioclase (triangles), and sodalite  
1428 (diamonds). Also shown are modeled diffusion profiles, discussed in text and summarized in  
1429 Table 4. For consistency, all models shown reflect calculations for diffusive exchange of oxygen  
1430 at 1400 K between interior solid melilite and a nebular gas reservoir, assumed to have  $P^{\text{tot}} = 10^{-3}$

1431 bar. Blue band labeled “protosolar gas” is the solar gas composition of McKeegan *et al.* (2011).  
1432 The red curve in (A) is representative of the mismatch of single-step models for A37. The black  
1433 curves in (A) reflect the cumulative effects of two-steps of oxygen exchange, the first that reset  
1434 melilite to an intermediate  $\Delta^{17}\text{O}$  value (step 1), implied by the relatively uniform value measured  
1435 in the interior, before melilite at its margin exchanged further with a near-zero  $\Delta^{17}\text{O}$  planetary  
1436 reservoir (step 2). In (B) single-step models (black curves) can be matched to the data, assuming  
1437 the inclusion initially had a protosolar  $\Delta^{17}\text{O}$  composition and then experienced oxygen exchange  
1438 that transformed its  $\Delta^{17}\text{O}$  to those of the interior melilite. In (C), interior spinel and fassaite have  
1439 similar  $\Delta^{17}\text{O}$  values of  $-22\pm 2\%$ , whereas melilite is relatively  $^{16}\text{O}$ -poor and exhibits constant to  
1440 slightly increasing  $\Delta^{17}\text{O}$  towards the edge of the inclusion. Model curves reflect two-steps of  
1441 exchange, where first the inclusion equilibrates with a reservoir of intermediate  $\Delta^{17}\text{O}$   
1442 composition, recorded by the similarity of its spinel and fassaite (step 1), before melilite  
1443 exchanged further as in (A) (step 2). For (D, E, and F), the reversely zoned CAIs, the model  
1444 curves were calculated as above, except that the interior melilite values were used for the initial  
1445 CAI value and the nebular gas reservoir was assumed to have the same  $\Delta^{17}\text{O}$  as the spinel in the  
1446 WL rims (see Table 4).

1447  
1448 Figure 10. Oxygen isotopic variability among Wark-Lovering rim layers surrounding (A)  
1449 Allende A37, (B) Allende Egg-6, (C) Allende TS4, (D) Leoville L6, (E) Allende ALH3, and (F)  
1450 Efremovka Ef-1. Solid and dashed vertical lines indicate contacts between rims and interiors,  
1451 and between individual WL rim layers, respectively. Layers are further identified by phase  
1452 labels along the tops of the plots. Numbers in (D) are L6 pyroxene layer units. Diagonal dashed  
1453 lines connect pyroxene analyses that exhibit “reverse” isotopic zoning within a single analytical  
1454 transect. Color-coding and solid curves as in Fig. 9, plus diopside (black circles), accretionary  
1455 olivine (red X’s), secondary nepheline (grey circles in (A)) and andradite (grey square in (E)).  
1456

**Table 1**

Spot	Mineral	From Edge of Inclusion ( $\mu\text{m}$ )	$\delta^{18}\text{O}/^{16}\text{O}^*$	$2\sigma$ (%) <sup>*</sup>	$\delta^{17}\text{O}/^{16}\text{O}^*$	$2\sigma$ (%) <sup>*</sup>	$\Delta^{17}\text{O}^*$	$2\sigma$ (%) <sup>*</sup>	$\Delta^{17}\text{O}^{**}$	$2\sigma$ (%) <sup>**</sup>	$^{28}\text{Si}/^{16}\text{O}$
<b>Interior follow up (August 2011)</b>											
A37_sp_2	spinel	660	-37.2	2.4	-48.6	4.3	-29.2	4.5	-29.4	5.8	5.5E-06
A37_sp_3	spinel	660	-34.2	2.4	-46.1	4.4	-28.4	4.5	-28.5	5.8	8.7E-07
A37_mel_1	melilite	661	-11.3	1.9	-21.9	3.9	-16.0	4.1	-17.5	5.2	9.9E-04
A37_mel_2	melilite	661	-12.7	2.0	-21.6	3.9	-14.9	4.1	-16.5	5.2	9.4E-04
A37_sp_1	spinel	825	-39.3	2.5	-51.5	5.5	-31.1	5.7	-31.2	6.8	5.5E-06

\* Standard mineral-specific instrumental corrections applied to measurements (i.e., olivine, anorthite, or spinel). Uncertainties include propagation of measured  $2\sigma$  counting statistics and  $2\sigma$  systematic errors of the mean for each mineral standard. These data are plotted in Figures 9 and 10.

\*\* Average standard mineral instrumental corrections applied to measurements. Uncertainties reflect the propagation of measured  $2\sigma$  counting statistics and  $2\sigma$  scatter about the mean derived from all mineral standard measurements.

Table 1. Egg-6 Oxygen isotope data

Spot	Mineral	From Edge of Inclusion (µm)	$\delta^{18}\text{O}^{16}\text{O}^*$	$2\sigma$ (%)**	$\delta^{17}\text{O}^{16}\text{O}^*$	$2\sigma$ (%)**	$\Delta^{17}\text{O}^*$	$2\sigma$ (%)**	$\Delta^{17}\text{O}^{**}$	$2\sigma$ (%)**	$^{28}\text{Si}^{16}\text{O}$
Traverse 1 (August 2011)											
Egg6_1	spinel (Fe)	-38	-40.7	2.2	-45.0	3.8	-23.8	3.9	-23.9	5.5	
Egg6_2	perovskite	-24	-14.2	1.9	-17.8	3.0	-10.4	3.2	-10.5	5.0	
Egg6_3	spinel	-11	-35.8	2.4	-37.8	3.5	-19.2	3.7	-19.3	5.4	
Egg6_4	plagioclase	2	0.9	1.9	-0.8	3.8	-1.3	3.9	-2.8	5.6	
Egg6_5	plagioclase	15	6.5	1.9	5.8	3.8	2.4	4.0	0.9	5.6	
Egg6_6	plagioclase	28	8.3	1.9	4.5	3.9	0.2	4.0	-1.4	5.6	
Egg6_7	melilite	41	3.6	1.9	0.3	3.8	-1.6	3.9	-3.1	5.6	
Egg6_8	melilite	54	3.3	1.9	1.0	4.2	-0.7	4.3	-2.2	5.9	
Egg6_9	melilite	67	4.0	1.7	2.1	3.8	0.0	3.9	-1.5	5.6	
Egg6_10	melilite	80	5.1	1.8	1.3	3.6	-1.4	3.8	-2.9	5.5	
Egg6_0	melilite	113	3.4	2.0	2.6	4.2	0.8	4.3	-0.7	5.9	
Egg6_1_1	melilite	145	6.8	1.8	1.4	4.0	-2.2	4.2	-3.7	5.7	
Egg6_1b	melilite	165	1.1	2.0	-2.6	4.1	-3.2	4.2	-4.7	5.8	
Egg6_1_2	spinel	179	-34.8	2.2	-40.4	3.9	-22.3	4.1	-22.4	5.6	
Egg6_2b	melilite	192	4.3	1.6	3.0	3.9	0.7	4.0	-0.8	5.6	
Egg6_1_3	melilite	212	8.7	1.9	2.3	3.8	-2.2	4.0	-3.8	5.6	
Egg6_1_4	melilite	244	3.9	1.8	2.9	3.7	0.9	3.8	-0.6	5.5	
Egg6_1_5	melilite	277	2.7	1.9	0.2	3.9	-1.2	4.1	-2.7	5.7	
Egg6_1_6	melilite	310	-1.8	2.1	-4.0	4.5	-3.1	4.7	-4.6	6.1	
Egg6_1_7	melilite	342	7.2	1.9	5.5	3.8	1.7	4.0	0.2	5.6	
Egg6_7b	vein grossular	355	8.5	2.0	3.1	3.7	-1.3	3.8	-2.8	5.5	
Egg6_8b	vein grossular	395	6.3	1.9	1.3	3.7	-1.9	3.8	-3.5	5.5	
Egg6_1_9	melilite	410	6.9	2.0	2.0	3.8	-1.6	4.0	-3.1	5.6	
Egg6_1_10	melilite	442	7.4	1.9	4.3	3.6	0.5	3.7	-1.0	5.4	
Egg6_1_11	melilite	475	4.9	2.0	3.4	4.1	0.8	4.2	-0.7	5.8	
Egg6_1_12	melilite	508	6.5	1.9	3.1	4.0	-0.3	4.2	-1.9	5.8	
Traverse 2 (August 2011)											
Egg6_t2_1_1	spinel	-25	-42.4	2.5	-43.9	4.4	-21.8	4.6	-21.9	6.0	
Egg6_t2_1_2	spinel	-10	-41.2	2.4	-50.9	4.6	-29.4	4.8	-29.5	6.2	
Egg6_t2_1_4	melilite	19	0.5	2.1	-0.2	3.9	-0.5	4.0	-2.0	5.6	
Egg6_t2_1_5	melilite	34	1.6	2.0	-3.0	4.5	-3.9	4.6	-5.4	6.1	
Egg6_t2_1_6	melilite	48	0.3	2.2	-0.9	4.5	-1.0	4.7	-2.5	6.1	
Egg6_t2_1_7	melilite	63	-0.9	2.1	-2.5	4.2	-2.1	4.4	-3.6	5.9	
Egg6_t2_1_8	vein grossular	78	4.1	2.2	-6.0	4.6	-8.1	4.7	-9.6	6.2	
Egg6_t2_1_9	vein grossular	93	2.1	2.1	-6.7	4.1	-7.8	4.2	-9.3	5.8	
Egg6_t2_1_10	melilite	107	-0.7	2.0	-2.3	4.2	-1.9	4.3	-3.4	5.9	
Egg6_t2b_1_1	melilite	146	-13.2	2.2	-7.8	4.1	-1.0	4.3	-2.5	5.8	
Egg6_t2b_1_2	melilite	184	0.5	2.0	-4.9	4.2	-5.2	4.4	-6.7	5.9	
Egg6_t2b_1_3	vein grossular	222	6.5	2.2	2.1	4.5	-1.3	4.6	-2.9	6.1	
Egg6_t2b_1_4	vein grossular	260	4.1	2.0	-1.3	4.1	-3.4	4.3	-4.9	5.8	
Egg6_t2b_1_5	melilite	298	3.8	2.0	-1.6	4.0	-3.6	4.1	-5.1	5.7	
Egg6_t2b_1_6	fassait	337	-34.0	1.8	-36.7	3.7	-18.9	3.8	-18.1	5.5	
Egg6_t2b_1_7	melilite	375	5.4	2.0	-3.5	4.3	-6.3	4.4	-7.8	5.9	
Egg6_t2b_1_8	melilite	413	5.9	1.9	-1.3	4.1	-4.4	4.2	-5.9	5.8	
Egg6_t2b_1_10	melilite	489	4.2	1.9	-2.1	4.2	-4.2	4.3	-5.8	5.9	
Egg6_t2b_1_11	melilite	528	5.2	2.0	-2.0	4.3	-4.7	4.4	-6.2	5.9	
Egg6_t2b_1_12	melilite	566	-0.2	1.8	-7.8	3.8	-7.7	3.9	-9.2	5.6	
Egg6_t2b_1_13	melilite	604	4.0	2.0	-3.1	3.8	-5.2	3.9	-6.7	5.6	
Egg6_t2b_1_14	melilite	642	3.3	2.0	-3.4	4.0	-5.2	4.1	-6.7	5.7	
Egg6_t2b_1_15	melilite	681	4.4	1.8	-4.8	4.2	-7.0	4.3	-8.6	5.8	
Main WL-rim Traverse (December 2012)											
Egg6_spn_1	spinel (Fe)	-41	-51.1	1.3	-49.6	3.0	-23.0	3.1	-23.7	5.1	1.08E-05
Egg6_spn_2	spinel (Fe)	-33	-44.4	1.6	-42.2	3.3	-19.1	3.4	-19.8	5.3	8.69E-04
Egg6_spn_3	Ti-pyroxene + spinel	-26	-11.6	2.1	-14.5	3.9	-8.5	4.0	-9.2	5.5	1.67E-02
Egg6_perov_3	spinel > perovskite	-18	-20.7	1.2	-23.5	2.3	-12.7	2.4	-13.4	4.7	2.22E-04
Egg6_spn_4	Ti-pyroxene	-17	-8.3	1.9	-8.4	3.6	-4.1	5.3	-4.9	4.9	2.05E-02
Egg6_spn_5	Ti-pyroxene	-11	-8.0	1.9	-6.2	3.5	-2.0	5.3	-2.8	2.29E-02	
Egg6_perov_1	spinel + perovskite	-9	-1.1	0.9	-4.2	2.1	-3.7	2.1	-4.4	4.6	5.78E-05
Egg6_spn_6	spinel	0	-39.5	1.8	-40.5	3.7	-19.9	3.8	-20.6	5.5	2.84E-04
Near main WL-rim Traverse (December 2012)											
Egg6_perov_5	perovskite	-23	1.8	1.0	-1.7	2.1	-2.6	2.2	-3.3	4.6	4.19E-05
Egg6_perov_4	perovskite	-17	-0.2	1.0	-1.3	2.0	-1.2	2.0	-1.9	4.5	4.68E-05
Egg6_perov_2	perovskite > spinel?	-9	3.5	1.2	-2.3	2.3	-4.2	2.4	-4.9	4.7	1.78E-02
Rim Traverse Follow up (March 2013)											
Egg6_rim_1	Al-pyroxene	-47	1.6	1.6	-3.2	3.5	-4.0	3.6	-4.3	5.3	3.30E-02
Rim Traverse-1 (March 2013)											
Egg6_spn_t1_1	spinel	-21	-49.3	1.7	-52.3	3.4	-26.6	3.4	-26.9	4.9	1.96E-05
Egg6_spn_t1_3	spinel	-21	-43.4	1.7	-48.0	3.4	-25.3	3.4	-25.6	5.0	1.96E-05
Rim Traverse-2 (February-March 2013)											
Egg6_spn_t2_4	Al-pyroxene	-52	-17.2	1.8	-22.4	3.9	-13.4	4.0	-13.7	5.6	3.85E-02
Egg6_spn_t2_1	spinel	-22	-45.4	1.6	-50.6	3.2	-26.9	3.2	-27.2	4.8	1.37E-04
Egg6_spn_t2_2	spinel + melilite	-13	11.7	1.9	-0.6	4.0	-6.7	4.0	-7.0	5.4	2.41E-02
Egg6_spn_t2_3	melilite	-2	2.9	1.7	-3.8	3.8	-5.2	3.8	-4.3	5.3	2.09E-02
Isolated Rim Analyses (February 2013)											
Egg6_spn_t3_2	spinel	-27	-41.5	2.0	-44.8	4.2	-23.1	4.2	-23.4	5.5	6.45E-04
Egg6_spn_t3_3	spinel	-21	-43.1	2.0	-48.6	4.2	-26.1	4.2	-26.4	5.5	1.45E-04
Interior (December 2012)											
Egg6_fass1	vein grossular	interior	0.2	1.8	-0.7	3.3	-0.8	3.4	0.5	5.1	3.09E-02
Egg6_fass2	fassait	interior	-45.5	1.8	-43.2	2.9	-19.5	3.1	-20.2	4.9	3.19E-02
Egg6_fass3_1	vein grossular	interior	5.9	1.8	1.2	3.5	-1.9	3.6	-0.6	5.2	2.58E-02
Representative Analyses in Melilite margin (February 2013)											
Egg6_spn_mantle_4	spinel	60	-42.1	1.8	-47.6	3.7	-25.7	3.7	-26.0	5.2	7.93E-06
Egg6_spn_mantle_2	spinel	144	-39.2	1.8	-45.3	3.7	-24.9	3.7	-25.2	5.2	6.21E-06
Egg6_spn_mantle_3	spinel	175	-43.0	1.9	-50.6	3.9	-28.2	3.9	-28.5	5.3	4.11E-06
Egg6_spn_mantle_1	spinel	467	-41.5	1.8	-48.9	3.7	-27.2	3.7	-27.5	5.2	6.69E-06
Egg6_fs_mantle_1	fassait	1056	-29.6	1.6	-32.3	3.4	-16.9	3.5	-17.2	5.3	3.66E-02
Egg6_fs_mantle_2	fassait	1432	-33.1	1.7	-34.8	3.8	-17.5	3.8	-17.8	5.5	2.94E-02
Representative Analyses in Core (February-March 2013)											
Egg6_spn_core_4	spinel	2065	-42.0	1.9	-47.2	4.0	-25.3	4.0	-25.6	5.4	1.38E-08
Egg6_spn_core_3	spinel	2452	-43.7	2.0	-44.8	4.1	-22.0	4.1	-22.3	5.4	1.13E-08
Egg6_spn_core_2	spinel	2733	-45.0	1.8	-48.6	3.6	-25.2	3.6	-25.5	5.1	2.79E-08
Egg6_an_core_1	anorthite	3026	2.9	1.6	-2.8	3.5	-4.3	3.5	-3.3	5.1	3.15E-02
Egg6_an_core_2	anorthite	3167	-3.7	1.8	-13.1	3.9	-11.2	3.9	-10.2	5.4	2.84E-02
Egg6_spn_core_1	spinel	3202	-39.8	1.9	-42.6	3.9	-21.9	4.0	-22.2	5.3	8.47E-06

\* Standard mineral-specific instrumental corrections applied to measurements (i.e., olivine, anorthite, or spinel). Uncertainties include propagation of measured  $2\sigma$  counting statistics and  $2\sigma$  systematic errors of the mean for each mineral standard. These data are plotted in Figures 9 and 10.

\*\* Average standard mineral instrumental corrections applied to measurements. Uncertainties reflect the propagation of measured  $2\sigma$  counting statistics and  $2\sigma$  scatter about the mean derived from all mineral standard measurements.

Table 1. TS4 Oxygen Isotope Data

Spot	Mineral	From Edge of Inclusion ( $\mu\text{m}$ )	$\delta^{18}\text{O}/^{16}\text{O}^*$	$2\sigma$ (‰)*	$\delta^{17}\text{O}/^{16}\text{O}^*$	$2\sigma$ (‰)*	$\Delta^{17}\text{O}^*$	$2\sigma$ (‰)*	$\Delta^{17}\text{O}^{**}$	$2\sigma$ (‰)**	$^{28}\text{Si}/^{16}\text{O}$
Traverse-1 (August 2011)											
TS4_WL_3	olivine	-77	-6.3	1.5	-3.4	3.3	-0.2	3.4	0.7	5.0	8.97E-04
TS4_WL_4	olivine	-71	-7.8	1.3	-5.2	2.4	-1.1	2.5	-0.2	4.5	8.79E-04
TS4_WL_5	olivine	-67	-13.0	1.6	-11.9	3.1	-5.1	3.2	-4.2	4.8	6.66E-04
TS4_WL_6	olivine	-60	-36.1	1.4	-40.0	3.0	-21.3	3.1	-20.4	4.8	8.18E-04
TS4_WL_7	olivine	-53	-15.8	1.4	-19.9	3.0	-11.7	3.1	-10.8	4.8	8.41E-04
TS4_WL_8	olivine	-46	-32.2	1.4	-35.9	3.0	-19.2	3.1	-18.2	4.8	8.83E-04
TS4_WL_9	olivine	-39	-6.0	1.6	-9.9	3.0	-6.8	3.2	-5.9	4.8	9.92E-04
TS4_WL_10	Al-pyroxene + < spinel	-33	0.8	1.5	-5.4	3.0	-5.8	3.1	-4.9	4.8	8.66E-04
TS4_interior_16	spinel	0	-28.5	1.9	-34.8	2.8	-19.9	3.0	-20.1	4.8	8.27E-05
TS4_interior_17	sodalite	7	12.1	1.8	8.6	3.4	2.3	3.5	0.8	4.8	7.14E-04
TS4_interior_18	sodalite	14	8.5	1.7	2.3	3.2	-2.1	3.3	-3.6	4.6	7.49E-04
TS4_interior_19	sodalite	20	8.9	1.7	3.1	3.4	-1.5	3.6	-3.0	4.8	6.11E-04
TS4_interior_20	melilite	34	12.3	1.7	5.9	3.4	-0.5	3.5	-2.0	4.7	8.08E-04
TS4_interior_21	melilite	43	13.1	1.7	7.5	3.3	0.7	3.4	-0.8	4.7	9.11E-04
TS4_interior_23	spinel + fassaite	109	-30.7	2.0	-39.9	3.1	-23.9	3.3	-24.0	4.9	1.83E-04
TS4_interior_24	fassaite + < spinel	143	-36.2	1.7	-41.3	3.2	-22.5	3.3	-21.6	4.9	9.64E-04
TS4_interior_25	fassaite + spinel	189	-39.2	1.5	-45.4	3.1	-25.0	3.2	-24.1	4.9	7.63E-04
TS4_interior_26	fassaite	226	-30.0	1.5	-34.8	3.0	-19.2	3.1	-18.3	4.8	9.96E-04
TS4_interior_27	melilite	349	8.7	1.5	4.0	3.0	-0.6	3.1	-2.1	4.4	9.86E-04
Traverse-2 (August 2011)											
TS4_mel_55	olivine	-80	-13.1	1.3	-7.0	2.4	-0.2	2.5	0.7	4.4	1.67E-03
TS4_mel_52	melilite	35	14.9	1.9	7.4	3.3	-0.4	3.4	-1.9	4.7	1.01E-03
TS4_mel_51	melilite	44	13.8	1.7	6.1	3.1	-1.0	3.2	-2.5	4.5	1.07E-03
TS4_mel_50	melilite	54	14.4	1.8	5.1	3.0	-2.4	3.1	-3.9	4.5	1.06E-03
TS4_mel_49	melilite	64	7.8	1.5	2.3	2.9	-1.7	3.0	-3.2	4.3	8.70E-04
TS4_mel_48	melilite	75	9.3	1.5	2.5	3.0	-2.4	3.1	-3.9	4.4	8.51E-04
TS4_mel_47	melilite	85	-12.9	1.6	-7.6	3.3	-0.9	3.4	-2.5	4.7	1.18E-03
TS4_mel_45	spinel	105	-43.0	2.0	-43.8	3.0	-21.4	3.2	-21.5	4.9	3.11E-05
TS4_mel_44	melilite	115	12.8	1.8	7.5	3.1	0.9	3.3	-0.6	4.6	9.69E-04
TS4_mel_43	melilite	125	12.7	1.5	5.2	2.7	-1.4	2.8	-2.9	4.3	1.02E-03
TS4_mel_42	melilite	136	-0.4	1.7	0.4	3.3	0.6	3.4	-0.9	4.7	1.03E-03
TS4_mel_41	melilite	144	12.8	1.9	6.4	3.1	-0.3	3.3	-1.8	4.6	9.81E-04
TS4_mel_40	melilite	153	9.6	1.6	5.1	3.4	0.1	3.5	-1.4	4.7	1.05E-03
TS4_mel_39	melilite	164	13.0	1.6	5.2	3.0	-1.5	3.1	-3.1	4.4	1.10E-03
TS4_mel_38	spinel	174	-40.3	2.0	-41.8	3.1	-20.8	3.2	-20.9	4.9	4.17E-04
TS4_mel_37	fassaite	185	-32.8	1.5	-38.3	3.1	-21.3	3.2	-20.4	4.9	9.60E-04
TS4_mel_36	fassaite	194	-31.7	1.4	-38.6	2.8	-22.1	2.9	-21.2	4.7	1.03E-03
TS4_mel_35	fassaite + < spinel	218	-43.8	1.6	-44.7	3.2	-21.9	3.3	-21.0	4.9	7.18E-06
TS4_mel_34	melilite (some alteration)	246	15.9	1.9	11.2	3.1	2.9	3.2	1.4	4.5	1.16E-03
TS4_mel_32	anorthite (some alteration)	318	12.2	1.8	6.1	3.6	-0.2	3.8	-1.7	4.9	7.91E-04
TS4_mel_31	spinel	467	-32.0	2.2	-38.0	3.2	-21.4	3.4	-21.5	5.0	7.16E-06
TS4_mel_30	melilite	614	7.9	1.6	-0.8	3.2	-4.9	3.3	-6.4	4.6	1.04E-03
TS4_mel_29	spinel	769	-33.3	1.9	-40.9	3.1	-23.6	3.3	-23.7	4.9	7.29E-06
TS4_mel_28	anorthite	896	-8.8	1.6	-15.0	3.2	-10.5	3.3	-12.0	4.6	8.27E-04
Assorted interior spots (August 2011)											
TS4_lgfass_1	fassaite	880	-33.7	1.6	-41.6	3.0	-24.1	3.1	-25.5	4.8	1.05E-03
TS4_lgfass_2	fassaite	880	-33.1	1.6	-38.4	3.3	-21.2	3.4	-22.6	5.0	1.05E-03
TS4_lgfass_3	fassaite	880	-35.5	1.6	-40.0	3.3	-21.6	3.5	-22.9	5.0	1.03E-03
TS4_pal_fs_1	fassaite	960	-33.6	1.7	-40.2	3.3	-22.7	3.4	-24.1	5.0	1.05E-03
TS4_pal_fs_2	fassaite	965	-34.9	1.6	-39.3	3.5	-21.2	3.6	-22.6	5.1	1.12E-03
TS4_pal_fs_3	fassaite	970	-33.2	1.7	-40.1	3.2	-22.8	3.3	-24.2	4.9	1.06E-03
TS4_pal_an_1	anorthite	910	0.7	1.8	-7.0	3.9	-7.4	4.0	-8.8	5.1	8.21E-04
TS4_pal_an_2	anorthite	915	1.7	2.0	-7.4	3.9	-8.3	4.0	-9.7	5.1	8.30E-04
TS4_pal_an_3	anorthite	920	2.3	1.8	-1.4	3.7	-2.6	3.8	-4.0	5.0	8.49E-04
TS4_pal_mel_1	melilite	930	6.5	1.8	-1.4	3.6	-4.8	3.7	-6.1	4.9	8.47E-04
TS4_pal_mel_2	melilite	935	4.0	1.7	-1.8	3.6	-3.8	3.7	-5.2	4.9	1.06E-03
TS4_pal_sp_1	spinel	940	-32.3	2.2	-38.2	3.7	-21.4	3.9	-21.8	5.3	6.97E-06
TS4_pal_sp_2	spinel	945	-29.4	2.1	-41.6	3.8	-26.3	3.9	-26.7	5.4	1.07E-04
TS4_pal_sp_3	spinel	950	-36.7	2.2	-41.4	3.7	-22.3	3.9	-22.8	5.4	1.05E-05
Internal Inclusion (August 2011)											
TS4_dark_1	pyroxene		11.9	1.7	1.5	3.6	-4.7	3.7	-3.8	5.2	1.19E-03
TS4_bright_1	pyroxene (Fe)		14.8	1.6	6.4	3.3	-1.3	3.4	-0.4	5.0	1.04E-03
TS4_olint_1	olivine		-3.0	1.8	-6.2	3.4	-4.6	3.5	-3.7	5.1	9.53E-04
TS4_olrim_1	olivine		9.8	1.6	4.3	3.2	-0.8	3.3	0.1	4.9	1.36E-03
TS4_sp_1	spinel		-35.2	2.0	-41.9	3.5	-23.6	3.7	-24.0	5.2	6.77E-06
TS4_sp_2	spinel		-31.0	2.1	-40.6	3.4	-24.5	3.6	-24.9	5.2	5.32E-06
TS4_mel_3	spinel + melilite		-27.9	2.1	-37.9	3.3	-23.4	3.5	-23.8	5.1	1.68E-04
TS4_mel_4	unknown Fe-Mg silicate		-8.6	2.7	-5.7	5.0	-1.3	5.2	-0.4	6.4	1.35E-03
TS4_ol_2	olivine		-4.2	1.7	-9.8	3.8	-7.6	3.9	-6.7	5.4	9.45E-04
TS4_ol_3	olivine		-4.8	1.7	-11.8	3.9	-9.3	4.0	-8.3	5.4	1.01E-03

\* Standard mineral-specific instrumental corrections applied to measurements (i.e., olivine, anorthite, or spinel). Uncertainties include propagation of measured  $2\sigma$  counting statistics and  $2\sigma$  systematic errors of the mean for each mineral standard. These data are plotted in Figures 9 and 10.

\*\* Average standard mineral instrumental corrections applied to measurements. Uncertainties reflect the propagation of measured  $2\sigma$  counting statistics and  $2\sigma$  scatter about the mean derived from all mineral standard measurements.

Table 1. L6 Oxygen Isotope Data

Spot	Mineral	From Edge of Inclusion ( $\mu\text{m}$ )	$\delta^{18}\text{O}/^{16}\text{O}^*$	$2\sigma$ (‰)*	$\delta^{17}\text{O}/^{16}\text{O}^*$	$2\sigma$ (‰)*	$\Delta^{17}\text{O}^*$	$2\sigma$ (‰)*	$\Delta^{17}\text{O}^{**}$	$2\sigma$ (‰)**	$^{28}\text{Si}/^{16}\text{O}$
Traverse 2 (March 2013)											
L6_t2@1_1	melilite + < spinel	-47.4	-21.3	1.7	-23.2	4.3	-12.0	4.4	-11.0	5.8	1.90E-02
L6_t2@1_2	spinel	-3.6	-42.4	2.0	-46.7	4.1	-24.6	4.2	-24.9	5.5	1.41E-04
L6_t2@1_4	melilite + < spinel	26.6	7.2	1.9	-1.1	3.9	-4.8	4.0	-3.8	5.5	2.19E-02
L6_t2@1_5	melilite	41.1	3.3	2.0	-3.7	4.3	-5.5	4.4	-4.4	5.8	2.05E-02
L6_t2@1_6	melilite	57.0	7.6	1.7	-1.8	3.8	-5.8	3.9	-4.7	5.4	2.11E-02
L6_t2@1_7	melilite	72.3	4.5	1.7	-3.9	3.9	-6.2	4.0	-5.2	5.5	2.16E-02
L6_t2@1_9	melilite	104.0	7.5	1.8	0.8	3.8	-3.1	3.9	-2.1	5.4	2.13E-02
L6_t2@1_10	melilite	119.8	6.3	1.8	-1.8	4.0	-5.1	4.1	-4.1	5.5	2.21E-02
L6_t2@1_11	melilite	135.6	4.3	1.7	-3.9	4.0	-6.2	4.1	-5.1	5.6	2.19E-02
L6_t2@1_12	melilite	152.4	7.0	1.8	-5.5	4.1	-9.1	4.2	-8.1	5.7	2.23E-02
L6_t2@1_13	melilite	168.0	2.8	1.8	-7.5	4.1	-9.0	4.2	-7.9	5.6	2.32E-02
L6_t2@1_14	melilite	183.8	2.8	1.9	-5.2	4.2	-6.6	4.3	-5.6	5.7	2.28E-02
L6_t2@1_15	melilite	198.9	5.4	1.9	-5.3	4.0	-8.1	4.1	-7.1	5.6	2.16E-02
L6_t2@1_16	melilite	215.4	7.7	1.9	-0.7	3.7	-4.7	3.8	-3.7	5.4	2.32E-02
L6_t2@1_17	melilite	230.8	4.1	1.9	-7.9	4.1	-10.1	4.2	-9.1	5.7	2.30E-02
L6_t2@1_18	melilite	246.8	2.0	2.0	-4.9	4.3	-5.9	4.4	-4.9	5.8	2.26E-02
L6_t2@1_19	melilite	262.7	1.1	1.8	-7.7	3.9	-8.3	4.0	-7.3	5.5	2.38E-02
L6_t2@1_20	melilite	278.9	4.5	1.9	-3.4	4.2	-5.7	4.3	-4.7	5.7	2.45E-02
L6_t2@1_21	melilite	294.1	4.1	1.7	-3.1	4.0	-5.2	4.1	-4.2	5.5	2.31E-02
L6_t2@1_22	melilite	310.2	3.3	1.9	-4.3	4.0	-6.0	4.1	-5.0	5.5	2.33E-02
L6_t2@1_24	melilite	341.2	2.7	1.8	-6.7	4.1	-8.1	4.2	-7.1	5.6	2.24E-02
L6_t2@1_26	melilite	373.0	9.8	1.9	0.2	4.4	-4.9	4.5	-3.9	5.8	2.11E-02
L6_t2@1_27	melilite	387.6	9.7	1.9	3.7	4.1	-1.4	4.2	-0.4	5.6	2.20E-02
L6_t2@1_28	melilite	403.4	5.1	1.9	-2.7	4.4	-5.4	4.5	-4.3	5.8	2.27E-02
L6_t2@1_29	melilite	418.6	5.5	1.8	-7.2	3.8	-10.0	3.9	-9.0	5.4	2.25E-02
L6_t2@1_30	melilite	434.0	6.0	1.8	-5.4	3.6	-8.5	3.8	-7.5	5.3	2.30E-02
Traverse 4 (March 2013)											
L6_t4_1@1_1	melilite $\pm$ Ti pyroxene	-208.8	-40.0	1.8	-39.8	3.6	-19.0	3.7	-18.0	5.2	2.17E-02
L6_t4_1@1_2	melilite	-193.6	4.7	1.9	-3.9	4.1	-6.4	4.2	-5.4	5.6	1.82E-02
L6_t4_1@1_3	melilite $\pm$ spinel?	-179.2	-46.8	1.7	-51.0	3.5	-26.6	3.6	-25.6	5.2	2.02E-02
L6_t4_1@1_4	melilite	-164.0	-12.7	1.9	-18.7	3.9	-12.0	4.0	-11.0	5.5	1.74E-02
L6_t4_1@1_5	melilite	-147.5	-23.7	1.9	-29.2	3.7	-16.9	3.8	-15.9	5.4	2.17E-02
L6_t4_1@1_6	melilite	-132.0	-12.0	1.8	-21.9	3.9	-15.6	4.0	-14.6	5.5	1.91E-02
L6_t4_1@1_7	melilite $\pm$ spinel	-117.2	8.3	2.0	-1.4	4.2	-5.8	4.3	-4.7	5.7	1.63E-02
L6_t4_1@1_10	spinel	-81.2	-40.1	2.0	-45.3	3.9	-24.4	4.1	-24.7	5.7	8.34E-04
L6_t4_1@1_11	Ti pyx	-71.8	-16.2	1.5	-20.0	3.3	-11.5	3.4	-11.8	5.3	2.94E-02
L6_t4_1@1_12	melilite	-61.1	5.8	1.9	-2.3	3.9	-5.3	4.1	-4.3	5.5	2.07E-02
L6_t4_1@1_13	melilite	-52.1	7.2	1.8	-0.9	3.7	-4.6	3.9	-3.6	5.4	2.07E-02
L6_t4_1@1_14	spinel	-29.7	-41.8	2.1	-45.6	4.1	-23.9	4.2	-24.1	5.5	5.92E-05
L6_t4_1@1_15	spinel	-0.2	-41.9	2.0	-46.9	4.5	-25.0	4.6	-25.3	5.8	3.09E-05
Traverse 1 (March 2013)											
L6_t1@1_1	melilite	-48.0	4.4	2.0	-3.0	3.8	-5.4	3.9	-4.3	5.4	2.10E-02
L6_t1@1_2	low Ti pyx	-33.6	-12.8	2.0	-15.3	4.0	-8.6	4.1	-8.9	5.8	1.53E-02
L6_t1@1_4	melilite	14.5	-8.4	1.7	-14.0	3.8	-9.6	3.9	-8.6	5.4	2.16E-02
L6_t1@1_5	spinel	29.4	-38.6	2.1	-42.7	4.4	-22.6	4.5	-22.8	5.8	2.69E-04
L6_t1@1_6	melilite	43.8	-4.6	1.9	-13.8	3.8	-11.4	3.9	-10.4	5.4	1.98E-02
L6_t1@1_7	melilite	59.3	-4.8	1.7	-13.0	3.9	-10.4	4.0	-9.4	5.4	2.05E-02
L6_t1@1_10	melilite	104.7	8.2	1.9	0.7	4.0	-3.5	4.2	-2.5	5.6	2.13E-02
L6_t1@1_11	melilite	119.9	7.9	1.9	1.1	3.7	-3.0	3.9	-2.0	5.4	2.37E-02
L6_t1@1_12	melilite	134.9	5.6	1.9	-1.3	3.9	-4.2	4.0	-3.2	5.5	2.24E-02
L6_t1@1_13	melilite	149.6	6.4	1.8	0.6	4.1	-2.7	4.2	-1.7	5.6	2.29E-02
L6_t1@1_14	melilite	165.0	5.4	1.8	-3.2	4.1	-6.0	4.2	-5.0	5.6	2.38E-02
L6_t1@1_15	melilite	180.5	5.5	2.0	-3.7	4.1	-6.6	4.2	-5.6	5.7	2.34E-02
Traverse 3 (March 2013)											
L6_t3@1_1	Ti pyx	-71.9	-20.0	1.6	-23.6	3.5	-13.1	3.5	-13.4	5.4	2.45E-02
L6_t3@1_2	spinel	-32.4	-38.7	1.8	-46.6	4.0	-26.4	4.1	-26.7	5.4	1.11E-04
L6_t3@1_3	spinel	-22.9	-43.4	1.9	-47.8	4.0	-25.2	4.1	-25.5	5.4	2.11E-05
L6_t3@1_4	spinel	-13.0	-41.4	2.1	-47.3	4.1	-25.7	4.3	-26.0	5.6	9.27E-05
L6_t3@1_5	spinel	-2.9	-40.3	2.2	-47.6	3.8	-26.6	4.0	-26.9	5.4	2.43E-05
L6_t3@1_6	spinel	0.0	-42.3	2.1	-44.3	4.2	-22.3	4.3	-22.5	5.6	2.07E-04
L6_t3@1_7	melilite	1.1	-40.1	1.9	-40.7	3.9	-19.8	4.0	-18.8	5.5	1.95E-02
L6_t3@1_8	melilite	4.7	-14.3	1.9	-21.5	4.2	-14.1	4.3	-13.0	5.7	1.93E-02
L6_t3@1_9	melilite	10.2	-16.3	1.8	-29.3	4.1	-20.8	4.2	-19.8	5.6	1.97E-02
L6_t3@1_10	melilite	17.1	-10.0	1.8	-18.2	3.6	-13.0	3.7	-12.0	5.3	2.05E-02
L6_t3@1_11	melilite	25.4	-12.1	1.9	-15.5	3.9	-9.2	4.0	-8.2	5.5	2.02E-02
L6_t3@1_13	melilite	42.8	-13.9	1.7	-19.6	4.0	-12.4	4.1	-11.4	5.5	1.93E-02
L6_t3@1_14	melilite	51.5	-4.0	1.8	-10.5	3.7	-8.4	3.8	-7.4	5.3	2.08E-02
L6_t3@1_15	melilite	61.6	-4.6	1.8	-13.0	4.0	-10.6	4.1	-9.6	5.5	2.05E-02
Pyroxene (January 2014)											
L6_2	diopside	-247.1	-51.9	2.0	-48.6	3.2	-21.5	3.3	-20.3	4.7	3.62E-02
L6_3	Ti pyx	-238.1	-38.9	2.0	-37.6	3.1	-17.4	3.3	-16.1	4.7	2.14E-02
L6_4	Ti pyx	-241.1	-42.6	2.4	-36.5	3.3	-14.3	3.5	-13.0	4.8	1.77E-02
L6_5	diopside	-245.0	-24.7	2.5	-26.4	3.6	-13.5	3.9	-12.3	5.1	3.64E-02
L6_7	diopside	-243.0	-46.5	1.9	-44.8	3.2	-20.6	3.3	-19.3	4.7	3.72E-02
L6_8	diopside	-249.4	-39.5	2.0	-38.2	3.3	-17.6	3.4	-16.3	4.8	3.78E-02

\* Standard mineral-specific instrumental corrections applied to measurements (i.e., olivine, anorthite, or spinel). Uncertainties include propagation of measured  $2\sigma$  counting statistics and  $2\sigma$  systematic errors of the mean for each mineral standard. These data are plotted in Figures 9 and 10.

\*\* Average standard mineral instrumental corrections applied to measurements. Uncertainties reflect the propagation of measured  $2\sigma$  counting statistics and  $2\sigma$  scatter about the mean derived from all mineral standard measurements.

Table 1. ALH3 Oxygen Isotope Data

Spot	Mineral	From Edge of Inclusion ( $\mu\text{m}$ )	$\delta^{18}\text{O}/^{16}\text{O}^*$	$2\sigma(\%)^*$	$\delta^{17}\text{O}/^{16}\text{O}^*$	$2\sigma(\%)^*$	$\Delta^{17}\text{O}^*$	$2\sigma(\%)^*$	$\Delta^{17}\text{O}^{**}$	$2\sigma(\%)^{**}$	$^{28}\text{Si}/^{16}\text{O}$
Traverse 4 (December 2012)											
ALH3_t4_1	olivine	-81	-12.8	1.6	-17.2	2.6	-10.6	2.8	-11.3	4.7	2.32E-02
ALH3_t4_2	olivine	-73	-0.2	1.7	0.2	2.5	0.3	2.7	-0.4	4.6	2.19E-02
ALH3_t4_3	Al-pyroxene	-64	-5.2	1.7	-11.3	2.8	-8.6	3.0	-9.3	4.8	3.65E-02
ALH3_t4_4	Ti-pyroxene	-53	-14.4	1.8	-18.9	3.2	-11.4	3.4	-12.1	5.1	1.58E-02
ALH3_t4_5	Ti pyroxene	-39	-37.8	1.7	-34.7	3.1	-15.0	3.2	-15.8	5.0	9.16E-03
ALH3_t4_6	spinel on crack	-5	-43.6	1.3	-46.4	2.9	-23.7	3.0	-24.4	5.0	1.39E-03
ALH3_t4_7	plagioclase on crack	4	-8.8	1.8	-1.8	3.2	2.8	3.3	4.1	5.0	3.47E-02
ALH3_t4_8a	plagioclase on crack	14	-13.2	1.5	-6.6	2.9	0.3	3.0	1.6	4.8	6.38E-02
ALH3_t4_9	melilite	24	5.1	1.9	-2.8	3.2	-5.4	3.3	-4.1	5.0	2.18E-02
ALH3_t4_10	melilite	33	1.9	1.7	-6.8	3.2	-7.7	3.3	-6.4	5.0	2.29E-02
ALH3_t4_11	melilite	42	-3.9	1.7	-10.4	2.9	-8.4	3.1	-7.1	4.9	2.12E-02
ALH3_t4_12	melilite	52	-1.9	1.9	-10.3	3.3	-9.3	3.5	-8.0	5.1	1.89E-02
ALH3_t4@1_1	melilite	70	-0.9	1.7	-8.1	3.0	-7.7	3.1	-6.4	4.9	2.20E-02
ALH3_t4@1_2	melilite	89	-1.2	1.7	-8.4	3.4	-7.8	3.5	-6.5	5.1	2.00E-02
ALH3_t4@1_3	melilite	110	3.7	1.7	-4.5	3.0	-6.5	3.2	-5.2	4.9	2.03E-02
ALH3_t4@1_4	melilite+grossular	129	3.8	1.9	0.6	3.8	-1.4	3.9	-0.1	5.5	2.45E-02
ALH3_t4@1_5	melilite	149	3.0	1.7	-5.5	3.1	-7.1	3.2	-5.8	5.0	2.11E-02
ALH3_t4@1_6	melilite	169	1.6	1.7	-5.5	3.2	-6.4	3.3	-5.1	5.0	2.05E-02
ALH3_t4@1_7	melilite	189	4.2	1.7	-3.5	3.3	-5.7	3.4	-4.4	5.1	2.20E-02
ALH3_t4@1_8	melilite	209	3.9	1.8	-0.9	3.3	-2.9	3.4	-1.6	5.1	2.02E-02
ALH3_t4@1_9	melilite	228	2.9	1.8	-2.7	3.3	-4.2	3.4	-2.9	5.1	2.56E-02
ALH3_t4@1_10	melilite	248	14.4	1.8	3.6	3.1	-3.9	3.2	-2.6	5.0	3.17E-02
Traverse 3 (December 2012)											
		From edge of inclusion									
ALH3_t3_1a	olivine	-75	-52.2	1.5	-52.9	2.4	-25.7	2.5	-27.8	4.8	2.39E-02
ALH3_t3_2a	olivine	-66	-46.9	1.5	-49.6	2.4	-25.1	2.6	-27.2	4.8	2.54E-02
ALH3_t3_3a	Al-pyroxene	-56	-19.2	1.7	-21.1	3.0	-11.1	3.4	-13.5	5.1	3.85E-02
ALH3_t3_4	Ti-pyroxene	-45	-15.6	1.8	-15.4	3.1	-7.3	3.1	-8.4	5.1	2.22E-02
ALH3_t3_5	grossular	-39	5.2	1.8	-0.6	3.5	-3.3	3.6	-3.3	5.4	2.41E-02
ALH3_t3_6	spinel+grossular	-2	-27.6	1.5	-30.0	3.0	-15.6	3.1	-17.7	5.2	1.05E-02
ALH3_t3_3	spinel	0	-47.9	1.1	-49.2	2.4	-24.2	2.4	-24.4	4.6	3.49E-04
Near Traverse 3 near edge (December 2012)											
		From edge of inclusion									
ALH3_t3_1	melilite	35	-5.2	1.7	-12.4	2.9	-9.7	3.0	-8.4	4.8	2.57E-02
ALH3_t3_2	melilite	45	-6.1	1.5	-9.5	2.9	-6.3	3.0	-5.1	4.8	3.41E-02
Traverse 2 at edge of inner pocket (December 2012)											
		From edge of pocket									
ALH3_t2_1	Andradite	-65	-8.1	1.5	-5.4	2.2	-1.2	2.3	-1.9	4.4	4.04E-02
ALH3_t2_2	Al-pyroxene	-49	-41.6	1.7	-42.7	3.0	-21.0	3.1	-22.1	4.9	3.64E-02
ALH3_t2_3	Al-pyroxene	-38	-3.2	1.6	-5.6	2.7	-4.0	2.9	-5.0	4.7	3.69E-02
ALH3_t2_4	spinel	-18	-44.8	1.3	-42.4	3.0	-19.1	3.1	-19.8	5.1	1.58E-05
ALH3_t2_5	spinel	-10	-40.2	1.3	-44.3	2.9	-23.3	3.0	-24.1	5.0	5.70E-05
ALH3_t2_6	melilite $\pm$ spl	7	-16.1	1.6	-18.5	2.9	-10.1	3.0	-8.8	4.8	2.44E-02
ALH3_t2_7	melilite	21	-10.2	1.6	-13.1	3.1	-7.8	3.2	-6.5	4.9	2.34E-02
Traverse 1 at edge of inner pocket (December 2012)											
		From edge of pocket									
ALH3_t1_1	Andradite	-65	10.1	1.7	1.9	3.1	-3.4	3.2	-4.1	5.0	2.76E-02
ALH3_t1_2	Al-pyroxene	-51	-2.4	1.8	-7.9	3.0	-6.6	3.2	-7.4	4.9	2.81E-02
ALH3_t1_3	Ti-pyroxene	-42	-16.1	1.9	-15.7	3.7	-7.3	3.8	-8.0	5.4	1.64E-02
ALH3_t1_4	spinel	-34	-43.3	1.4	-44.5	3.1	-21.9	3.2	-22.6	5.1	1.95E-05
ALH3_t1_5	spinel	-21	-43.9	1.5	-43.0	3.3	-20.2	3.4	-20.9	5.2	9.99E-05
ALH3_t1_6	spinel	-10	-41.9	1.4	-43.3	3.3	-21.5	3.4	-22.2	5.3	5.76E-05
ALH3_t1_7	spinel+melilite>perosk	0	-27.7	1.3	-31.8	2.8	-17.3	2.9	-18.1	5.0	4.71E-05
ALH3_t1_8	melilite	11	-7.6	1.7	-15.0	3.3	-11.0	3.4	-9.7	5.1	1.95E-02

\* Standard mineral-specific instrumental corrections applied to measurements (i.e., olivine, anorthite, or spinel). Uncertainties include propagation of measured  $2\sigma$  counting statistics and  $2\sigma$  systematic errors of the mean for each mineral standard. These data are plotted in Figures 9 and 10.

\*\* Average standard mineral instrumental corrections applied to measurements. Uncertainties reflect the propagation of measured  $2\sigma$  counting statistics and  $2\sigma$  scatter about the mean derived from all mineral standard measurements.

Spot	Mineral	From Edge of Inclusion (μm)	$\delta^{18}\text{O}/^{16}\text{O}^*$	$2\sigma$ (‰)*	$\delta^{17}\text{O}/^{16}\text{O}^*$	$2\sigma$ (‰)*	$\Delta^{17}\text{O}^*$	$2\sigma$ (‰)*	$\Delta^{17}\text{O}^{**}$	$2\sigma$ (‰)**	$^{28}\text{Si}/^{16}\text{O}$
<b>Traverse-1 (August 2011)</b>											
EF_matrix_2	olivine matrix	-38	10.9	1.6	6.6	3.6	0.9	3.7	1.8	5.2	1.18E-03
EF_matrix_3	olivine matrix	-31	8.5	1.7	0.0	3.3	-4.4	3.4	-3.5	5.0	1.18E-03
EF_matrix_4	olivine matrix	-25	6.4	1.9	1.0	3.7	-2.3	3.8	-1.5	5.2	1.16E-03
EF_WL_7	spinel	-6	-30.8	2.2	-35.8	3.5	-19.7	3.6	-19.8	5.2	5.12E-04
EF_WL_8	spinel + diopside	-5	-44.1	2.4	-46.3	4.3	-23.3	4.5	-23.4	5.8	2.46E-04
EF_WL_9	spinel + << melilite	0	-39.5	2.4	-41.5	4.2	-21.0	4.3	-21.1	5.7	2.78E-05
EF_interior_1	melilite	Interior margin	5.1	2.0	-1.1	3.9	-3.7	4.0	-5.3	5.2	8.80E-04
<b>Traverse-2 (August 2011)</b>											
EF_matrix_13	olivine matrix	-21	6.0	1.6	2.7	3.3	-0.4	3.5	0.5	5.0	1.21E-03
EF_WL_12	Ti pyroxene	-15	-44.8	1.8	-43.8	3.7	-20.5	3.8	-19.6	5.3	1.31E-03
EF_WL_11	Ti pyroxene	-9	-25.9	1.7	-25.0	3.5	-11.5	3.7	-10.6	5.2	1.23E-03
EF_WL_14	spinel	-2	-35.3	2.1	-40.1	3.4	-21.7	3.6	-21.8	5.1	2.19E-05
EF_interior_15	melilite	5	-21.2	1.8	-16.6	4.2	-5.6	4.3	-7.1	5.3	9.65E-04
EF_interior_17	melilite	15	-8.5	1.9	-10.5	3.5	-6.1	3.6	-7.7	4.8	9.15E-04
EF_interior_18	melilite	21	-18.3	1.9	-14.4	3.9	-4.9	4.0	-6.4	5.1	9.08E-04
EF_interior_19	melilite	28	-0.7	1.9	-7.6	3.5	-7.3	3.6	-8.8	4.8	1.27E-03
EF_interior_20	melilite	34	-13.9	2.1	-12.0	3.5	-4.8	3.7	-6.3	4.9	1.03E-03
EF_interior_21	melilite	40	1.5	1.9	-0.3	3.4	-1.1	3.6	-2.6	4.8	1.47E-03
EF_interior_22	melilite	52	-11.3	2.1	-12.2	4.3	-6.3	4.5	-7.8	5.5	1.41E-03
EF_interior_23	melilite	68	-2.9	2.6	-5.4	4.5	-3.9	4.7	-5.5	5.7	1.70E-03
EF_interior_26	melilite	93	-1.8	2.0	-3.6	4.3	-2.7	4.4	-4.2	5.5	1.48E-03
EF_interior_27	melilite	111	-6.6	1.9	-4.9	3.5	-1.5	3.6	-3.0	4.8	1.47E-03
EF_interior_28	melilite	131	-6.1	2.7	-6.0	4.3	-2.8	4.5	-4.3	5.5	1.26E-03
EF_interior_29	melilite	161	4.8	2.0	0.5	3.7	-2.0	3.8	-3.5	5.0	1.51E-03
EF_interior_25	spinel	179	-39.7	2.1	-41.7	3.7	-21.0	3.9	-21.1	5.4	8.24E-06
EF_interior_30	melilite	192	6.4	2.4	3.6	4.3	0.3	4.5	-1.3	5.5	1.51E-03
EF_interior_32	melilite	264	6.4	1.9	0.8	3.6	-2.5	3.7	-4.0	4.9	1.52E-03

\* Standard mineral-specific instrumental corrections applied to measurements (i.e., olivine, anorthite, or spinel). Uncertainties include propagation of measured  $2\sigma$  counting statistics and  $2\sigma$  systematic errors of the mean for each mineral standard. These data are plotted in Figures 9 and 10.

\*\* Average standard mineral instrumental corrections applied to measurements. Uncertainties reflect the propagation of measured  $2\sigma$  counting statistics and  $2\sigma$  scatter about the mean derived from all mineral

Table 2. Representative electron probe analyses of melilite.

	1.	2.	3.	4.	5.	6.	7.	8.	9.	10.
Na <sub>2</sub> O	0.03	0.02	0.04	0.02	0.02	0.00	0.02	0.02	0.18	0.13
MgO	2.61	1.18	1.61	1.49	1.84	2.10	0.87	4.14	6.90	4.62
Al <sub>2</sub> O <sub>3</sub>	31.8	33.62	32.38	33.13	31.21	30.40	33.76	25.33	18.67	23.68
SiO <sub>2</sub>	25.42	24.20	24.87	23.49	24.55	24.78	22.35	27.37	33.26	28.94
CaO	39.78	40.13	40.17	40.27	40.93	41.04	41.02	40.89	40.91	40.69
TiO <sub>2</sub>	0.07	0.02	0.09	0.00	0.01	0.04	0.08	0.00	0.02	0.04
Cr <sub>2</sub> O <sub>3</sub>	0.02	0.00	0.01	n.d.						
MnO	0.01	0.02	0.01	n.d.						
FeO	0.14	0.08	0.01	0.13	0.01	0.05	0.00	0.00	n.d.	n.d.
SUM	99.91	99.28	99.19	98.54	98.56	98.41	98.10	97.76	99.94	98.10
Cations per 7 oxygens										
Na	0.003	0.002	0.004	0.002	0.002	0.000	0.002	0.002	0.016	0.012
Mg	0.177	0.081	0.110	0.103	0.127	0.146	0.061	0.289	0.468	0.321
Al	1.705	1.816	1.750	1.809	1.706	1.666	1.860	1.397	1.001	1.299
Si	1.157	1.109	1.141	1.089	1.139	1.153	1.045	1.281	1.513	1.347
Ca	1.939	1.971	1.974	2.000	2.034	2.045	2.054	2.051	1.994	2.029
Ti	0.002	0.000	0.003	0.000	0.000	0.001	0.003	0.000	0.001	0.002
Fe	0.005	0.003	0.000	0.005	0.000	0.002	0.000	0.000	—	—
Total	4.989	4.983	4.983	5.008	5.009	5.013	5.024	5.021	4.993	5.008
Åk	17.2	8.2	11.1	9.2	14.3	16.0	5.7	29.1	50.6	34.9

1: Ef-1, edge. 2,3: Ef-1, interior. 4 – 6: L6, outer melilite. 7, 8: L6, inner melilite. 9, 10: TS4.  
n.d.: not determined.

Table 3. Electron probe analyses of pyroxene in L6.

	1.	2.	3.	4.	5.	6.	7.
MgO	6.98	5.37	13.47	17.77	7.34	4.66	18.98
Al <sub>2</sub> O <sub>3</sub>	19.33	23.51	9.94	3.42	24.06	25.59	1.00
SiO <sub>2</sub>	33.12	29.54	43.38	51.54	30.47	27.79	52.10
CaO	24.49	24.73	24.63	24.99	23.92	24.74	24.86
Ti as TiO <sub>2</sub>	14.30	15.70	7.38	2.38	11.92	15.97	0.13
Sc <sub>2</sub> O <sub>3</sub>	0.21	BDL	BDL	BDL	0.06	0.14	BDL
V <sub>2</sub> O <sub>3</sub>	0.58	0.62	0.09	BDL	0.61	0.93	0.02
FeO	0.02	0.02	0.00	BDL	0.37	0.18	0.74
Ti <sub>2</sub> O <sub>3</sub>	9.18	8.13	2.74	—	3.04	7.47	—
TiO <sub>2</sub>	4.22	6.88	4.27	—	8.35	7.86	—
Sum	98.30	98.80	98.51	100.10	98.15	99.20	98.26
Si	1.275	1.142	1.610	1.868	1.149	1.071	1.933
Al	0.725	0.858	0.390	0.132	0.851	0.929	0.044
Al	0.155	0.214	0.044	0.014	0.218	0.233	0.000
Mg	0.400	0.310	0.745	0.959	0.413	0.268	1.049
Fe	0.001	0.001	0.000	0.000	0.012	0.006	0.023
Sc	0.007	0.000	0.000	0.000	0.002	0.005	0.000
V	0.017	0.018	0.003	0.000	0.017	0.027	0.001
Ti <sup>3+</sup>	0.295	0.259	0.086	—	0.097	0.238	—
Ti <sup>4+</sup>	0.122	0.198	0.120	0.065	0.241	0.225	0.004
Ca	1.000	1.000	1.000	0.951	1.000	1.000	0.988
Ti <sup>3+</sup> /Ti <sup>tot</sup>	0.707	0.567	0.417		0.287	0.463	

1. Interior, coarse fassaite, average of 25 analyses. 2. Ti-pyx-1 layer. 3. Ti-pyx-2 (inner zone) 4. Ti-pyx-2 (outer zone). 5. Ti-pyx-3. 6. Ti-pyx-4 7. Al-pyx-5 outermost (diopside) rim. For Ti-rich analyses, Ti<sup>3+</sup>/Ti<sup>4+</sup> proportions calculated according to the method of S. Simon et al. (1991), with normalization of analyses to one Ca and four total cations per six oxygen anions. BDL: Below detection limit of electron microprobe of 0.02 wt%.

Table 4. Summary of Diffusion Exchange Models

		Early Stage ("Step 1")		Environments		Later Stage ("Step 2")		Environments	
Inclusion	Size (cm)*	$\Delta^{17}\text{O}$ (‰)	$\Delta^{17}\text{O}$ (‰)	Nebular	Parent body	$\Delta^{17}\text{O}$ (‰)	$\Delta^{17}\text{O}$ (‰)	Nebular	Parent body
		interior	gas	T (K), t (years)	T (K), t (years)	interior	gas	T (K), t (years)	T (K), t (years)
<i>Idealized CAIs</i>									
molten	0.5	-28	0	1773, $10^0$	nil				
molten	0.5	-28	0	1973, $\leq 10^{-3}$	nil				
solid	0.5	-28	0	1400, $2.5 \times 10^4$	nil				
solid, $P_{\text{tot}}=10^{-2}$	0.5	-28	0	1500, $2 \times 10^3$	nil				
defects <sup>RM</sup>	2.0	-28	0	1400, $10^3$	900, $\geq 10^6$				
defects <sup>RM</sup>	0.5	-28	0	1500, $10^2$	900, $10^6$				
<i>Studied CAIs</i>									
A37	0.5	-28	-20	1400, $\leq 2 \times 10^4$ <sup>m</sup>	1000, $\geq 10^8$	-20	0	1400, $\leq 1.6 \times 10^4$	900, $\geq 10^8$
Egg-6	2.0	-28	0 <sup>t</sup>	1400, $\leq 2.8 \times 10^5$	900, $10^9$ **				
TS4	0.6	-28	-20	1400, $\leq 2 \times 10^4$ <sup>m</sup>	1000, $10^8$	-20	0 <sup>t</sup>	1400, $\leq 3 \times 10^4$	900, $\geq 10^8$
ALH3	0.6	-28	0	1400, $\leq 2.5 \times 10^4$ <sup>m</sup>	1000, $10^8$	-3	-25	1400, $\leq 2 \times 10^4$	900, $\geq 10^8$
Ef-1	0.3 <sup>f</sup>	-28	0	1400, $\leq 10^3$ <sup>m</sup>	900, $\geq 10^8$ **	0	-20	1400, $\leq 5 \times 10^3$	-
L6	0.7 <sup>f</sup>	-28	0	1400, $\leq 3 \times 10^4$ <sup>m</sup>	900, $\geq 10^8$ **	-5	-25	1400, $\leq 3 \times 10^4$	-

\*spherical diameter used for model calculations

<sup>f</sup>original inclusion size unknown

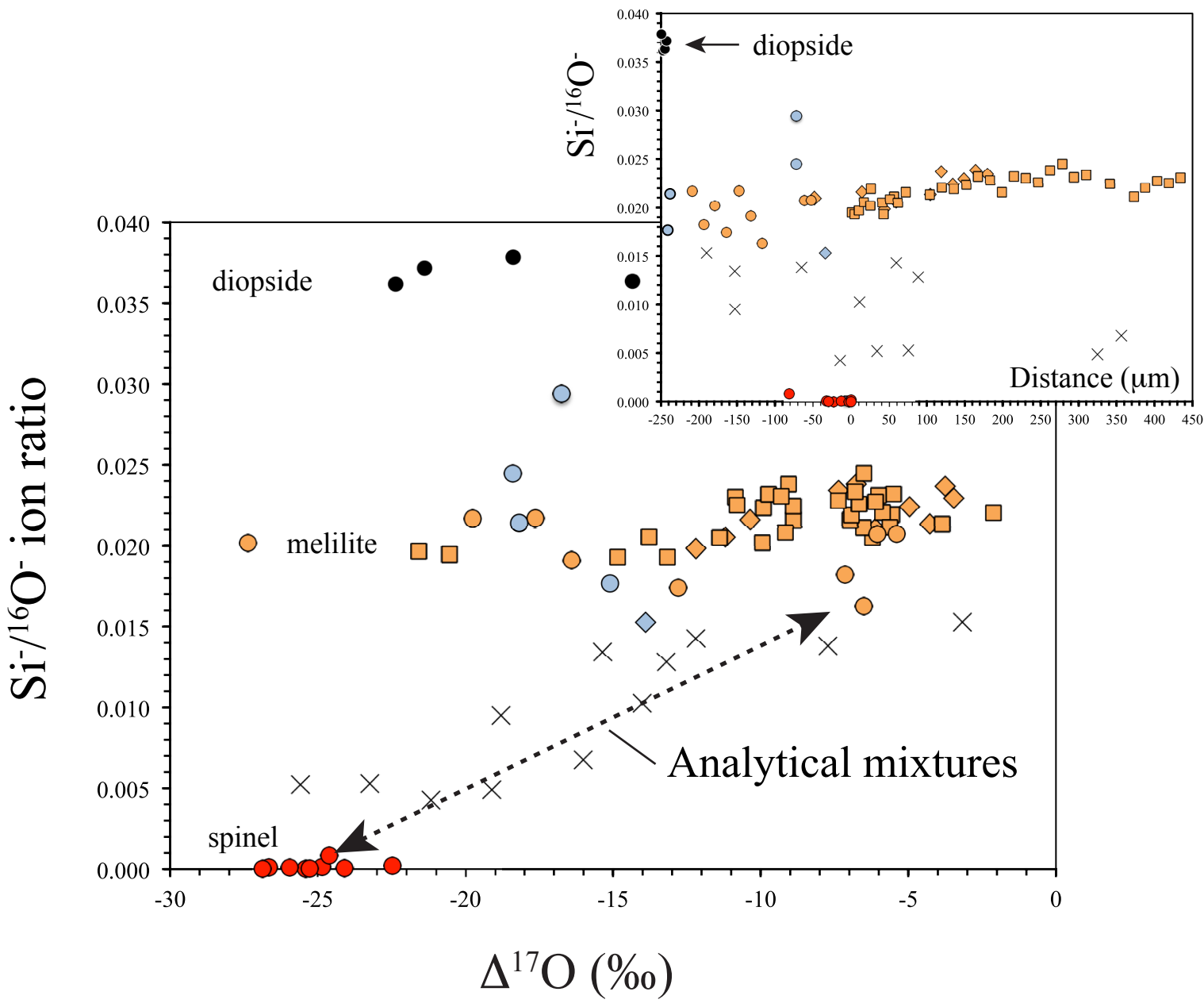
<sup>m</sup>requires early stage of exchange, possibly while protoCAI was molten.

\*\*does not account for the presence of a fluid phase that would make the exchange more efficient.

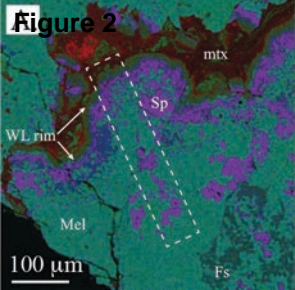
<sup>t</sup>inferred (not seen in the inner most WL rim)

<sup>RM</sup>Near 1000 K, equilibration times exceed  $10^6$  years regardless of the dislocation density within melilite (Ryerson and McKeegan, 1994).

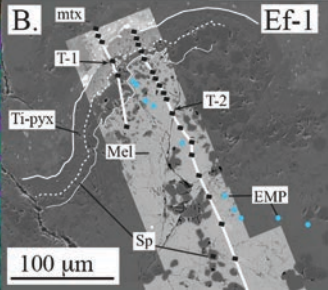
Figure 1



**Figure 2**



**B.**



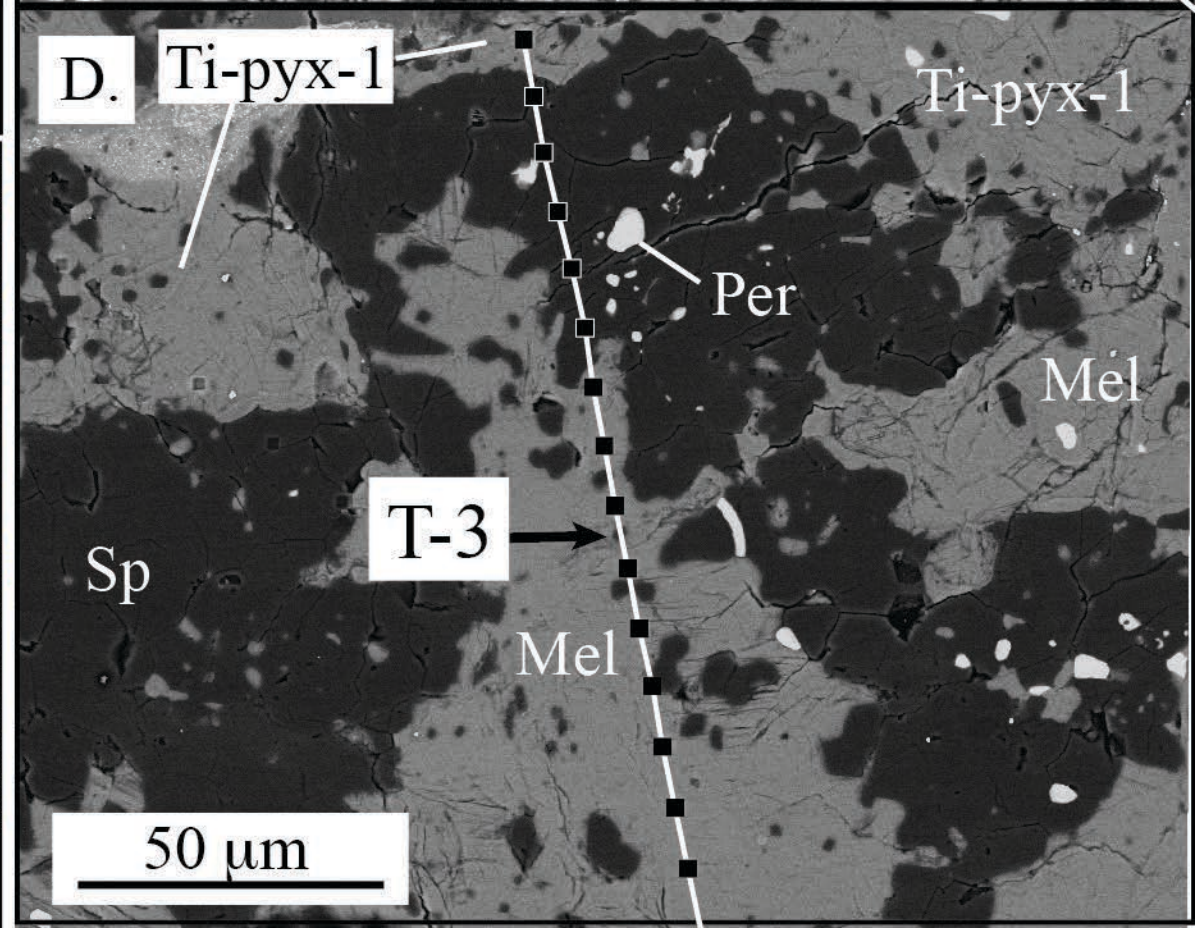
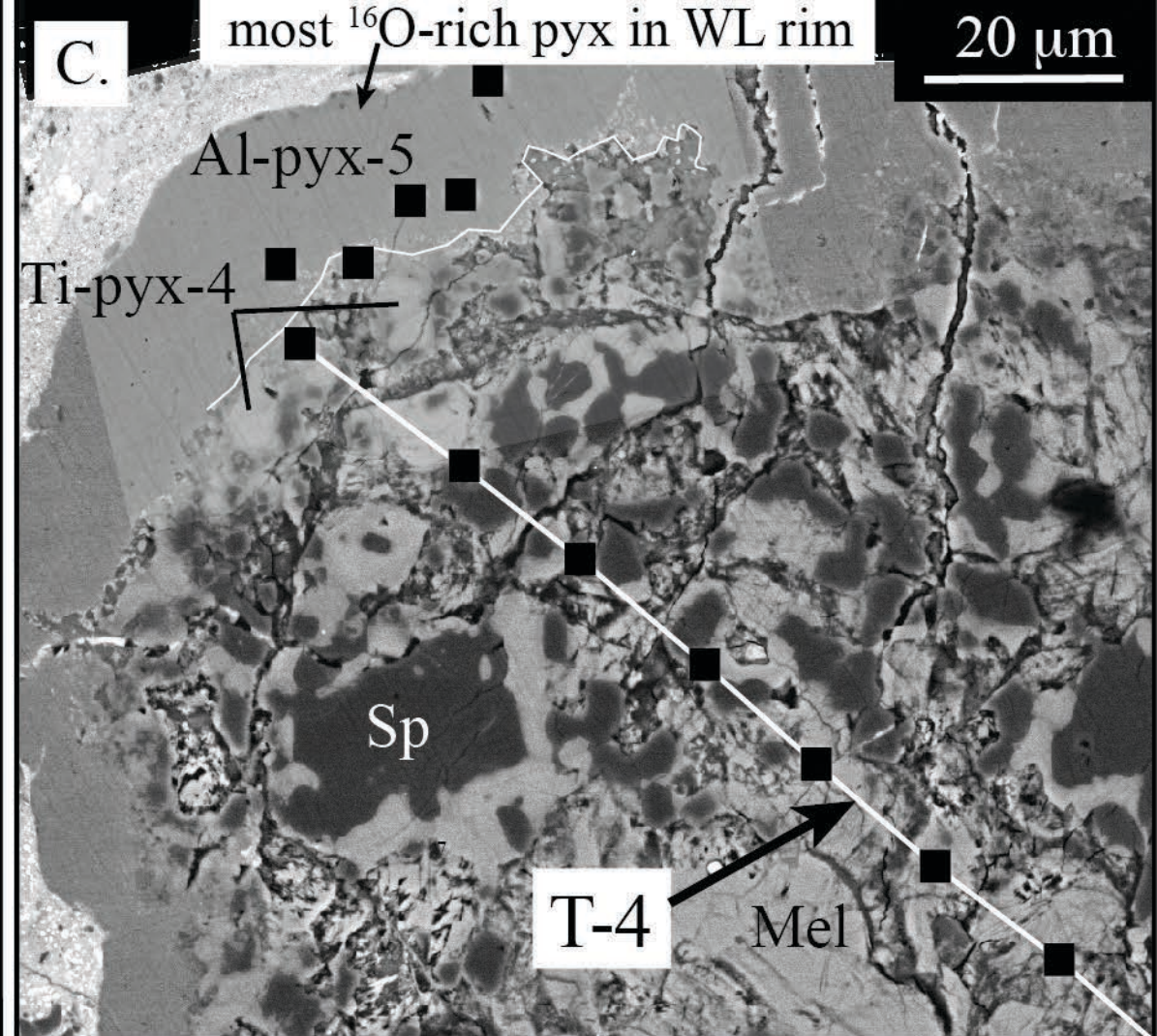
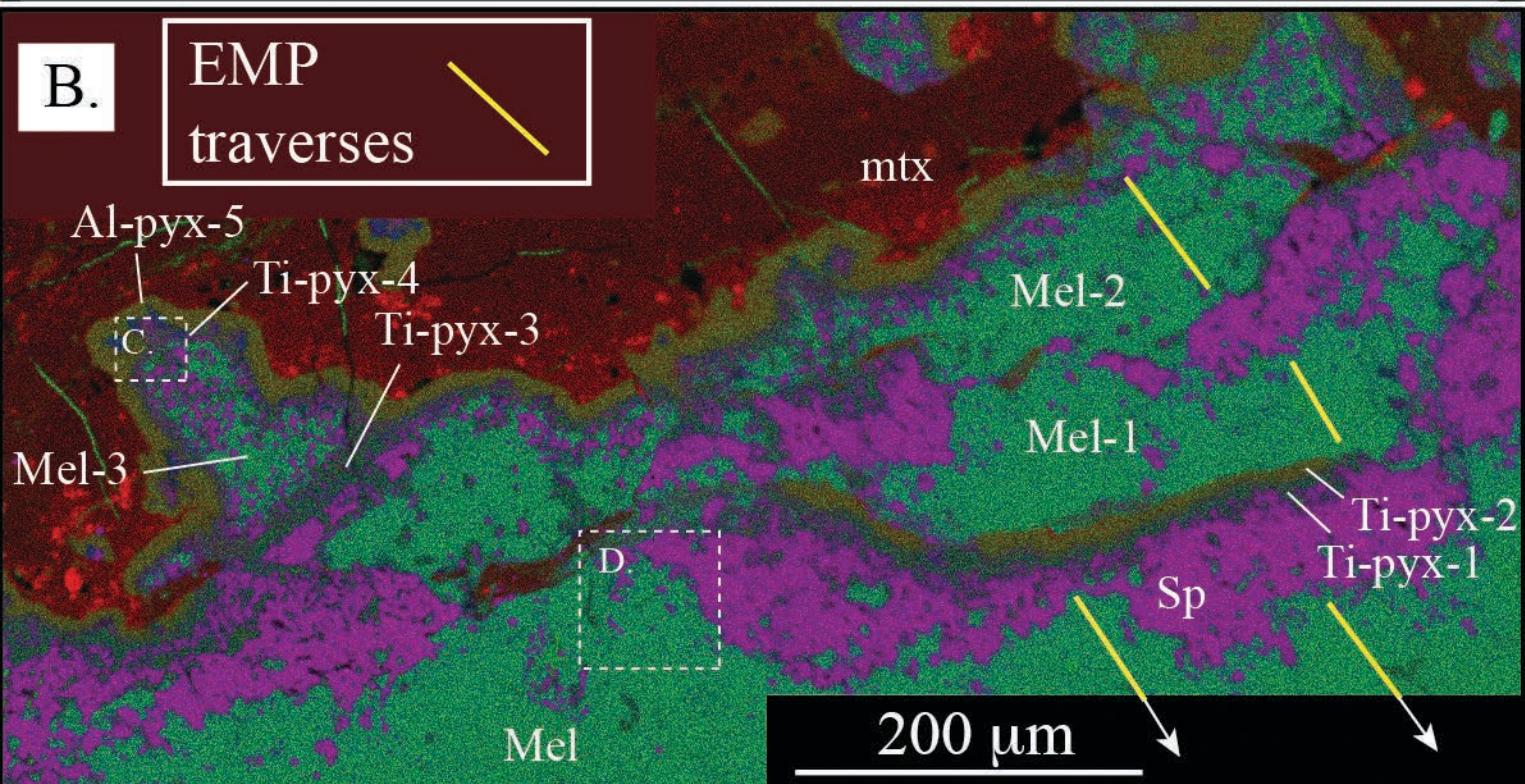
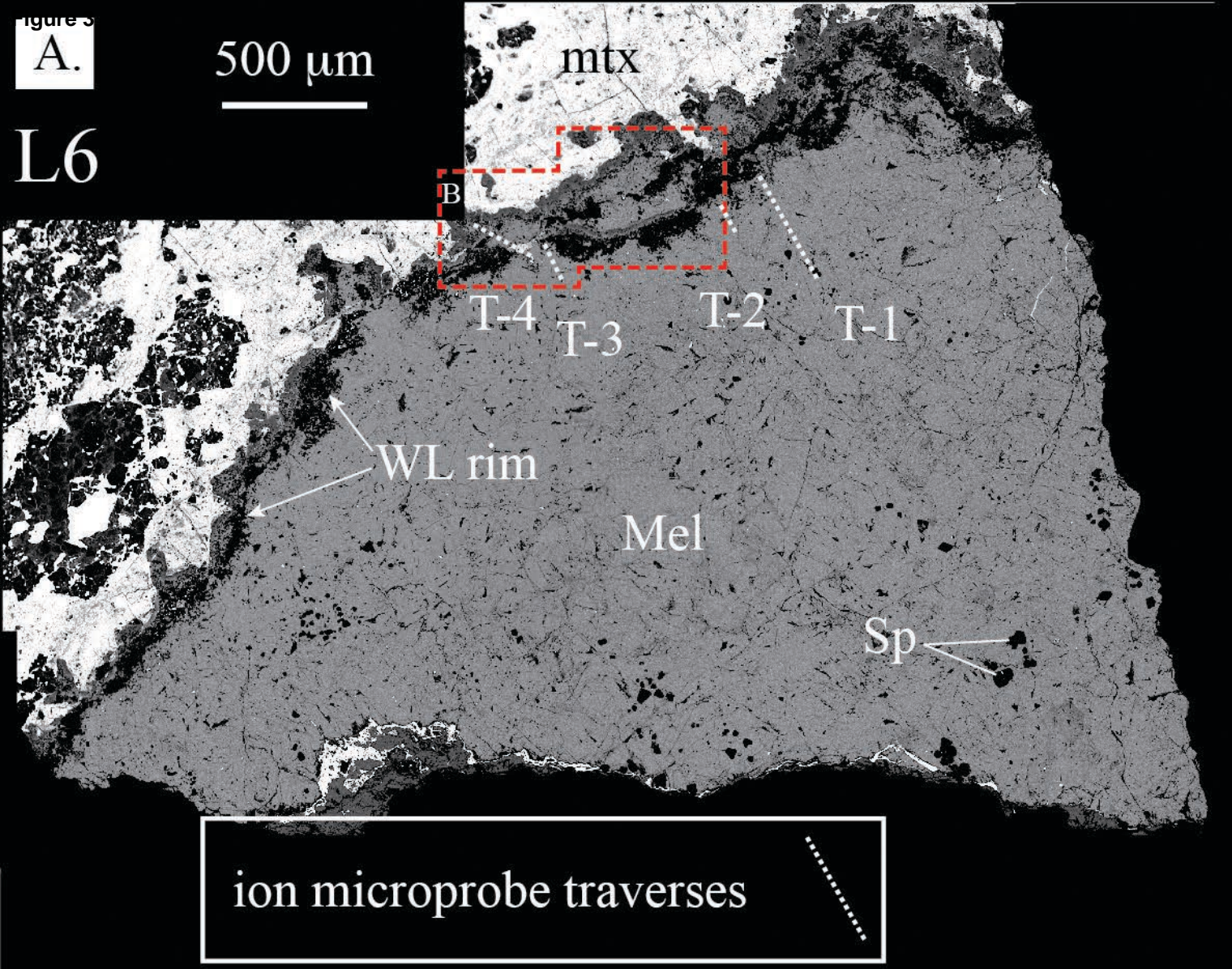
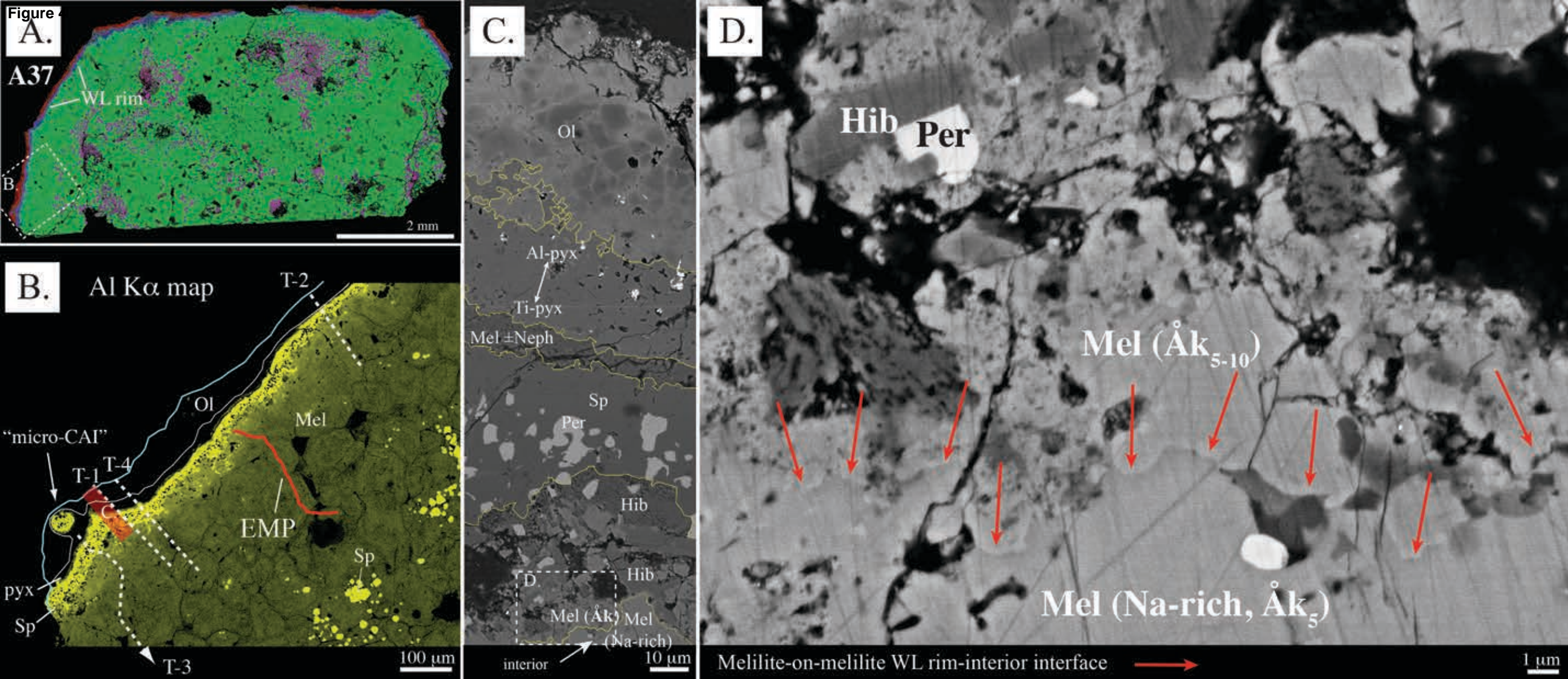
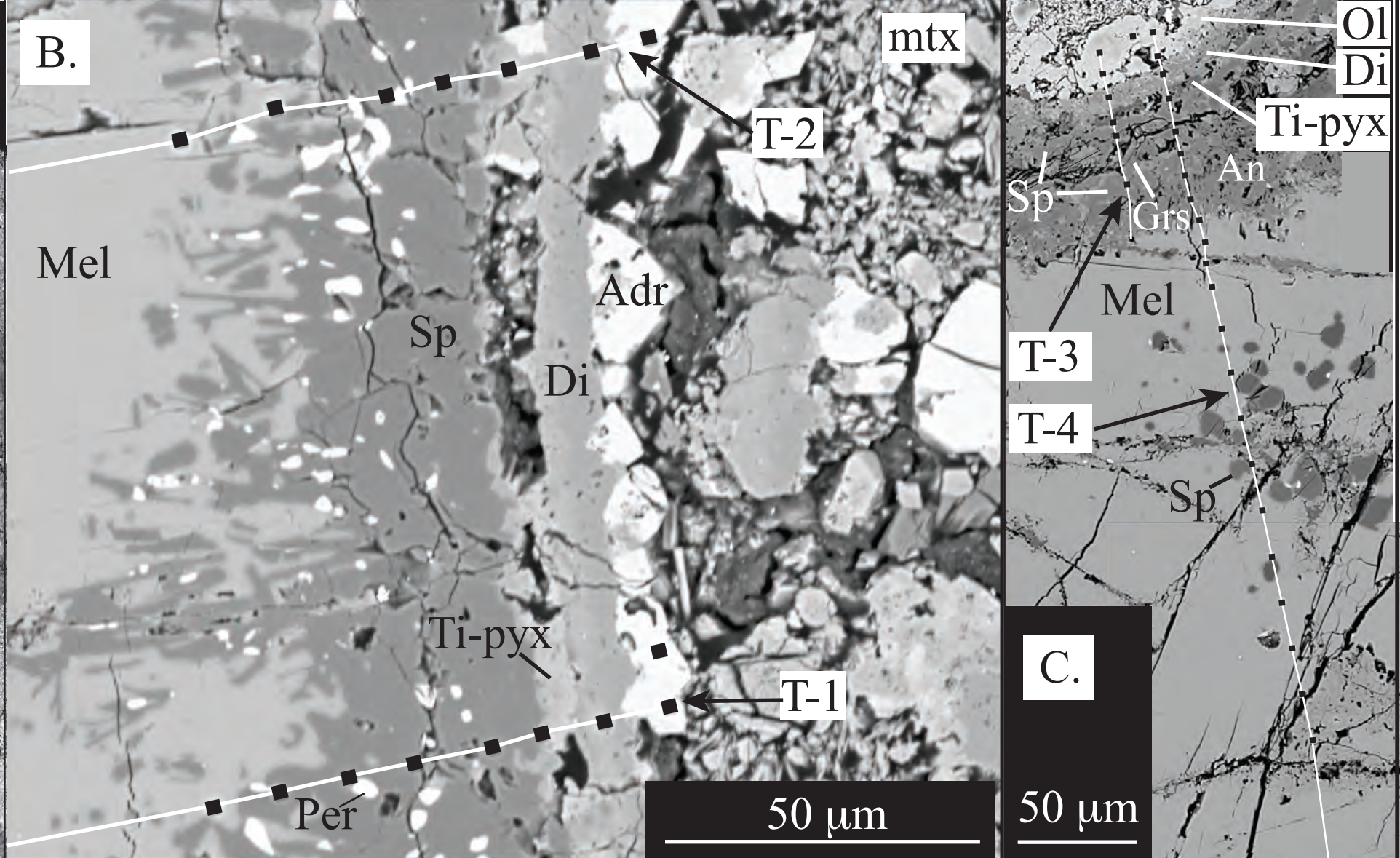
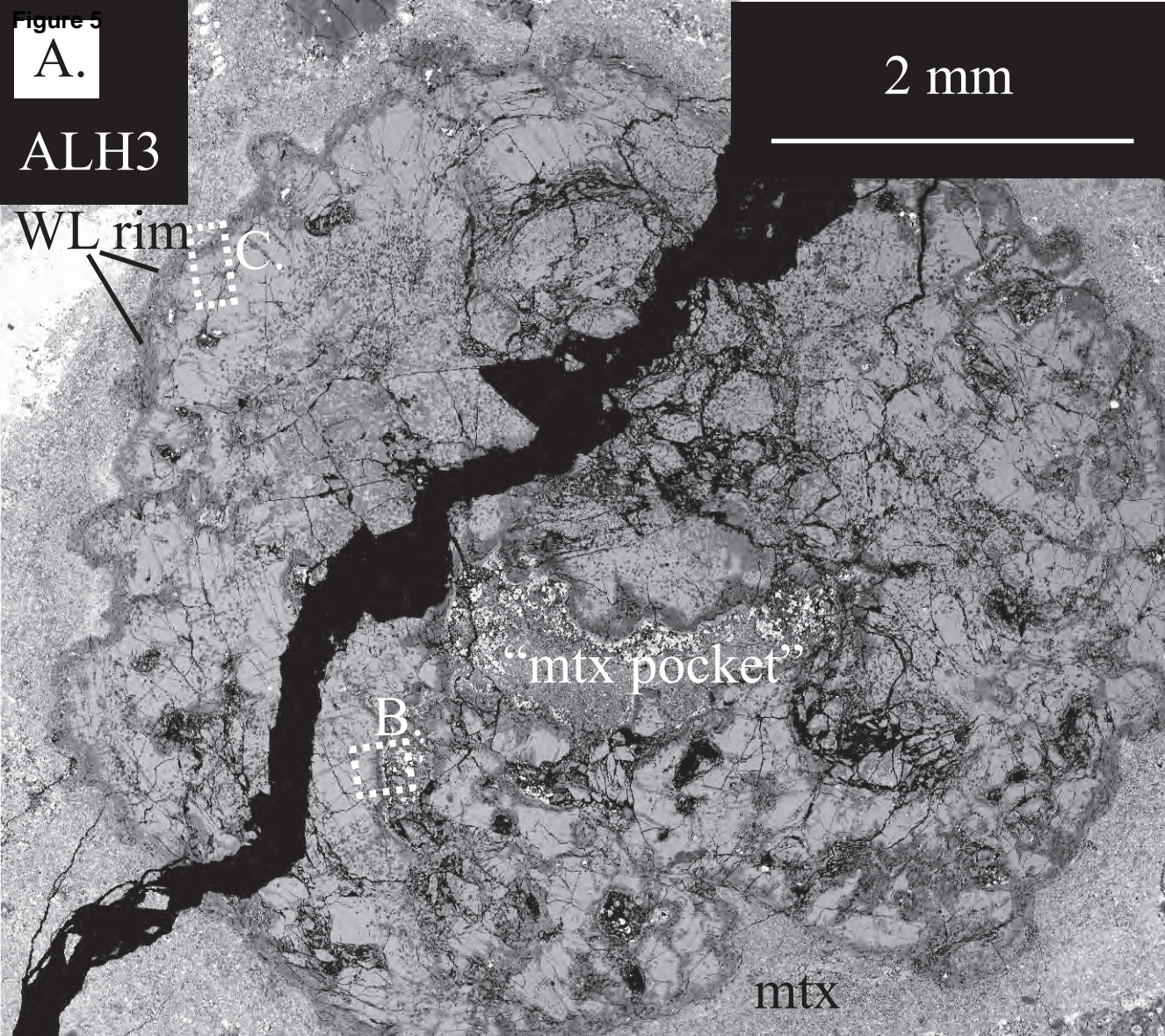


Figure 4





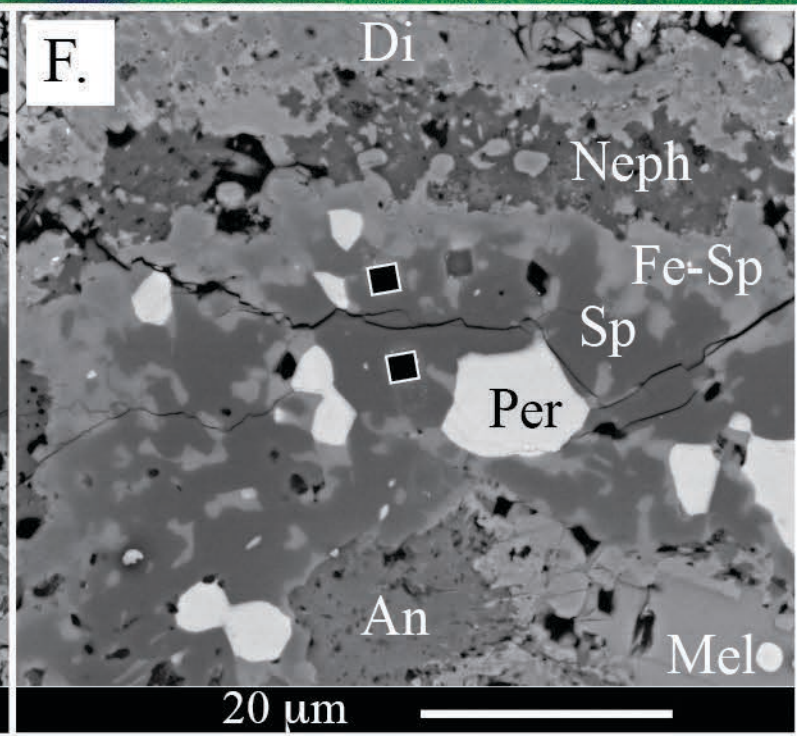
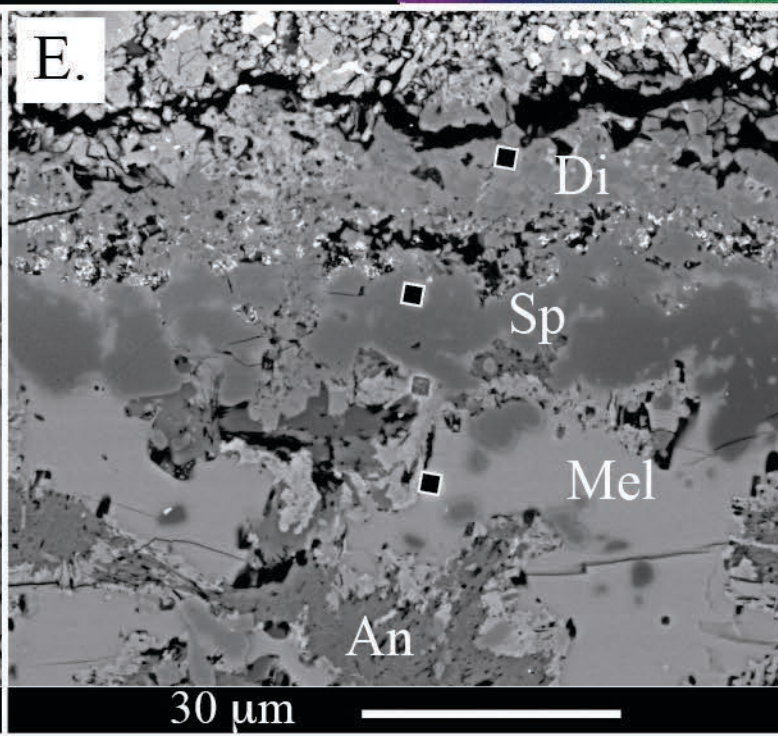
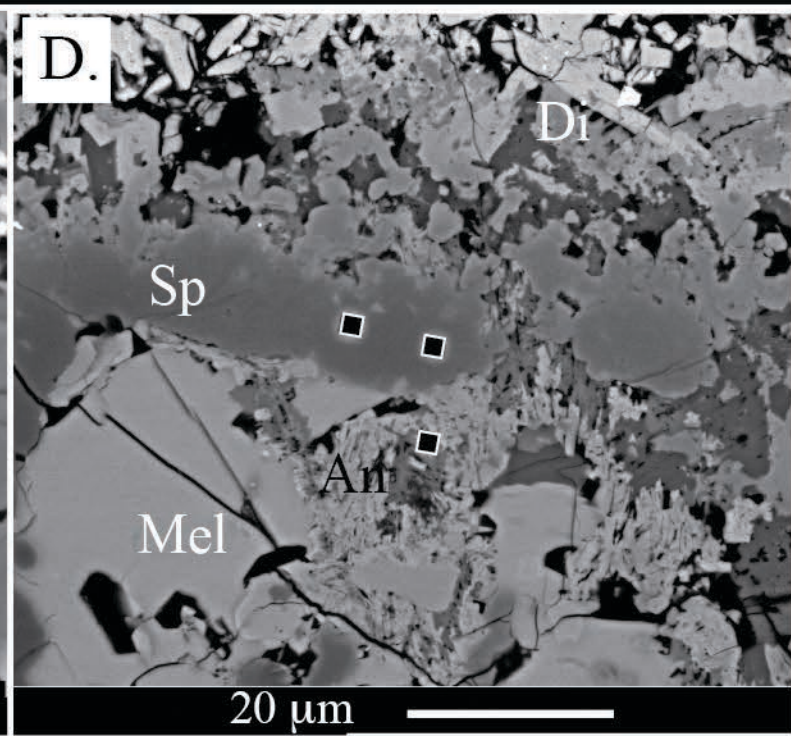
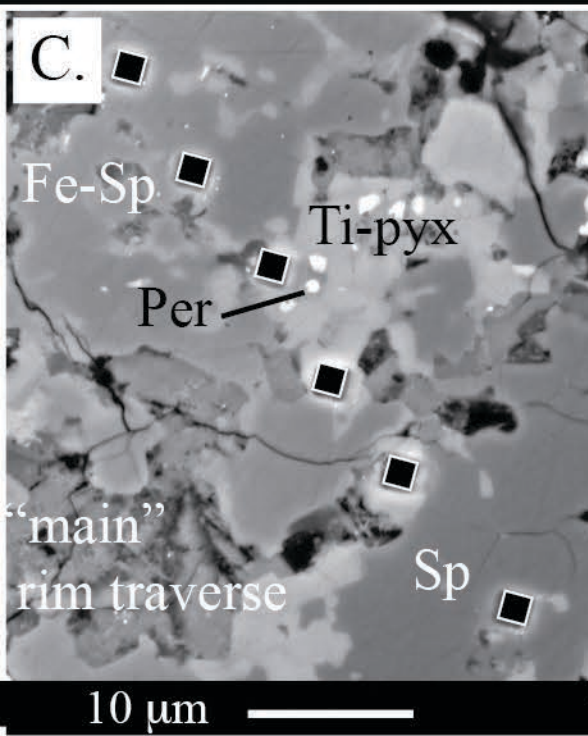
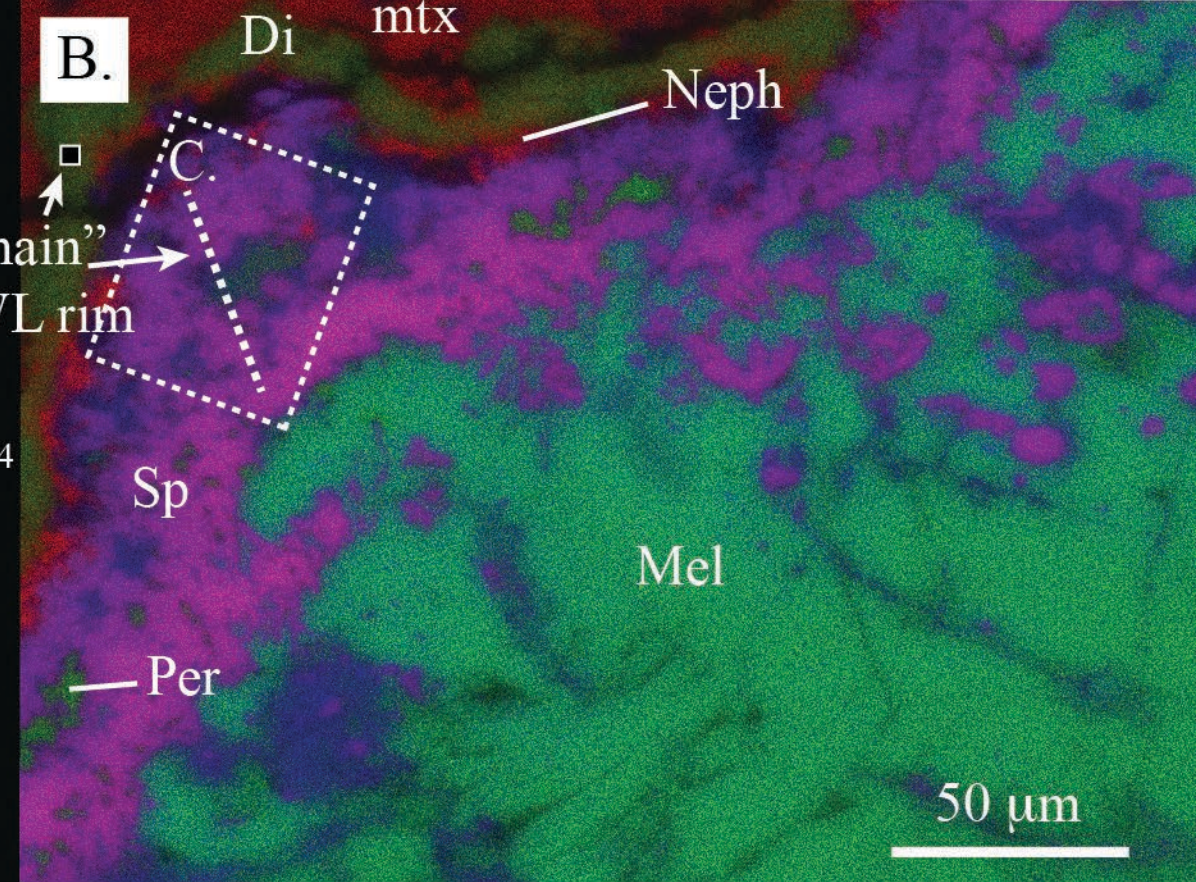
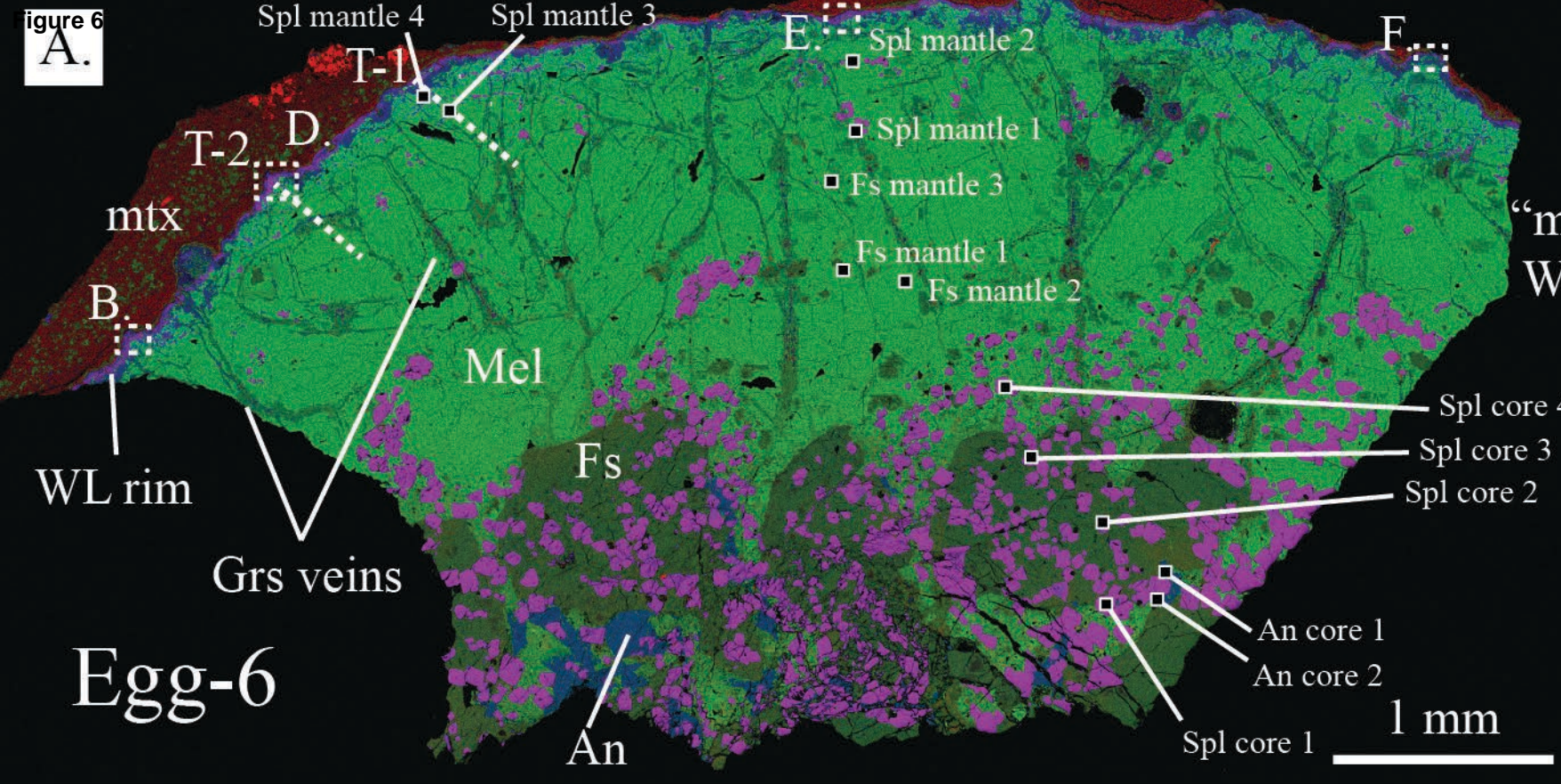


Figure 7

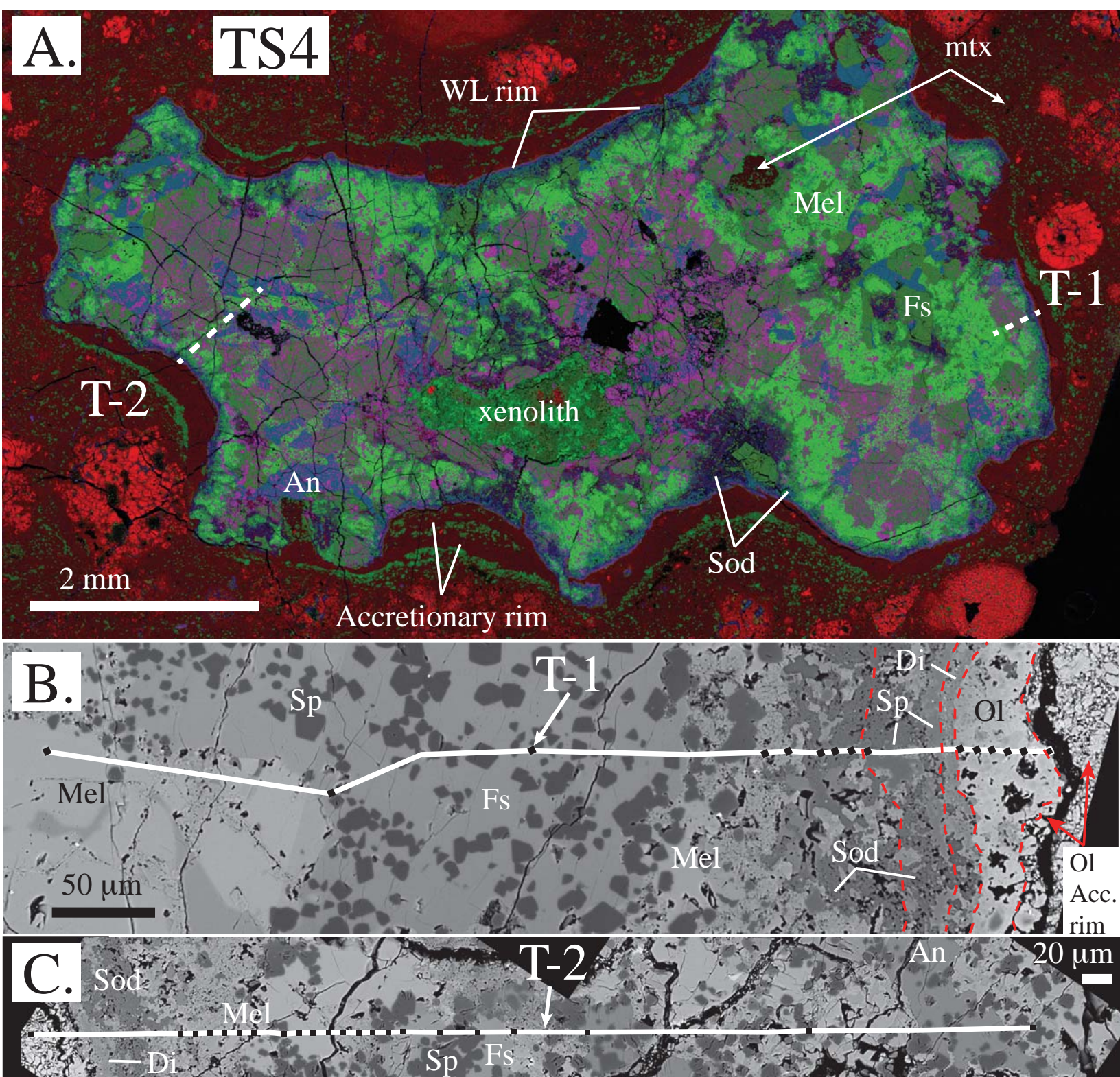


Figure 8

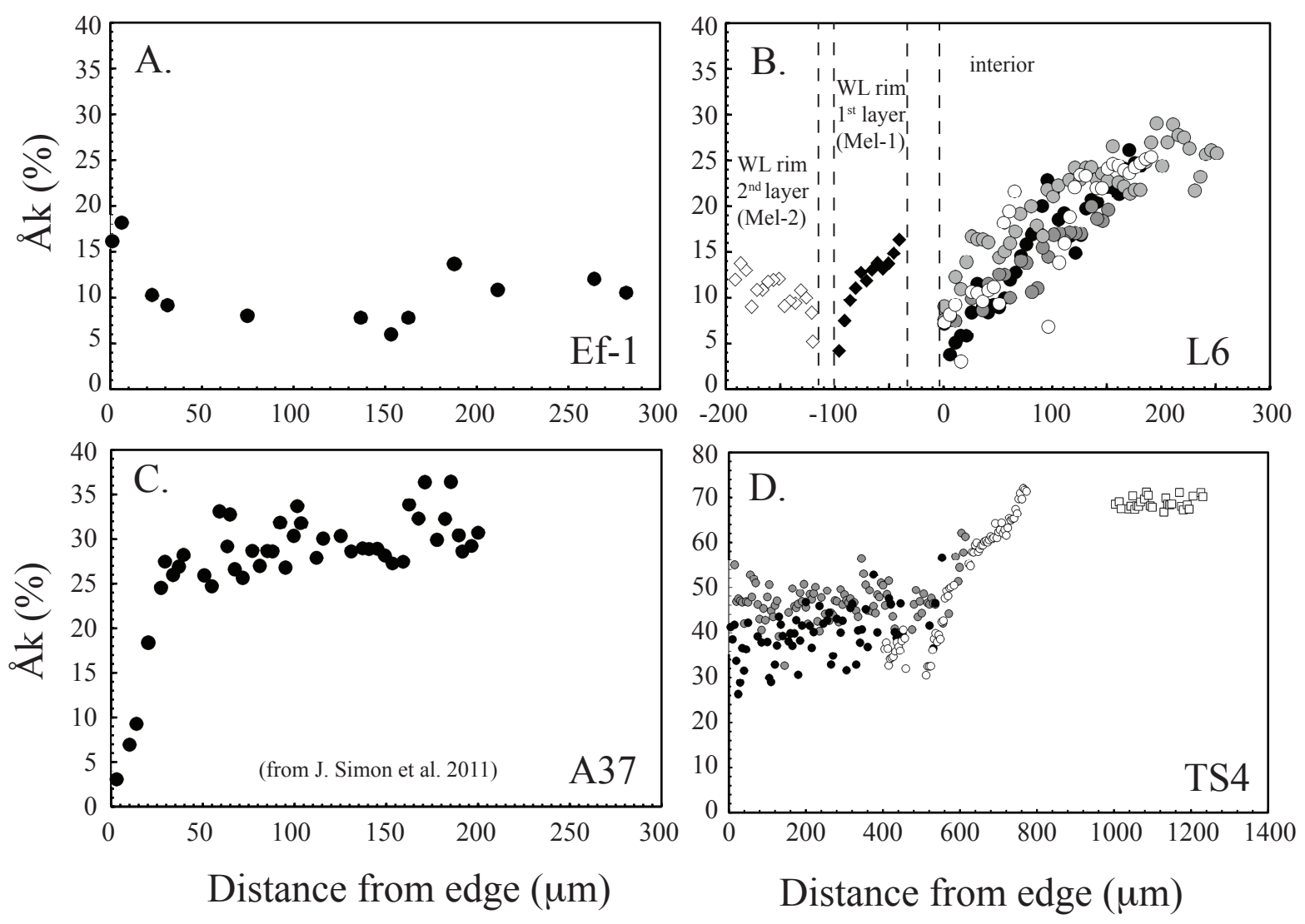


Figure 9 A B5

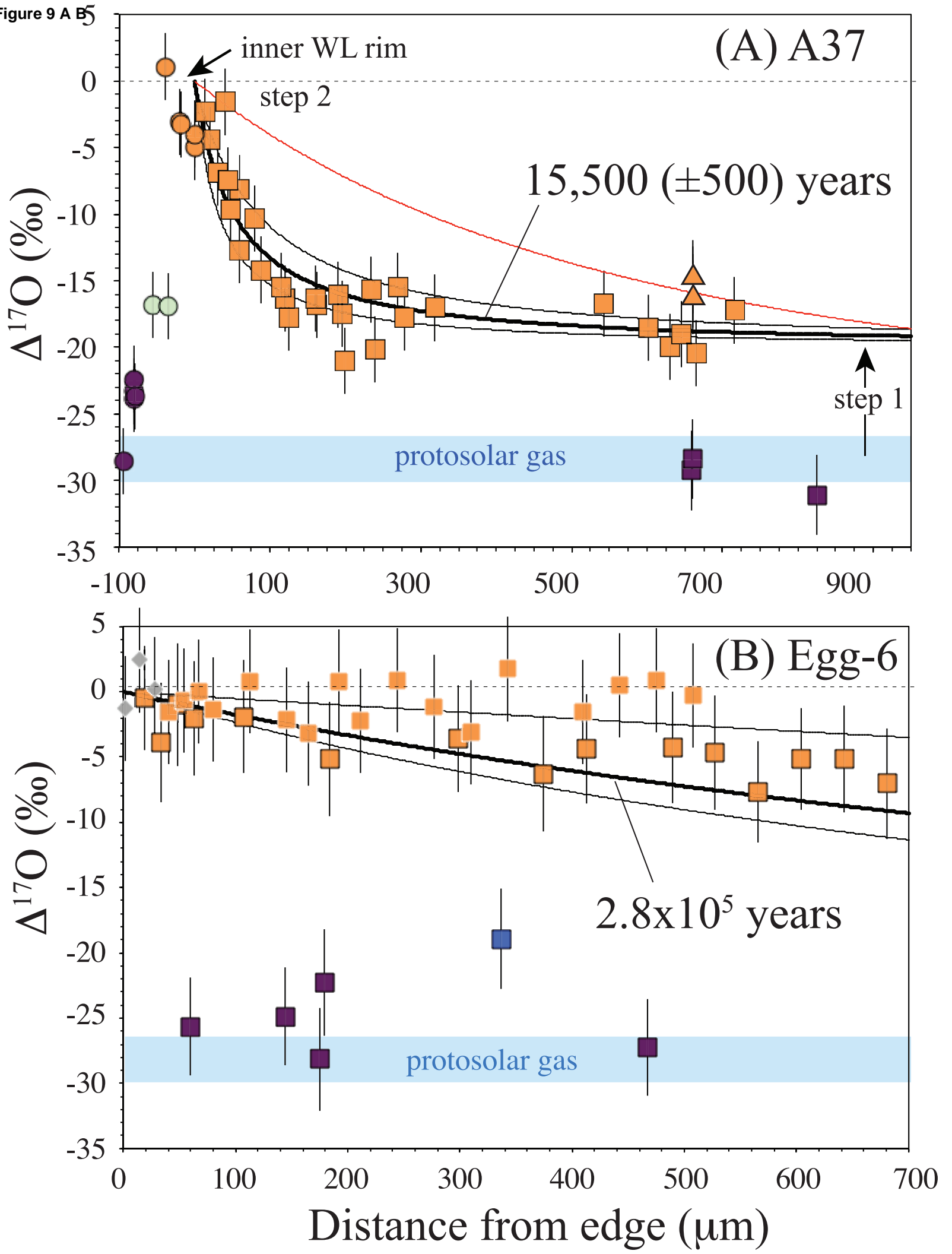


Figure 9 C D

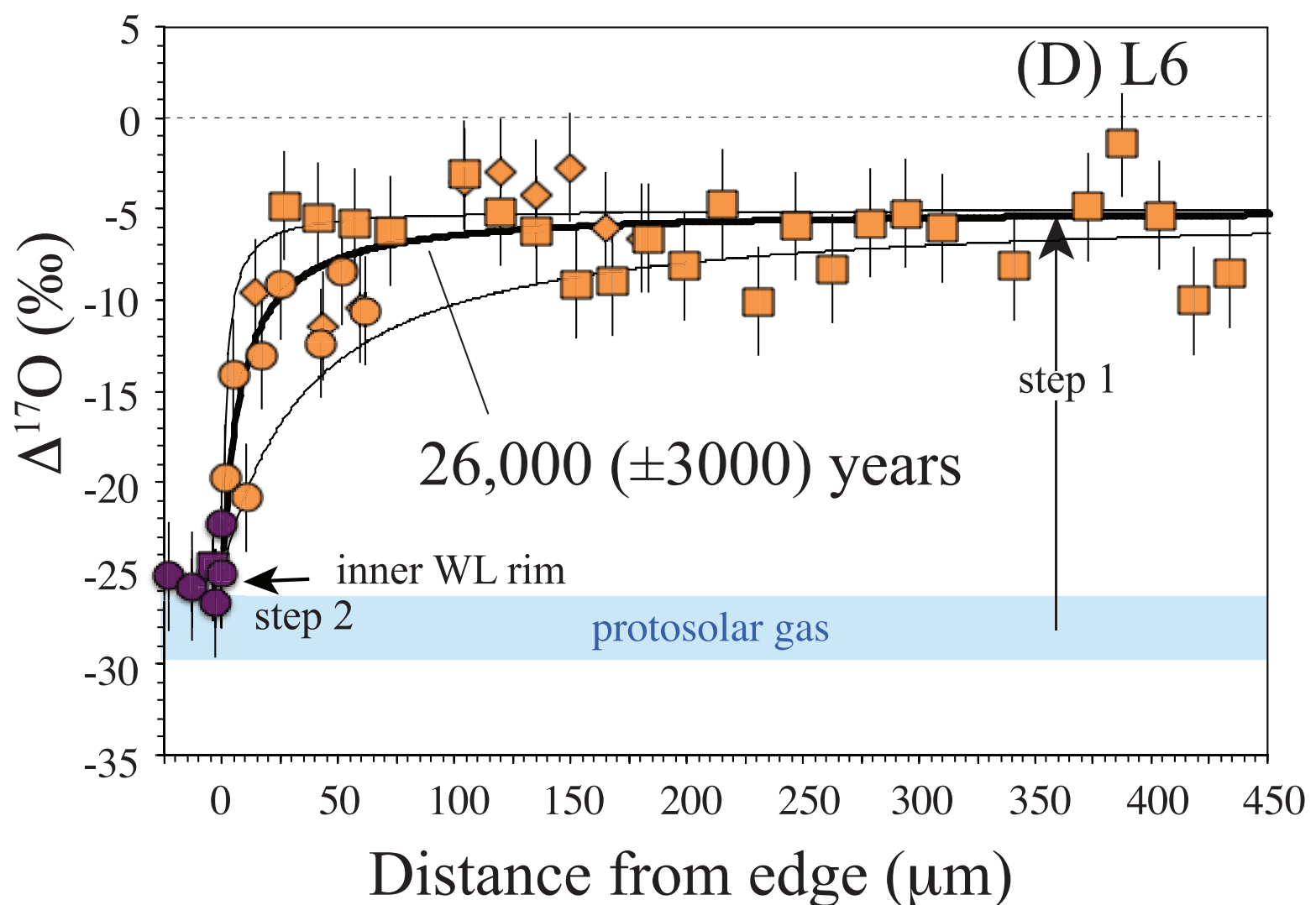
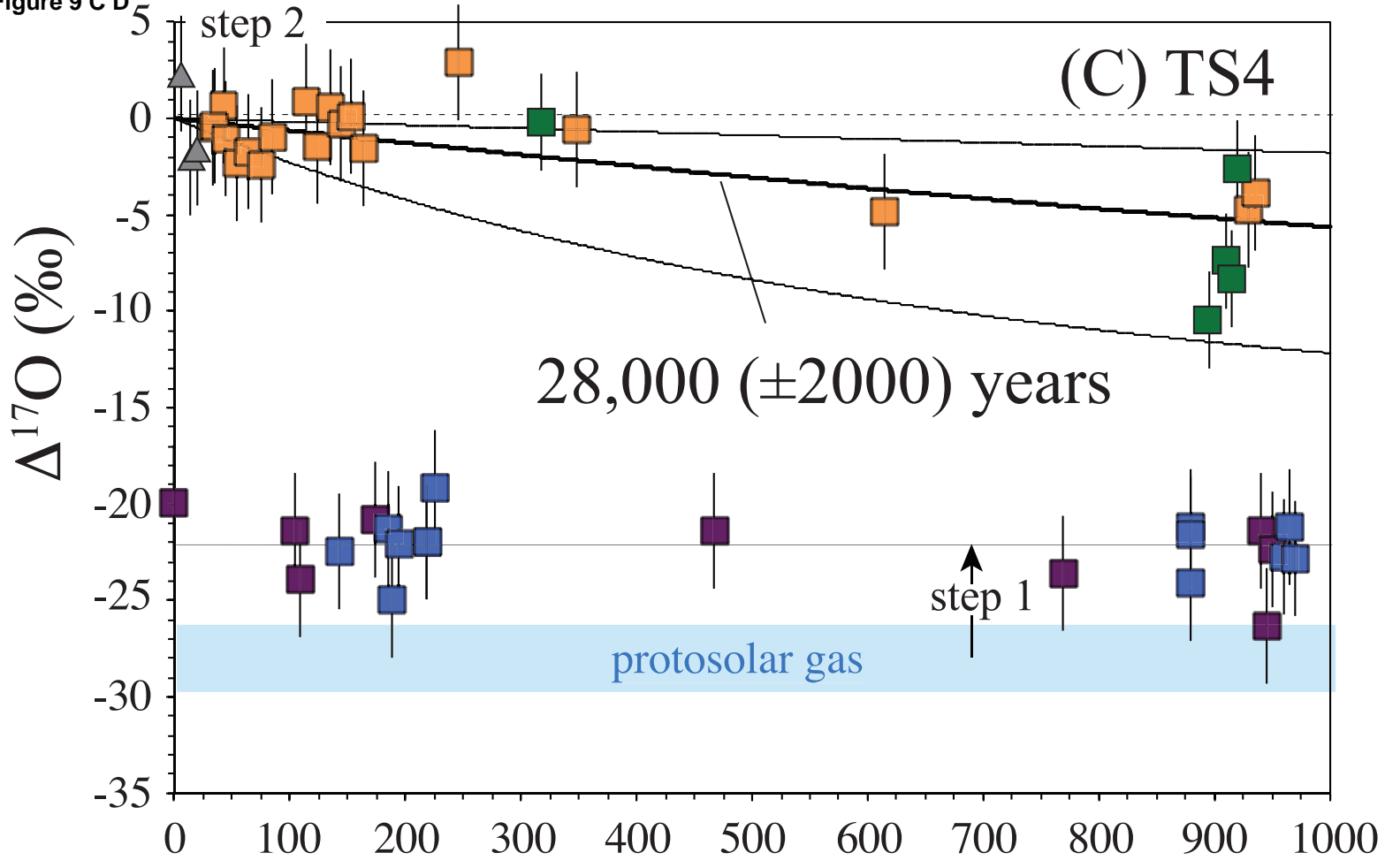
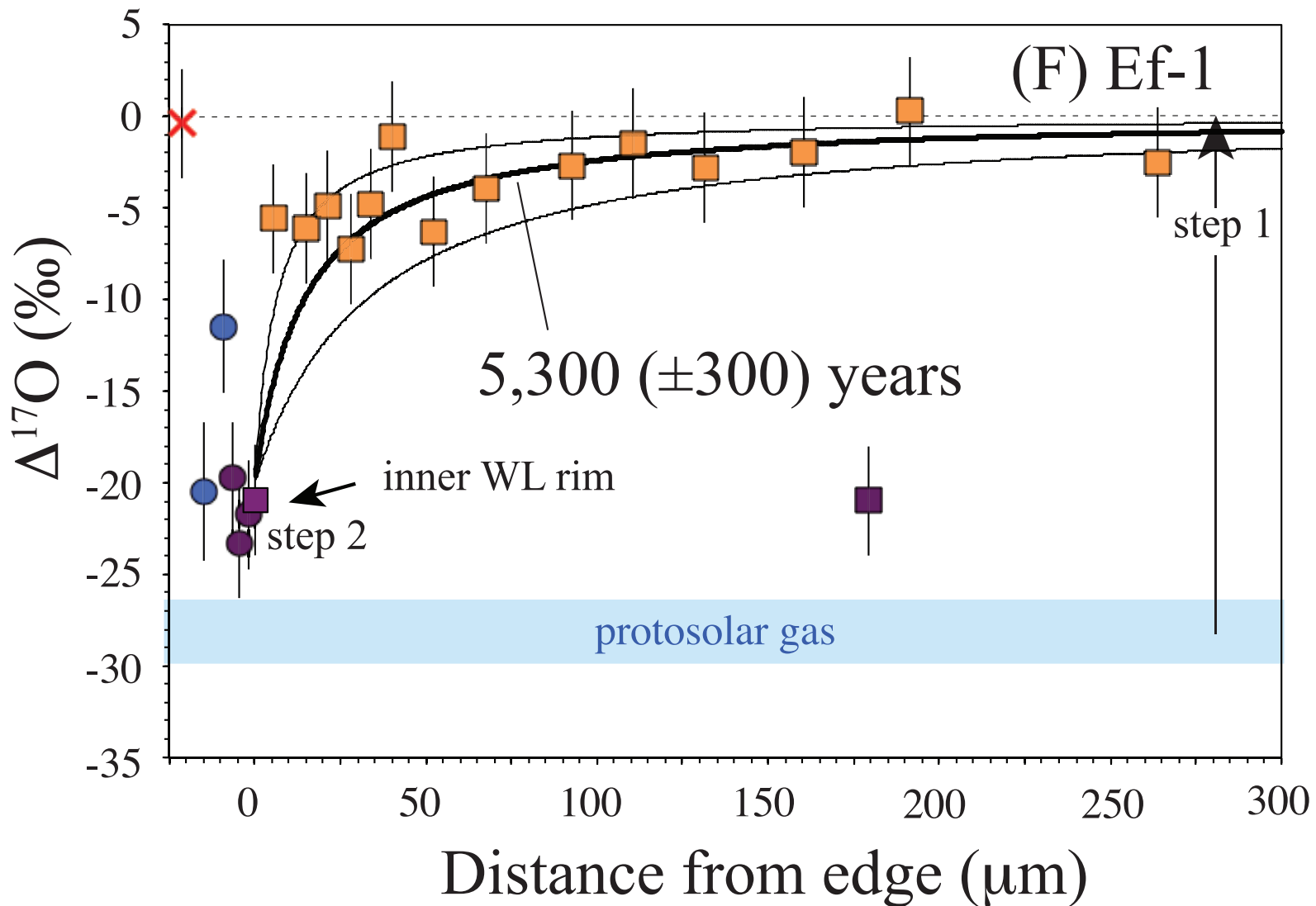
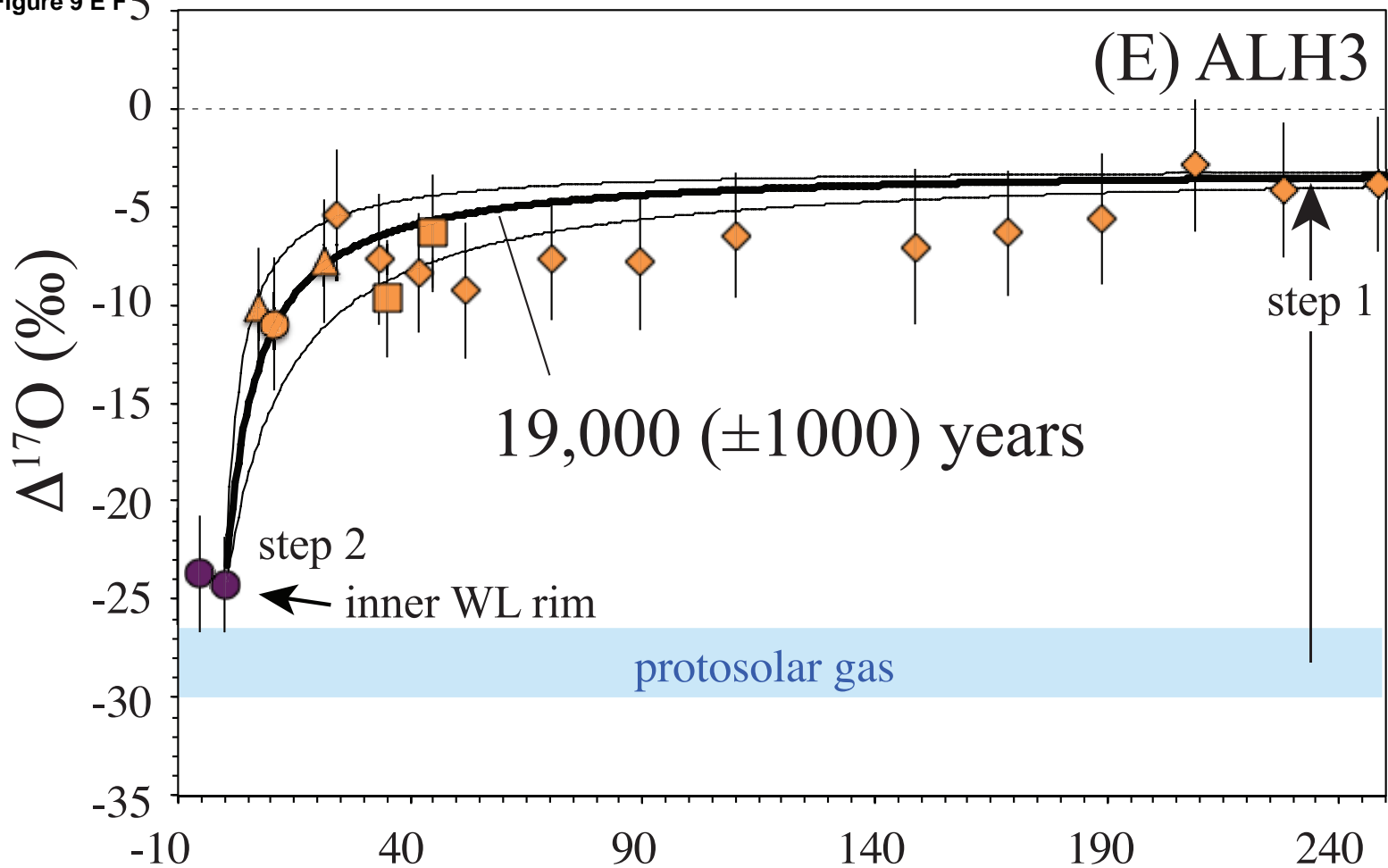
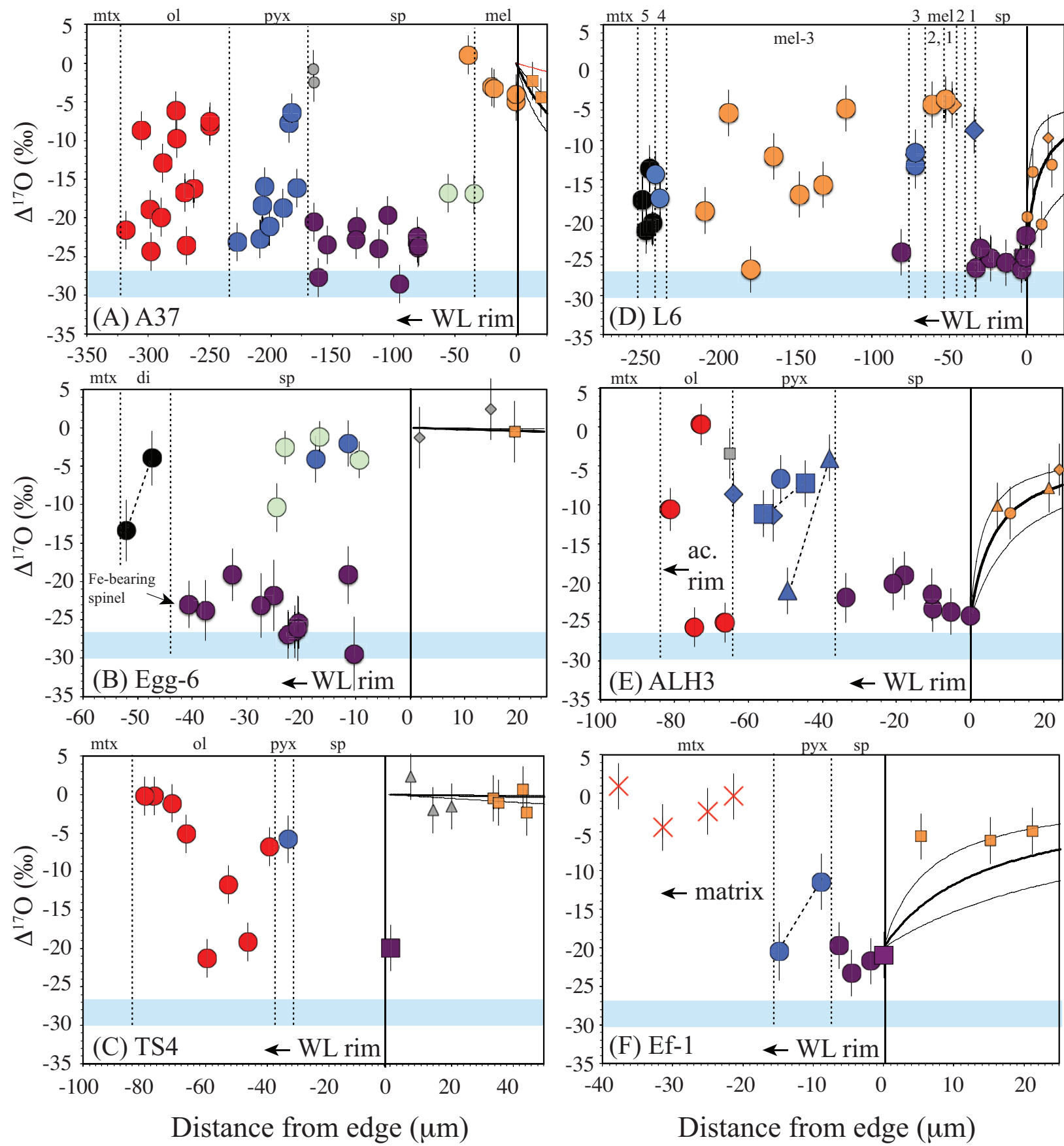


Figure 9 E F 5



**Figure 10**



## Appendix I

[Click here to download Appendix: Appendix I.pdf](#)

## Appendix II

[Click here to download Appendix: Appendix II.pdf](#)